A QUANTITATIVE ANALYSIS OF WING PITCHING IN INSECT FLIGHT

A Dissertation

Presented to the Faculty of the Graduate School

of Cornell University

in Partial Fulfillment of the Requirements for the Degree of

Doctor of Philosophy

by

Attila János Bergou

August 2009

A QUANTITATIVE ANALYSIS OF WING PITCHING IN INSECT FLIGHT

Attila János Bergou, Ph.D.

Cornell University 2009

The flying ability of insects is spellbinding: dragonflies can catch their prey in midair, mosquitoes have an intricate in-flight mating ritual, honey-bees are able to land precisely on a small flower. Even the minute fruit fly can accurately induce sudden flight maneuvers in milliseconds. To gain an understanding of how insects are able to perform these feats, scientists and engineers have, for more than a century and a half, pursued the principles behind how insects fly. This research has lead to many breakthroughs in our understanding of the behavior and force production of flapping wings. Despite such successes, many aspects of how insects are able to maneuver and precisely control their flight with such apparent ease, remain poorly understood.

Insects control their flight by altering the motion of their rapidly beating wings. Therefore, in this thesis, we ask how insects actuate their wings. We focus mainly on a single degree of freedom of the wings: their orientation as they slice through the air, termed the wing pitch. This particular motion is chosen because of the sensitivity of the aerodynamic forces on both fixed wing and flapping flight to changes in wing pitch. The major results of this thesis are contained in §2–§5. In these chapters, we build a quantitative understanding of how insects pitch their wings. This part of the thesis culminates in §5 where we show how insects modulate wing pitching to induce flight maneuvers. We briefly summarize each chapter below.

In §2, we analyze the hovering wing kinematics of insects and find that they

do not do any positive work to pitch their wings. The wing inertia and aerodynamic forces both tend to rotate the wing, suggesting that wing pitching is largely passive.

In §3, we describe the methods we developed to measure and visualize the kinematics of freely-flying fruit flies.

In §4, we analyze the kinematics of freely-flying fruit flies and find that the pitching motion of insect wings can be understood by modeling the viscoelastic properties of the wing joints.

In §5, we analyze the motion of maneuvering fruit flies and find that these insects turn by modulating their wing pitch, in effect rowing through the air. We show that their flight dynamics ultimately derive from fine-tuned biomechanical properties of the wing hinge with only subtle actuation by the musculature.

The second part of the thesis focuses on the numerical methods used throughout this work. In §6, we describe the aerodynamic models used to compute the forces on insect wings. Finally, we end in §7 with a discussion of a topic somewhat separate from the rest of the thesis: we introduce a genetic programming method that determines symbolic relationships between variables from time-series measurements. We apply this method to finding an improved quasi-steady model for the aerodynamic torque that rotates a two-dimensional falling plate.

BIOGRAPHICAL SKETCH

The author of this thesis was born to János and Váléria Bergou on February 13, 1980 in Budapest, Hungary. His family moved several times throughout his childhood and so he grew up in many cities at once. He, however, always called Budapest home. In 1990, his family moved to the New York area, where his father became a physics professor. He thus spent the rest of his childhood in East Brunswick, NJ. While in high school Attila was a swimmer and occasionally ran track. Being the son of a biologist and a physicist, through the encouragement of his parents, he developed an early interest in science and took part in the math team and various other academic endeavours.

Attila attended Carnegie Mellon University to pursue his undergraduate degree. This was the first time he realized quite how broad his interests where: while he was definitely drawn to the quantitative sciences, he found that he had interests that spanned several fields. Carnegie Mellon was very accommodating and thus he pursued a dual degree in physics and computer science. On the computer science end Attila became keenly interested in systems programming and, with the many entrepreneurial opportunities at CMU, culminated in him working for a small startup named Vivisimo (makers of the search engine Clusty) and eventually for the Linux platform team at IBM. He, however, came to realize that, as satisfying computer science was, he missed fundamental research at both these jobs. In the meantime he very much enjoyed the undergraduate research he was performing on the physics end of his interests. When he graduated CMU, Attila knew that he wanted to go to graduate school. To help him decide between pursuing a computer science or a physics PhD, he took a year to work at Jet Propulsion Laboratory before applying to graduate school.

At JPL, Attila joined the Exploration Systems Autonomy section as a graduate co-op student. He found the experience of working at JPL remarkable. While there, he had the opportunity to work for two different groups. He started out working on relativistic quantum information theory for the Quantum Computer Technologist group. After working there for about six months, he spent his remaining months working for Parallel Application Technologies group. There, he worked for the national virtual observatory project. He found both of these incredible opportunities and these pushed him to enter graduate school in physics at Cornell University.

After arriving at Cornell University in the fall of 2003 Attila spent some time exploring the different areas of physics. After his experience with relativistic quantum mechanics at JPL, initially Attila thought that he would study theoretical physics. He, however, came to realize in doing so he missed computation. That was when, through his friend Gordon Berman, he came upon the research of Prof. Jane Wang. He found Jane's research to be fascinating and the perfect combination of computation and physics. He joined her group in the summer of 2005 and worked in closely with, graduate students and friends, Gordon Berman and Leif Ristroph to study how insects control their flight.

After completing his PhD, Attila will join the engineering department at Brown University as a postdoctoral researcher.

Dedicated to my family,

Valéria, János, Miklós, and Katalin Bergou.

ACKNOWLEDGEMENTS

Throughout my PhD numerous people helped me with their expertise, advice and support. I would like to thank them all very much.

I would like to begin by especially thanking my advisor, Jane Wang, from whom I absorbed an immense amount of knowledge, enthusiasm, and guidance throughout my PhD. Of course, I must also thank Gordon Berman, my fellow insectophile who sat just a few feet away me for the better part of my PhD. The constant discussions we had about research and his insightful comments and criticisms helped me throughout my graduate school career. I must also thank my initial mentors when I was first introduced to the Wang Lab: Sheng Xu, Anders Andersen, and Umberto Pesavento, from who I absorbed much knowledge about both fluid dynamics and insect flight.

I would like to thank our collaborators Itai Cohen and Leif Ristroph have both helped me grow as a scientist and greatly improved the material in this thesis. In addition, I would like to also thank John Guckenheimer and Andy Ruina who have also provided invaluable advice and criticisms that have also improved this work considerably.

I would also like to thank my special committee for providing me with advice and guidance throughout the years.

My friends and confidants who have helped me keep my sanity throughout the years: Brooke, Umberto, James, Leif, Gordon, Arend, Ben, Mark, Sophie, Johannes, Brian, Simon, Jörn, Vlad, and so many others. . . Thank you!

Finally, I would like to thank my parents, János and Valéria, brother and sister, Miklós and Katalin, for unending support.

TABLE OF CONTENTS

LIST OF TABLES

LIST OF FIGURES

CHAPTER 1

OVERVIEW

The apparent ease with which insects can perform complex flight maneuvers has long fascinated scientists. The speed insects move with, however, has been an obstacle to understanding their motion: many insects beat their wings dozens, even hundreds of times a second and perform rapid maneuvers in only milliseconds. These short timescales are far too fast for human vision to capture the intricacies of their motion. Thus, the study of insect flight truly began in the mid-nineteenth century, when the advent of the stroboscope and photography allowed scientists to appreciate the elegant motion of insects for the first time [1, 2]. Over a century and a half much progress has been made in this rich field of research. For example, scientists have learned many of the aerodynamic mechanisms insects use to produce the forces on their wings [3–15]. At the same time, biologists have cataloged and explored the muscles that drive the insect wings [16–23]. There remain, however, innumerable open questions yet to be answered.

In this body of work, we quantitatively analyze how insects actuate their wings. At a basic level, these actuations are caused by a cascade of neural and muscle firings. Neurons fire to send a signal to flight muscles whose actions, in turn, combine with mechanical properties of joints to actuate the motion of insect wings. The wings then move in response to both the torques exerted by the insect and the aerodynamic and inertial forces acting on them. Finally, the flight path of the insect is altered by the aerodynamic forces caused by its coupled wing and body motions. Because of the complex physiology and dynamics of insect wings, how wing motions are actuated and how they induce an insect

to maneuver remain poorly understood. In this thesis, we specifically focus on understanding how insects actuate the orientation of their wings as they slice through the air. Aerodynamic forces on wings are particularly sensitive to this motion, called the wing pitch [15]. In fact, fixed winged aircraft are primarily controlled by varying the orientation of their flight surfaces and research shows that wing pitch plays a similarly import role in insect flight [24,25].

We determine how insects actuate their wing pitch directly from measurements of their wing and body motion. From these measurements, we infer the forces and torques acting on the insects and in conjunction with computer simulations and mathematical models show how they are actuated. There are, however, millions of different species of insects [21]. Therefore, examining the flight mechanics of each species individually is impossible and we must choose a representative species to study. With a few exceptions, notably §2, we focus our analysis on the flight mechanics of *Drosophila melanogaster*. These tiny insects are ideally suited for flight research because they are easily reared in a laboratory environment. As a result, the physiology and genetics of this insect is thoroughly researched allowing for the eventual connection of flight research with the biology of the organism.

This thesis is roughly divided into into two parts. The first part, §2–5, contains the major results of the thesis. In these chapters, we quantitatively analyze the pitching motion of insect wings and build a model to show how this motion arises. This research direction culminates in §5, where we show how insects modulate the pitch of their wings to steer their flight through the air. The second part of the thesis, §6 and §7, is focused on the numerical methods that we use throughout this work to study the aerodynamic forces on insect wings. We

briefly summarize each chapter below.

We begin in §2 by analyzing published wing kinematics of hovering fruit flies, dragonflies, and hawkmoths to determine whether insects need to expend energy to pitch their wings. We determine this energy by inferring the forces and torques driving the wings, and computing the mechanical energy involved in wing rotation. These methods allow us to infer whether direct muscular actuation is necessary to pitch the wings. We find that the wing inertia and aerodynamic forces both tend to naturally rock the wing back and forth suggesting that this motion may be largely passive.

In §3, we describe the Hull Reconstruction Motion Tracking (HRMT) technique developed by Leif Ristroph, Gordon Berman and the author of this thesis. This method allows us to accurately recover the kinematics of freely flying fruit flies at a level of detail that has previously been impossible. Aside from a description of the method the accuracy is rigorously assessed. Furthermore techniques are introduced to accurately differentiate the kinematic data as reduce the data.

In §4 we apply HRMT to several hundred measured strokes of freely flying *D. melanogaster* to determine the torques that an insect exerted by the insect to drive its wings. We confirm the results of §2 that the torque are passive. Furthermore, we show that they may can be accurately modeled by a damped torsional spring. Finally, we discuss the properties of the wing hinge that can give rise to such behavior.

In §5, we analyze fruit flies performing sharp turns to determine how they induce these maneuvers. We find that, to turn, *Drosophila* modulate their wing

pitch and in effect row through the air. We also show that despite this modulation the pitching of the insect wings is still primarily passive. In fact, insects use the passive pitching behavior of their wings and effectively bias the rest angle of the torsional spring that induces wings to pitch achieve the rowing motions of the wings. Finally, we discuss the biomechanical implications of this result.

In §6 we describe the numerical methods which are used to throughout the thesis. Specifically, we detail the models we use to determine the aerodynamic forces on a flying insect from its wing and body kinematics. We also describe how these force models are extended to model the passive fluid dynamic interactions that a wing undergoes.

The final chapter, §7, is a separate project that is related to the numerical methods of §6. In this chapter, we introduce a genetic programming method that determines symbolic relationships between variables from time-series measurements. We apply this method to finding an improved quasi-steady model for the aerodynamic torque that rotates a two-dimensional falling plate.

CHAPTER 2

PASSIVE WING PITCH REVERSAL IN INSECT FLIGHT

2.1 Introduction [1]

Due to morphological constraints, insects must reverse the direction of their wing motion periodically. Correspondingly, the wing pitch is also reversed in order to maintain a positive angle of attack during the entire period. At the transition from an up-stroke to a down-stroke, the wing pitch reversal is called pronation, and at the transition from a down-stroke to an up-stroke, it is called supination. For dragonflies, the reversal of their wing's pitch is primarily responsible for orienting the wing so that it plunges down at a large angle of attack and then returns at a smaller one. We show snapshots of the wing motion of a tethered dragonfly in Fig. 2.1. Pronation occurs in frames 1–2 and supination can be observed in frames 5–7. In other insects (e.g., fruit flies), the pitch reverses such that the mid-stroke angle of attack is about the same in the back and forth strokes. This sudden wing pitch reversal marks the main difference between hovering using flapping motion and using a continuously rotating wing. It is therefore of interest to understand whether the pitch reversal necessarily requires active muscle control from the insect or if it can result from a passive mechanism.

Insects are able to independently modulate the timing of the pitch reversal of their left and right wings [14, 27], suggesting that flight muscles may be involved in driving its motion. The manner in which insect wings are driven by

[1] The work presented in this chapter originally appeared in Bergou, Xu & Wang, *J. Fluid. Mech.*, **591**, 321–337 (2007).

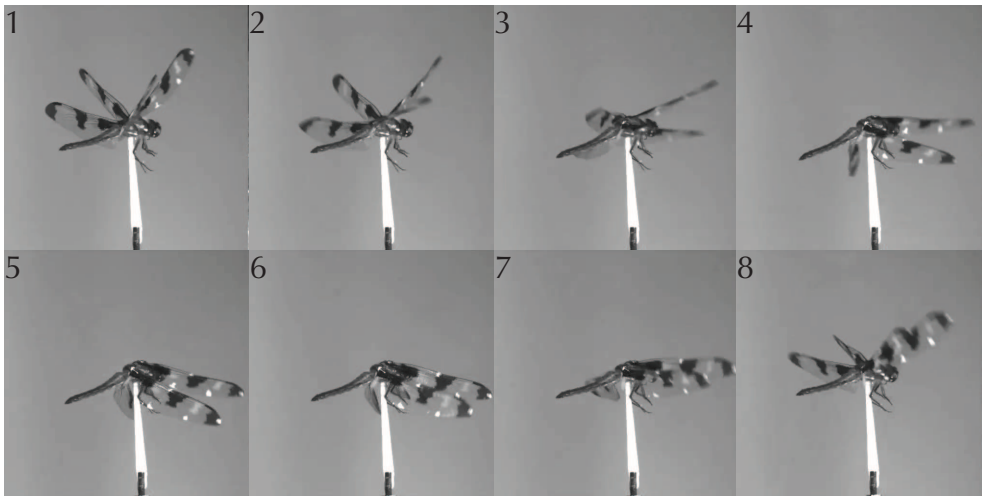

Figure 2.1: Snapshots from the video of tethered dragonfly motion during one period [26].

flight muscles, however, tend to naturally pitch the insect wing. Specifically, the wing driving forces act through an axis near the leading edge of the wing [28]. Because the wing's center of mass is behind the leading edge of the wing, muscle forces will cause a moment about the center of mass that will cause it to pitch. In fact, the inertial forces on the wings of a housefly, indicate that wing inertia alone may be sufficient to cause wing pitch reversal [29].

In this paper, we compute the power required by the insect to pitch its wings. We take into account aerodynamic forces on the wing as well as the wing inertia, i.e. the position of the center of mass with respect to the torsion axis. To compute the aerodynamic power, we solve the 2D Navier-Stokes equations as well as using a simplified quasi-steady force model for observed wing kinematics. We analyze several wing kinematics, including those measured from a tethered dragonfly [26], as well as published kinematics of a hovering fruit fly [30], hovering hawkmoth [31], and simplified dragonfly hovering kinematics [32]. We find that for all the kinematics, no power is required from the insect for wing pitch reversal, thus the wing pitch is passive. We further observe that the ro-

tational power due to aerodynamic forces is greater than inertial effects in fruit flies and dragonflies. In hawkmoths, the inertial effects become more important. Employing a quasi-steady model, we show that for any kinematics where pitch reversal occurs near stroke reversal, where forces due to wing acceleration and wing rotation dominate those due to velocity, both the aerodynamic and the inertial forces aid the wing pitching. A signature of passive wing pitch reversal is the direction of the torsional wave traveling along the back of the wing during reversal. If it propagates from near the tip to the root, then this suggests that the aerodynamic force, which is maximal near the tip, is responsible for the turning motion. If the wave propagates from the root to tip, then it suggests that the muscle force applied near the root, is turning the wing. We observe a torsional wave traveling from tip to root for the dragonfly wing kinematics, thus providing experimental evidence for our results.

2.2 Energetics of Wing Rotation

In order to determine whether the wing pitch reversal is active or passive, we calculate the power required by the insect to produce the observed pitching motion. The pitch is the rotational motion of the wing about the torsion axis, the axis through which the forces produced by the muscles of the insect wing act, and about which forces applied to the wing will generate no moment on the wing [28]. Accordingly, in order to determine the power requirements, we calculate the rotational power about this line.

Although the immersed interface method we use for direct numerical simulation is naturally suited for modeling a flexible wing structure, in this paper,

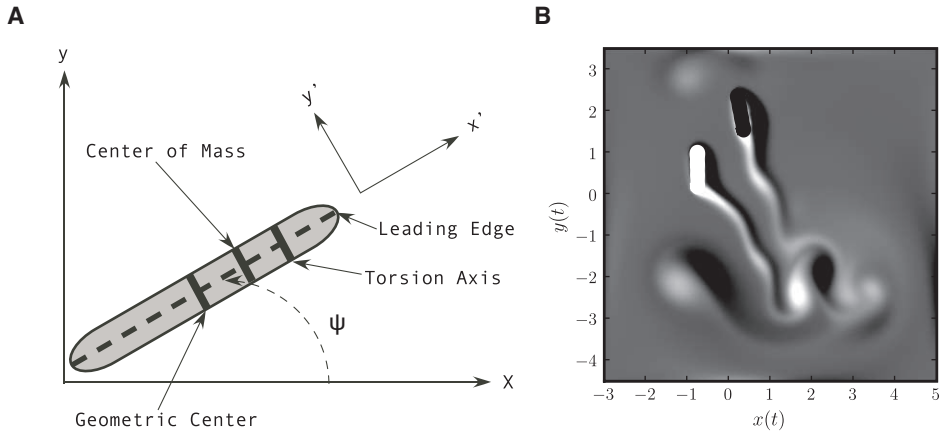

Figure 2.2: (**A**) 2D coordinate system. The wing chord is shaded in gray. For a dragonfly the torsion axis and the center of mass are located at approximately 15% and 30% of a chord length behind the leading edge of the wing. (**B**) A snapshot of vorticity field during flapping period just prior to pronation.

we approximate the wing as a rigid plate to calculate 2D forces and power. This is motivated by the observation that the most visible deformation during wing pitch reversal is the twisting along the torsional axis [33]. The twisting is mainly caused by the different amounts of wing rotation along the wingspan. This deformation is different from the camber of a clamped plate due to the forces applied at the two ends. The rigid plate approximation simplifies analysis and also helps us decouple the effect of the wing camber, which is interesting in its own right [34], from the effect of twisting due to pitching which is our current focus. We will first calculate the rotational power on a 2D rigid wing. By applying blade-element theory to the 2D result, we can qualitatively explain the twisting along the span of the wing. The 2D cross-section of the insect wing is shown in Fig. 2.2A. In this model, the angular motion of the 3D wing is described by translation in the $\hat{x}$ and $\hat{y}$ direction, while pitching corresponds to the angle ψ. The locations of the torsion axis and center of mass of a dragonfly wing are taken from measurements in [28].

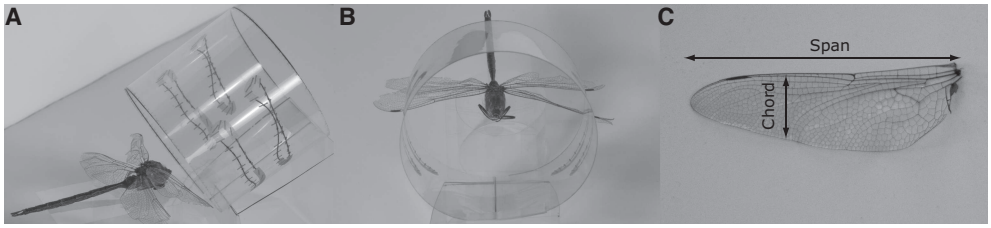

Figure 2.3: Illustration of the 3D to 2D conversion of the dragonfly wing kinematics. In (**A**) and (**B**) we show a 3D image of the dragonfly with the 2D projection cylinder. In (**C**) we see the 2D wing with the slices superimposed on them.

Given a set of kinematics, the total power that is exerted by the insect, P_{insect}, can then be calculated from,

$$P_{\text{inertial}} = m\vec{a}_{\text{cm}} \cdot \vec{v}_{\text{cm}} + I_{\text{cm}}\ddot{\psi}\dot{\psi} = P_{\text{aerodynamic}} + P_{\text{insect}}, \tag{2.1}$$

where $\vec{a}_{\text{cm}}$ and $\vec{v}_{\text{cm}}$ are the velocity and acceleration of the center of mass of the wing, m and I_{cm} are mass and moment of inertia of the wing. The power can be decomposed into rotational and translational components about the torsion axis. The power required by the insect to pitch the wing, P_{rot}, is then

$$P_{\text{rot}} = \underbrace{\dot{\psi}d_{\text{cm}}(ma_x \sin\psi - ma_y \cos\psi) + I_{\text{cm}}\ddot{\psi}\dot{\psi}}_{P^{\text{rot}}_{\text{inertial}}} \underbrace{-\dot{\psi}d_{\text{gc}}(F_x \sin\psi - F_y \cos\psi) - \dot{\psi}\tau}_{-P^{\text{rot}}_{\text{aerodynamic}}}, \tag{2.2}$$

where d_{cm} is the distance from the center of mass to the torsion axis, d_{gc} is the distance from the geometric center of the wing to the torsion axis and F_x, F_y and τ are the aerodynamic forces and torque about the geometric center of the wing, and the accelerations, a_x and a_y, are at the center of mass.

2.3 Measurement of Wing Kinematics

We use the tethered dragonfly wing kinematics measured in [26]. In order to obtain the motion in 3D using a single camera, a mirror was placed near the

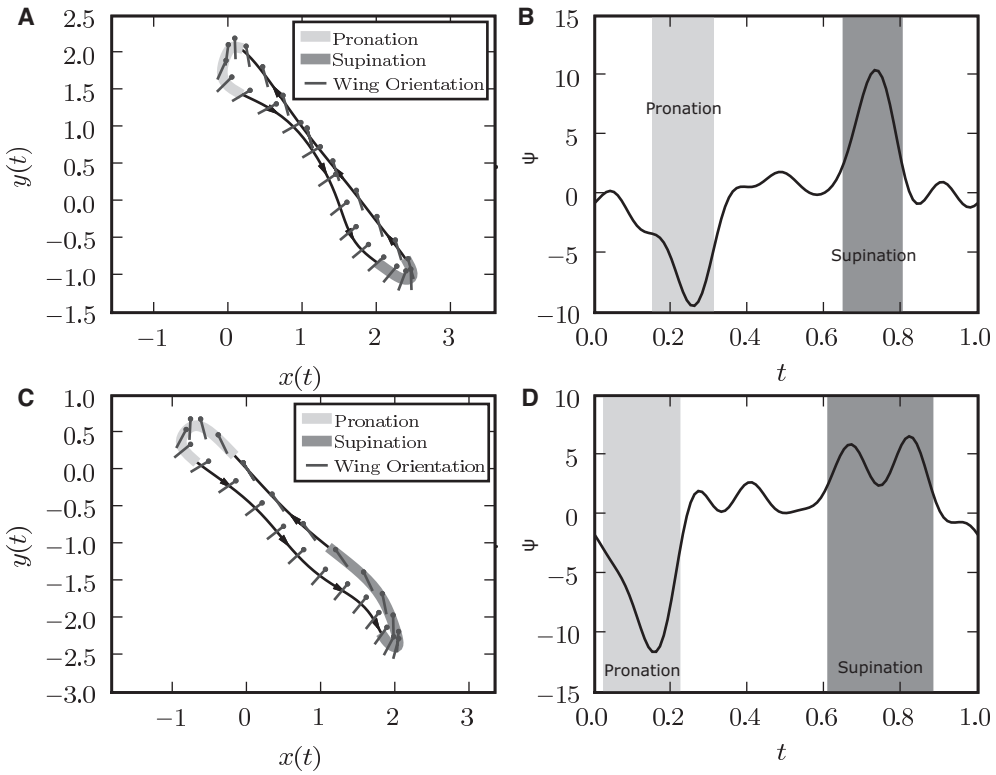

Figure 2.4: Projected motion and angular velocity of a fore- ((**A**) and (**B**) respectively) and a hindwing ((**C**) and (**D**) respectively). In (A) and (C), the lines indicate snapshots of the angular orientation of the wing (for clarity line lengths are scaled to 40% of the actual chord-length of the wing). The leading edge of the wing is denoted by the dot. Lengths are in units of chord length, and time in units of flapping period.

dragonfly. Both the insect and the reflection were recorded using a high speed camera at 1500 frames per second. In Fig. 2.1, we can see snapshots of the captured wing motion reproduced from [26]. From the video, 3D kinematics were reconstructed using three marked points on the wings for 5 beats of the insects wing. This was done by treating the wings as rigid bodies, ignoring any deformation.

The two pairs of wings move symmetrically and the wing interaction between the two sides is negligible due to the small stroke angle, we therefore simulate a pair of wings on one side. As mentioned above we simulate a 2D

cross-section. As shown in Fig. 2.3 the stroke-planes of the fore- and hind-wings are nearly parallel, oriented at 37° from the vertical. As a result of this, a single cylinder can be aligned such that the axis is perpendicular to both stroke planes. To make use of this fact for the 2D projection, we take such a cylinder with a radius 2/3's the wingspan of the forewing, and use its intersection with the leading edge of each wing to determine the trace of each wing on the cylinder. Conversion to Cartesian coordinates is done by unwrapping the cylinder about the mid-stroke and defining the 2D coordinate system so that the $\hat{y}$ corresponds to the vertical direction. Making use of a second intersection point of the wing with the cylinder, we additionally calculate the pitching angle in the 2D coordinate system. To avoid varying the chord length throughout the motion, a constant chord length is maintained and wing position and orientation are determined by the leading edge intersection of the wing and the pitching angle determined from the second intersection point respectively. This corresponds, approximately, to taking the 2D cross-section of the wing shown in Fig. 2.3C.

The resulting motion is parametrized by the position of the center of the wing, $x(t)$ and $y(t)$, and the angular orientation of the wing chord, $\psi(t)$, as defined Fig. 2.2A. The average 2D stroke is given by fitting the resulting wing kinematics with an 8 parameter Fourier series to each of $x(t)$, $y(t)$ and $\psi(t)$. The resulting 2D kinematics, the unwrapped motion of the wings, are shown in Figs. 2.4A and 2.4B. On these figures, we also see the regions of pronation and supination, which are found by analyzing the pitching velocity of the wing, $\dot{\psi}$, shown in Figs. 2.4B and 2.4D.

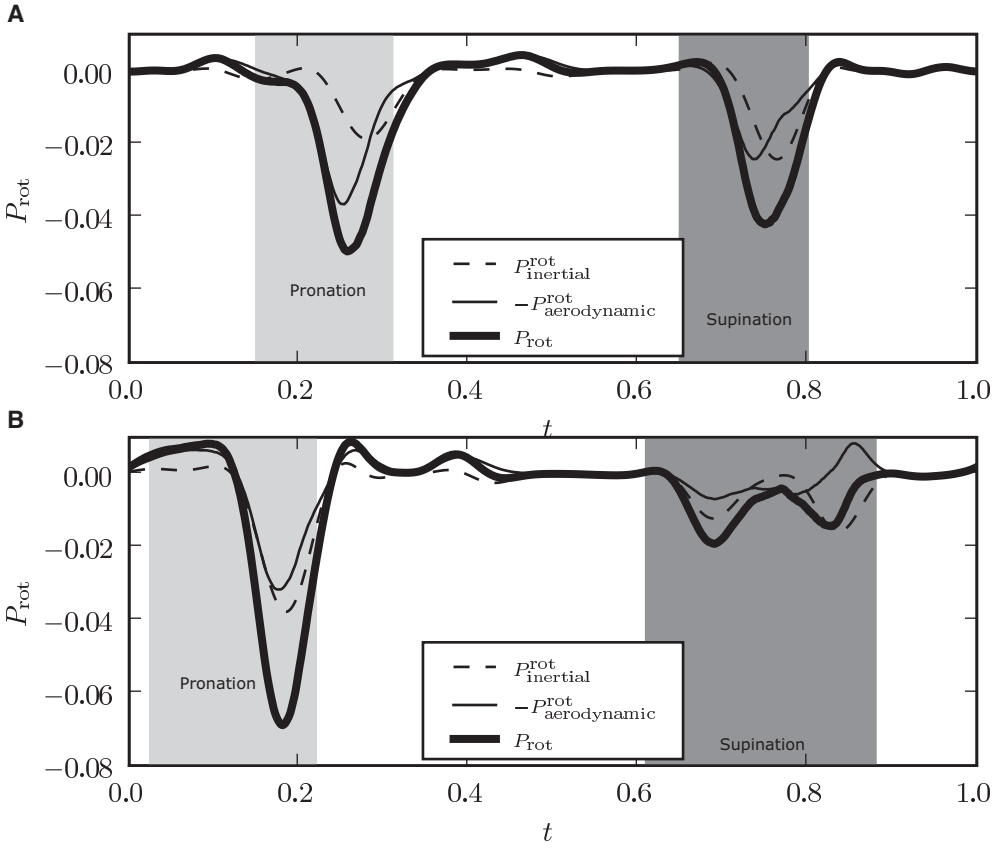

Figure 2.5: The averaged values of $P_{\rm rot}$ for the fore-, (**A**), and hind-, (**B**), wings as a function of time, pronation and supination are at marked regions. The average value is taken over 50 periods. Also shown in the figure are $-P^{\rm rot}_{\rm aerodynamic}$ and $P^{\rm rot}_{\rm inertial}$ from Eq. 2.2. Time is in the unit of the flapping period, and $P_{\rm rot}$ dimensions, power per unit length, in the unit of the ratio of the weight of the insect and the timescale.

2.4 Passive Wing Pitch Reversal in Dragonfly Flight

In Fig. 2.5, we show the rotational power about the torsion axis as a function of time for the fore- and hind- wings respectively. These are calculated using Eq. 2.2 for 50 wing strokes and then averaged. Shown are both the contribution from the aerodynamics and the wing inertia. During both pronation and supination, $P_{\rm rot}$ has strong negative peaks that are greater in magnitude during pronation than during supination. The negative peaks indicate that the fluid,

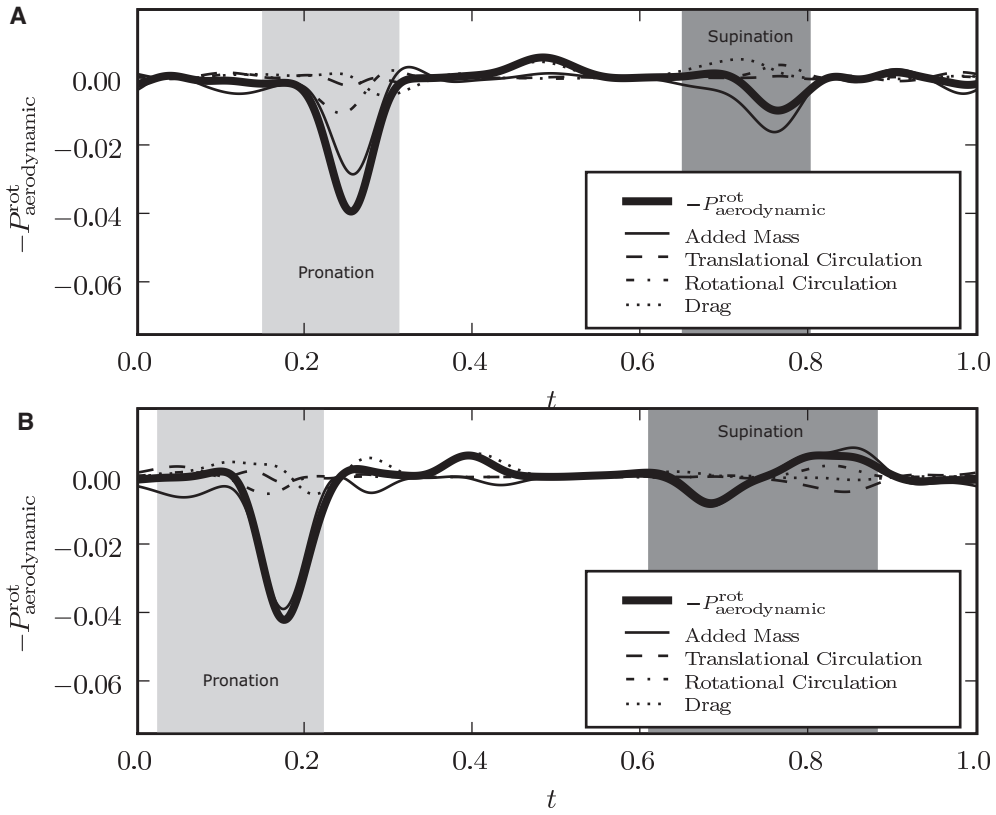

Figure 2.6: In (**A**) and (**B**) we show $-P^{\text{rot}}_{\text{aerodynamic}}$ and its components for the fore- and hind- wings, respectively. The units of time and $-P^{\text{rot}}_{\text{aerodynamic}}$ are the same as in Fig. 2.5.

by doing work on the wings, actually aids, rather than resists, the wing pitch reversal. This shows that the wing pitch reversal is passive. Both inertial and aerodynamic effects have a tendency of pitching the wing in the proper direction, but in this case, aerodynamic effects dominate.

In Fig. 2.6, we see that for both wings, the added mass term dominates all other terms at both pronation and supination. The next dominant term is the rotational circulation term which aids passivity at pronation of the wings and opposes it at supination. The dissipative and rotational circulation terms only play minor roles in wing pitch reversal. However, they tend to oppose wing pitch reversal in the beginning of the pronation and supination and aid

it in the latter half of it. We therefore see that for the dragonfly kinematics, the passivity of wing pitch reversal is determined, to a large extent, by added mass and rotational circulation effects, with other terms playing a minor, but discernible, role.

2.5 Passive Wing Pitch Reversal in Other Insects

To see if the described passive mechanism for wing pitch reversal occurs in other insects, we analyze kinematics for a hovering fruit fly [30], hovering hawkmoth [31], and simplified dragonfly hovering kinematics [32]. As with the dragonfly, we calculate P_{rot} using Eq. 2.2 for a chord-wise cross section of the wing at 66% the wingspan. In order to model aerodynamic forces, we use the quasi-steady model from Eq. 6.27. For the simplified hovering kinematics, the morphological parameters of the dragonfly studied in the previous section are used. For the fruit fly and hawkmoth, actual morphology of the insects is employed [30, 35].

Results for P_{rot} along with each wing motion are shown in Fig. 2.7. For each of the kinematics, we see similar results to the dragonfly kinematics. Large negative peaks occur close to the wing pitch reversal, which is nearly coincidental with stroke reversal. Because of the relatively light wings of dragonflies and fruit flies (Figs. 2.7A and 2.7E), the aerodynamic component of P_{rot} is greater than the inertial one. For the hawkmoth, however, the inertial component becomes dominant. This is expected, as the hawkmoth has a large wing mass relative to the body mass.

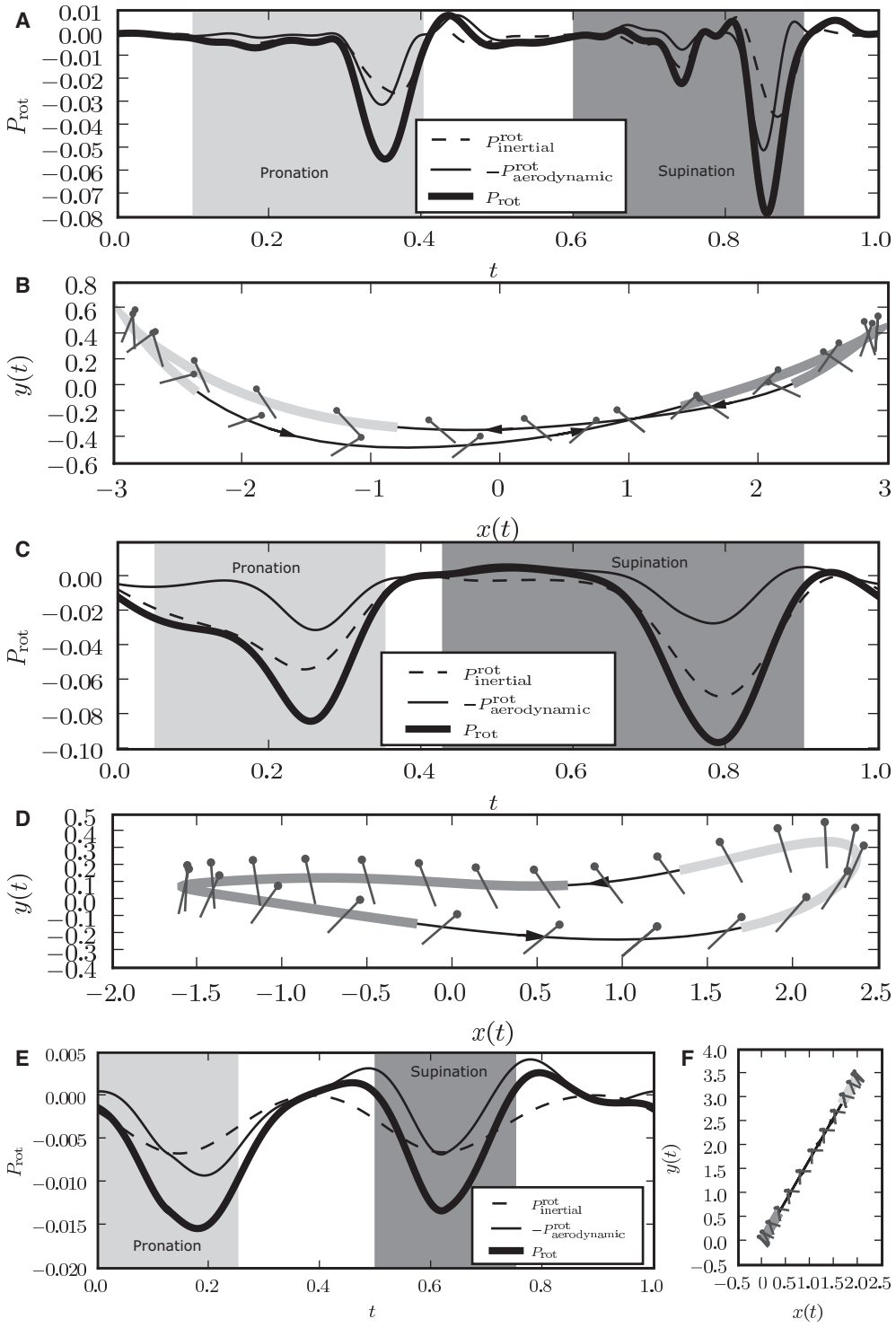

Figure 2.7: Wing motions and quasi-steady $P_{\rm rot}$ for a fruit fly, (**A**)–(**B**), hawkmoth, (**C**)–(**D**), and simplified dragonfly hovering kinematics, (**E**)–(**F**). The units of time and $P_{\rm rot}$ are the same as in Fig. 2.5.

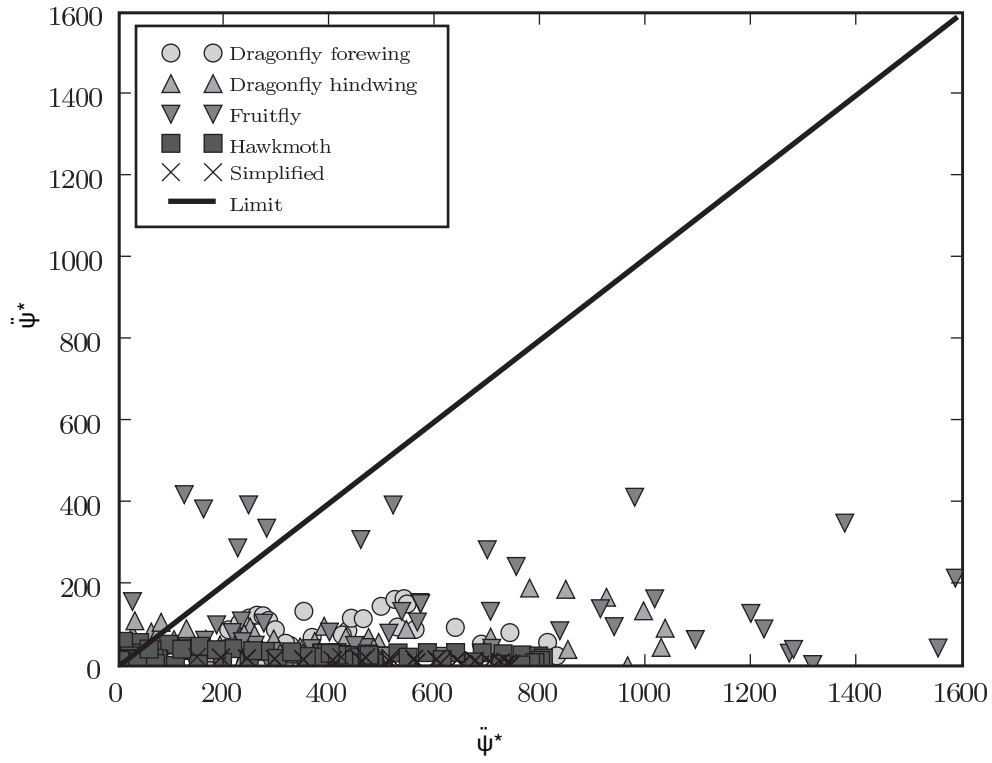

Figure 2.8: Plot of $\ddot{\psi}^* = \frac{md_{\mathrm{cm}}+m_{\mathrm{a}}d_{\mathrm{gc}}}{I_{\mathrm{cm}}+I_{\mathrm{a}}}|a_{y'}|$ against $|\ddot{\psi}|$. The region under the solid line is the limit where inertial and added mass effects aid in wing pitch reversal. The points represent snapshots of the wing kinematics during pronation and supination, i.e. they are values of $\ddot{\psi}(t)$ and $a_{y'}(t)$ for a particular motion at a particular t.

2.6 Quasi-steady Analysis of Wing Pitch Reversal

The fact that passive wing pitch reversal is observed for these different wing kinematics suggests the existence of a general explanation. The passive pitching can be intuitively explained as follows. When the wing decelerates prior to stroke reversal, the fluid continues to move forward and pushes the center of the wing forward causing it to rotate about the torsion axis. This is the added-mass effect. As the wing continues to pitch after stroke reversal, lift, drag and added mass forces on the wing will all be directed in a way that will cause pitch reversal to occur passively. Below, we analyze the relative importance of these

terms in the framework of the quasi-steady model. We do this by inspecting the components in the quasi-steady expression for P_{rot} term by term.

If the wing is thin, $\frac{b}{a} \ll 1$, then the added mass coefficients can be simplified as $m_{11} \to 0$, $m_{22} \to m_{\text{a}}$. Hence, we can combine Eqs. 2.2 and 6.27 to write P_{rot} in the co-rotating coordinate system as,

$$P_{\text{rot}} = [\underbrace{(I_{\text{cm}} + I_{\text{a}})\ddot{\psi} - (md_{\text{cm}} + m_{\text{a}}d_{\text{gc}})a_{y'} + m_{\text{a}}v_{x'}v_{y'}}_{\text{inertial and added mass}} \underbrace{-d_{\text{gc}}F^{\nu}_{y'} + \tau^{\nu}}_{\text{dissipative}} \underbrace{+\rho_f d_{\text{gc}}v_{x'}\Gamma}_{\text{circulation}}]\dot{\psi}. \quad (2.3)$$

All terms in the equation appear as defined previously. We analyze Eq. 2.3 term by term, and seek criteria that, when satisfied, result in wing pitch reversal being passive.

Near stroke reversal the translational velocity of the wing is small, and therefore drag and circulatory terms will be small because of their velocity dependence. The terms $(I_{\text{cm}} + I_{\text{a}})\ddot{\psi}\dot{\psi} - (md_{\text{cm}} + m_{\text{a}}d_{\text{gc}})a_{y'}\dot{\psi}$ are independent of velocity and dependent on the acceleration of the wing. Therefore, when pitch reversal occurs in this region added mass and inertial terms dominate P_{rot}. We therefore, first, consider the balance of these two dominant terms. They aid the wing pitch when their sum is negative, this occurs when

$$|\ddot{\psi}| \leq \frac{md_{\text{cm}} + m_{\text{a}}d_{\text{gc}}}{I_{\text{cm}} + I_{\text{a}}}|a_{y'}|. \quad (2.4)$$

These terms determine a limit on angular acceleration below which added mass and inertial effects aid in pitch reversal. In Fig. 2.8, we plot $\ddot{\psi}^* = \frac{md_{\text{cm}}+m_{\text{a}}d_{\text{gc}}}{I_{\text{cm}}+I_{\text{a}}}|a_{y'}|$ against $|\ddot{\psi}|$ for snapshots in time during the pronation and supination of the previously mentioned wing kinematics. Added mass and inertial effects aid wing pitch reversal for any points that lie below the identity and oppose it otherwise. As we see from the figure, most points lie below this line. Therefore these terms tend to aid pitch reversal during both pronation and supination. The torque

due to these terms will pitch the wing such that the leading edge of the wing remains the edge near the torsional axis.

As mentioned, the drag and circulatory terms are small near stroke reversal, however, they can play a role in wing pitching if pitch reversal occurs sufficiently away from stroke reversal. From Eq. 6.26, we see that τ^{ν} will always oppose wing rotation, but is negligible. The other drag term $\vec{F}^{\nu} \propto -|\vec{v}|\vec{v}$ will oppose the translational motion of the wing. Therefore, if pitch reversal occurs before stroke reversal, this term opposes pitching, and aids it after stroke reversal. This is in agreement with observations in Fig. 2.6.

The circulation term can be decomposed into translational, $P^{\text{rot}}_{\Gamma_T}$, and the rotational, $P^{\text{rot}}_{\Gamma_R}$, components. Following Eq. 6.25,

$$P^{\text{rot}}_{\Gamma_T} = -2C_T\rho_f d_{\text{gc}} d_{\text{le}} \frac{v^2_{x'} v_{y'}}{|\vec{v}|}\dot{\psi} \tag{2.5}$$

This term aids pitch reversal when the sign of $v_{y'}$ and $\dot{\psi}$ are the same. This occurs when the trailing edge is rotating away from the direction that it is moving, as is the case when the wing pitches after stroke reversal. $P^{\text{rot}}_{\Gamma_R}$ can be calculated from

$$P^{\text{rot}}_{\Gamma_R} = 2C_R\rho_f d_{\text{gc}} d^2_{\text{le}} v_{x'}\dot{\psi}^2. \tag{2.6}$$

Because of its linear dependence in velocity, its magnitude is typically larger than either drag or translational circulation near wing reversal. The sign of P_{Γ} is determined by the sign of $v_{x'}$, and opposes wing pitching unless the leading edge is changed from near the torsion axis to the other edge of the wing, which can happen momentarily during the pitch reversal (Fig. 2.4). In Fig. 2.6 we see that translational circulation aids wing pitch reversal in the latter half of stokes, past stroke reversal. Rotational circulation only helps rotate the wing during pronation, where the leading edge temporarily changes from away the torsion

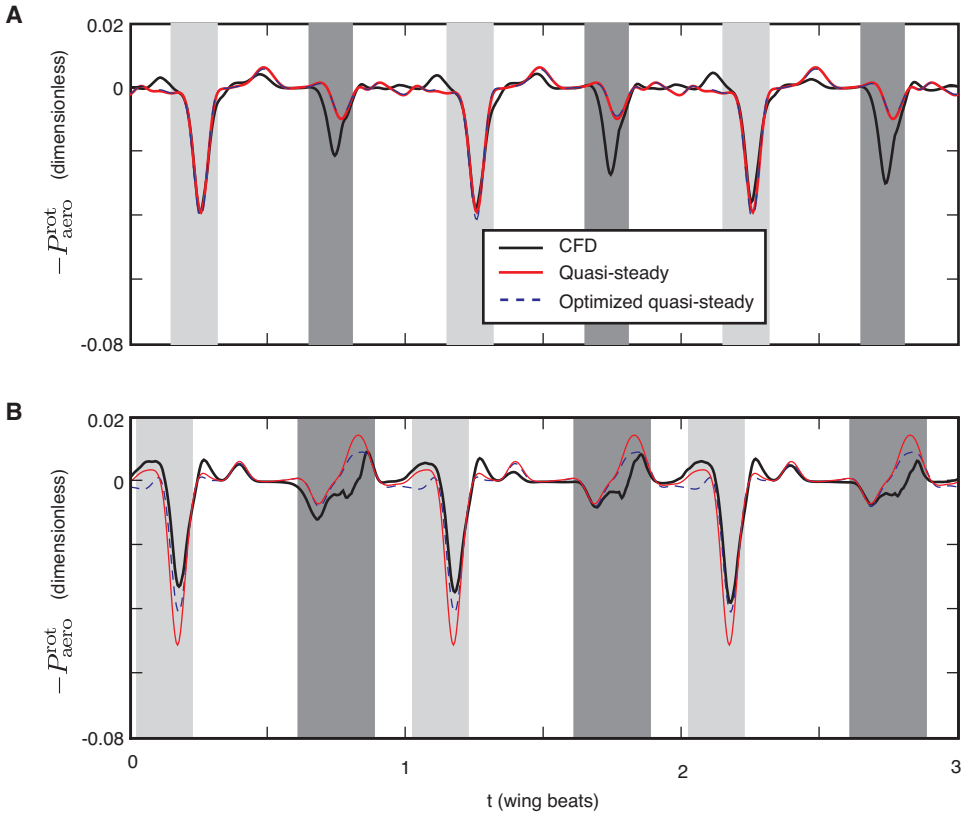

Figure 2.9: Comparison of $-P^{\text{rot}}_{\text{aerodynamic}}$ calculated using IIM to the falling paper model for the fore-, (**A**), and hind-wing, (**B**), respectively. The parameters in the quasi-steady model match those from [36] with the exception of C_R. $C_R = 2.58$ for the forewing and 0.90 for the hindwing. The units of time and $P^{\text{rot}}_{\text{aerodynamic}}$ are the same as in Fig. 2.5.

axis, and has a tendency of opposing it during supination, where the leading edge remains unchanged.

2.6.1 Optimization of Quasi-steady Parameters

In §6.3.1 we compare the forces computed on dragonfly wings using the quasi-steady model to simulations of the immersed interface method. We find that because the wings generate a net downward jet, that is not present in the quasi-steady model discrepancies in force predictions coincide with the wings cross-

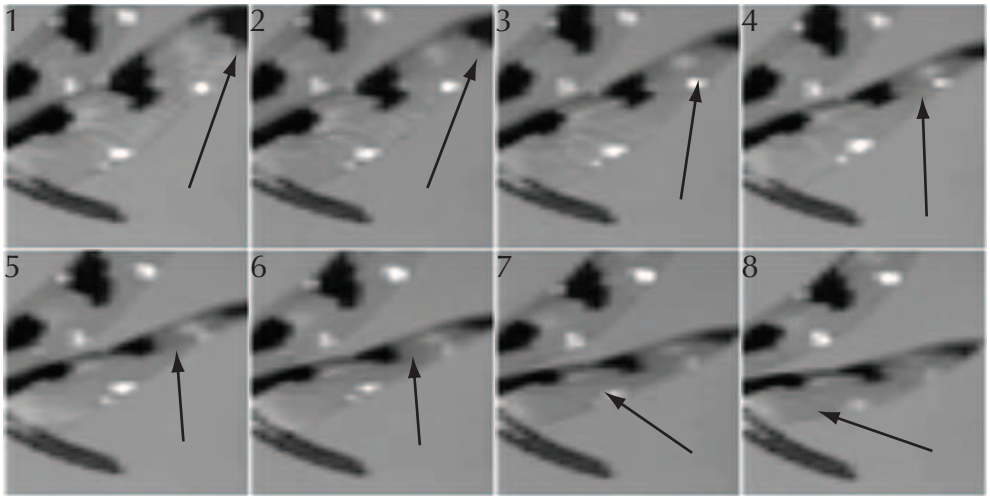

Figure 2.10: Torsional wave propagating along trailing edge of wing from base to tip near pronation.

ing this jet near supination. To compensate for this effect we determine quasi-steady parameter values that minimize the difference between the quasi-steady and CFD results for $P^{\text{rot}}_{\text{aerodynamic}}$. We find that only optimization of C_R yields significant improvements in quasi-steady model predictions. In Fig. 2.9, we show $P^{\text{rot}}_{\text{aerodynamic}}$ compared between direct simulations and the quasi-steady model along with values of the optimized quasi-steady model parameters. Importantly, the peaks in the quasi-steady model have the same sign as in the direct simulations. Furthermore, the net effect of these wing interaction effects is to make the wing motion "more passive". Since we are mainly interested in the sign of these peaks when determining the passive nature of the wing pitching, we will make use of this quasi-steady model in our general analysis in §2.6.

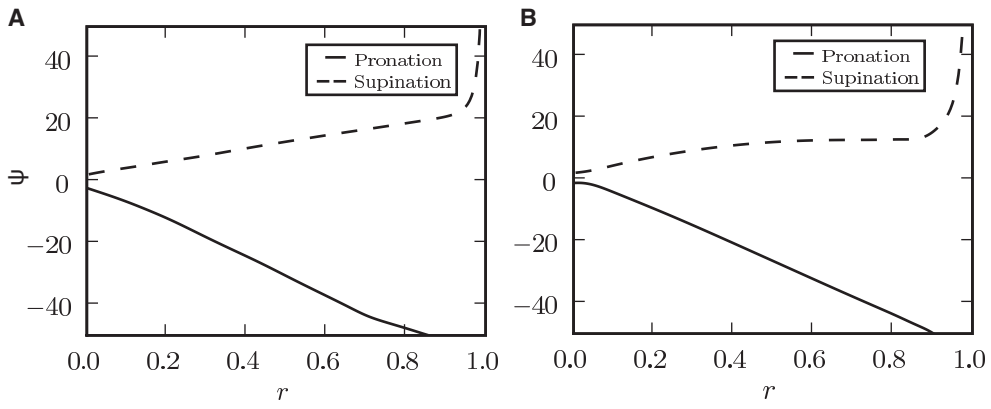

Figure 2.11: Span-wise dependence of ψ on r, the fractional distance along the span of the wing. $\psi(r)$ is calculated by integrating the torque about the wing's center of mass over pronation and supination regions. During pronation, the wing is reoriented so that ψ goes from a large value to a small one. During supination, the opposite happens. Therefore, at both pronation and supination the wing elements closer to the wingtip have a tendency of twisting ahead of those nearer to the base and thus create a torsional wave.

2.7 Signature of Passive Wing Reversal

A signature of active versus passive wing pitch reversal is the direction of the torsional wave traveling along the trailing edge of the wing during wing reversal. If the wave propagates from the root to tip, then the wing pitch reversal is likely to be activated by the muscle, which is applied near the wing root. Such a wave was previously observed in the study of a desert locust, *Schistocerca gregaria* [12]. If, on the other hand, the wave propagates from near the tip to the root, then this suggests that the aerodynamic force, which is maximal near the tip, is responsible for the turning motion. This type of torsional wave was observed in [29] for the wings of Diptera during passive wing rotation observed in those insects. In Fig. 2.10, we show a blowup of several frames captured for the tethered dragonfly around the transition from up-stroke to down-stroke. We observe a torsional wave propagating along the trailing edge of the wing starting near the wing-tip ending near the wing base. This provides additional

evidence for the passive nature of the wing pitching as analyzed above.

The torsion along the length of the wing is directly related to the angular rotation of each wing segment comprising it. Using the blade-element approximation and the wing shape of the dragonfly, we determine, for each segment, the torque caused by aerodynamic forces and the insect muscle. The muscle forces act at the torsion axis and are calculated by ensuring that the translational acceleration of the wing matches the wing kinematics, $\vec{F}_{\text{insect}} = m\vec{a} - \vec{F}_{\text{aerodynamic}}$. The torque about the center of mass of a segment is then

$$\begin{aligned} \tau &= \tau_{\text{gc}} + (d_{\text{cm}} - d_{\text{gc}})(F_y \cos\psi - F_x \sin\psi) + (d_{\text{cm}} - d_{\text{ta}})(F_y^{\text{insect}} \cos\psi - F_x^{\text{insect}} \sin\psi) \\ &= I_{\text{cm}}(r)\ddot{\psi}. \end{aligned} \tag{2.7}$$

We approximate the wing as having uniform surface mass density. Thus, the moment of inertia of a blade element is $I_{\text{cm}} \propto c(r)^3$ at span r. Eq. 2.7 determines the pitching motion of each blade element independently of the others. We integrate this equation over pronation and supination to determine how independent blade elements would move just based on aerodynamic force, and the prescription of the torsion axis motion.

In Fig. 2.11, we show the results integrating Eq. 2.7 for the fore- and hindwings of the dragonfly. We see that if each blade element is allowed to move independently, then the tip of the wing will move ahead of the base. Since a wing is continuous, this will induce a torsional wave along the wingspan during pronation and supination that travels from the wing tip to the base, as seen in Fig. 2.10.

2.8 Summary

We have analyzed the wing pitch reversal in observed hovering wing kinematics for 4 different insects. By calculating the rotational power required to pitch the wing using direct numerical simulation and quasi-steady analysis, we have shown that in all these cases, the wing pitch reversal is aided by the aerodynamic torque and wing inertia. The passive wing pitch is consistent with the observed torsional wave which propagates from near the wing tip to wing root. Using a quasi-steady analysis, we identified the main component of the fluid forces that is responsible for the passive wing pitching. We have further determined the relative importance of the aerodynamic and the wing inertial force in these different wing motions.

The observed wing pitching in these cases does not require additional power input from the muscles. This suggests that while insects have the ability to pitch the wing actively, during steady hovering flight, they can benefit from the aerodynamic force and inertia to simplify the control of wing pitching.

CHAPTER 3

MULTIPLE VIEW MOTION RECONSTRUCTION OF *DROSOPHILA* FLIGHT

3.1 Introduction [1]

Flying insects primarily control their flight path with very subtle changes to how their wings slice through the air. By modifying their wing kinematics by just a few degrees they are able to induce spectacular maneuvers such as sharp turns at rates of thousands of degrees per second. The goal of this work is to quantify how insects actuate their wings during flight. This requires unprecedented accuracy in the measurements of their movements. Further, because our ultimate goal is to understand flight maneuvers we require measurements of freely flying insects.

In this chapter, we briefly describe the method that we developed to track the pose of freely flying *D. melanogaster*. Additional details may be found in [25, 37]. We then in detail introduce how we visualize these data and quantify the measurement uncertainties within this method.

3.2 Experimental Apparatus

Flight sequences of freely flying *D. melanogaster* are recorded using the apparatus shown in Fig. 3.1. Three synchronized high speed cameras (Phantom v7.1,

[1] Part of the work presented in this chapter originally appeared in Ristroph, Berman, Bergou, Wang & Cohen *J. Exp. Biol.*, **212**, (2009).

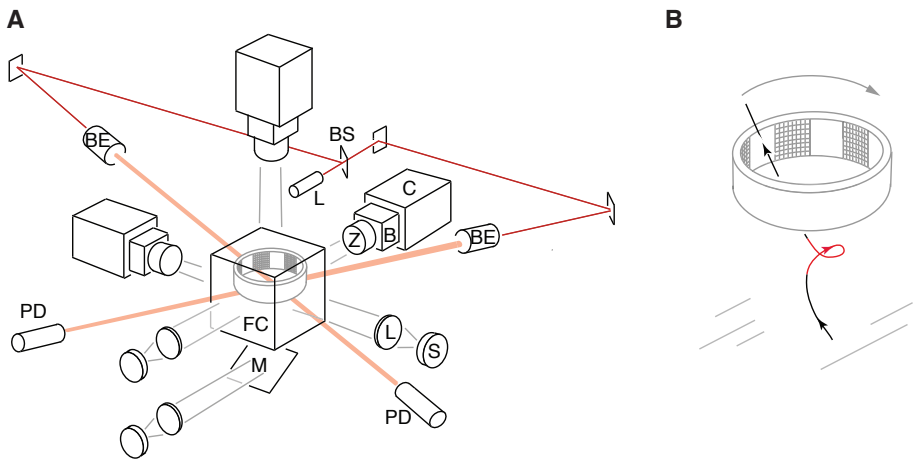

Figure 3.1: (**A**) The experimental apparatus used to record maneuvers performed by freely flying fruit flies consists of three orthogonally placed cameras (C), focused on a common volume. Flies are placed in a flight chamber (FC) where filming is triggered by the simultaneously breaking of crossed laser beams (red lines). An LED arena in the center of the chamber induces flies to perform maneuvers. The additional labeled components of the setup are beam expander (BE), lens (L), back-lighting diode (S), bellows lens (B), lens (Z), laser (L), mirror (M) and photo-detector (PD) (**B**) The LED arena is built from ten panels of light emitting diodes arranged in a circle. Each panel consists of 8×8 grid of diodes. A rotating bar pattern is displayed to induce the flies to perform turns. *Image courtesy of Leif Ristroph*

Vision Research, Inc., Wayne, NJ USA) each capture 512×512 pixel 12-bit gray scale images at 8000 frames per second (fps). This setup enables us to capture 30–40 images per wing beat of *Drosophila*, which have a flapping frequency of 200-260 Hz. The cameras are aligned orthogonally to focus on a square filming volume 1–2 cm in length. Thus, the resolution of the captured insect body, $2mm$, is usually about 80 pixels long. Due to stringent lighting requirements, each camera is back-lighted with a bright light source (LEDs, Diamond Dragon, OSRAM Opto Semiconductor, Sunnyvale, CA USA). Thus, silhouettes of flies are recorded by the cameras. Flies are placed within a square chamber 12 cm in length that encompasses the filming volume. A pair of laser beams are crossed in the filming volume. These beams trigger filming when a fly breaks both si-

Figure 3.2: We show the top-view of a recorded frame of a fruit fly in free-flight (left). We are able to automatically remove the background of the image through a median filter (right).

multaneously. The back-lighting and laser (HeNe, Thorlabs, Newton, NJ USA) are chosen to be red (wavelength greater than 600 nm) in order to minimize the visual stimulus to the insects, which have poor sensitivity to light of long wavelength [38]. The optional LED arena in Fig. 3.1B consists of ten panels of light emitting diodes. Each panel has an 8×8 grid of diodes. When filming is triggered, a rotating strip pattern is displayed on the LED arena. This pattern visually stimulates the fly to perform a turn [27].

Additional experimental details may be found in [25].

3.3 The Visual Hull

Motion approximation from image sequences taken by multiple synchronized cameras is a very mature subject in the computer vision community. The technology evolved primarily for motion tracking of human performers and so, until recently [25,39,40], has been underutilized by the biolocomotion community.

To recover the three-dimensional motion of the fruit fly from the recorded image sequences, we use the concept of the maximum convex hull or visual hull [41]. This volume corresponds the maximum volume that is consistent with fly silhouettes recorded by each of the cameras.

To determine the visual hull from each frame of the image sequence, we first segment the images to isolate the shadow of the fly from the background. The relative uniformity of the background enables us to accomplish this fully automatically. We first compute the approximate the median image, $\bar{I}(x, y)$, of a random sample of images, $I_n(x, y)$ for $n = 1..N$ (where N is usually 100), from each video. To ensure that thresholding is insensitive to subtly varying lighting conditions we also compute the pixel-wise median absolute deviation, $\sigma(x, y)$, of the sequence. We clip $\sigma(x, y)$ to ensure that it is neither too high or too low. Then, we threshold foreground segments, $F_n(x, y)$, within the image sequence with,

$$F_n(x,y) = \begin{cases} I_n(x,y) & \text{if } \left|I_n(x,y) - \bar{I}(x,y)\right| \geq 3\sigma(x,y) \\ 0 & \text{otherwise} \end{cases} . \tag{3.1}$$

The largest connected regions within F_n are found using the binary Watershed algorithm and all other regions are set to 0. We show this technique applied to a frame of a hovering fruit fly in in Fig. 3.2.

We can determine the approximate three-dimensional volume occupied by the fly from its captured shadows. For each frame of the recorded image sequences, we extend the fruit flies shadow that is found by image segmentation (Eq. 3.1). We then extend these shadows in the in the direction from where it is cast. This direction a shadow is extended corresponds to the axial orientation of the corresponding camera in the lab frame. The extended shadows form

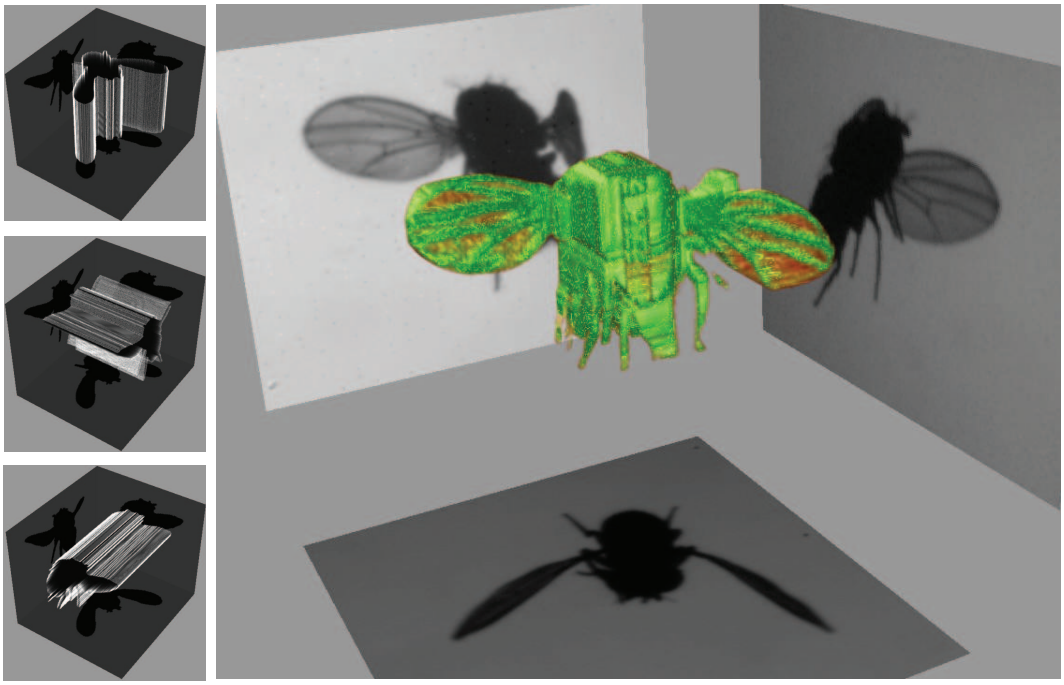

Figure 3.3: For each frame captured by the apparatus (Fig. 3.1), we extend the fruit fly silhouette in the direction it is cast from. The intersection of these extended shadows from all recording cameras forms the visual hull of the fruit fly. The colors of the visual hull are determined by the intensities in the shadows.

cylinders with cross-sections that correspond to the silhouettes (see Fig. 3.3). Extending the shadows in this way neglects perspective in the images, however, the focal length of the cameras is much longer then each side of the filming volume, therefore, this method results in less than 5% distortion of lengths when compared to more accurate methods.

The intersection of the extended shadows forms the visual hull of the fly (Fig. 3.3). This volume is the maximum volume that can be occupied by the fly that cast the shadows [41, 42]. To form the visual hull, the (square) pixels in the images map to (three dimensional cube) voxels in the visual hull.

Because the filming apparatus records the shadows of flies very little intensity information is available in the images. The wings of a fruit fly, however,

are translucent. Therefore, their intensity is distinct from the opaque fly body. Further, because the veins on the wings are also opaque in the captured image sequences (see Fig. 3.2) the venation pattern is visible on the wings. To use this intensity information from the images we form the visual hull of the fly by,

$$V(x,y,z) = \begin{cases} Z(x,y) & \text{if } Z(x,y) \leq Y(x,z) \text{ and } Z(x,y) \leq X(y,z) \\ Y(x,z) & \text{if } Y(x,z) < Z(x,y) \text{ and } Y(x,z) \leq X(y,z) \\ X(y,z) & \text{if } X(x,y) < Z(x,y) \text{ and } X(y,z) < Y(x,z) \\ 0 & \text{otherwise} \end{cases}, \tag{3.2}$$

where $V(x,y,z)$ is the visual hull and $X(y,z)$, $Y(x,z)$, $Z(x,y)$ are the images captured by the three orthogonally placed cameras. By forming the visual hull using Eq. 3.2, we ensure that a voxel of the visual hull has the intensity equal to the minimum intensity of the intersecting shadows. To render the visual hull we volume render the resulting three-dimensional voxel image using [43]. In this way the intensity values approximated from 3.2 are mapped to colors in Fig. 3.3.

3.4 Tracking of Flight Sequences

The wings of fruit flies are relatively rigid. In addition, we find that during a flight sequence flies do not significantly alter the position of their legs and body segments. We, therefore, recover the kinematics of a fly as six degrees of freedom (DOF) describing the position and orientation of their body centroid relative to the lab frame. Similarly, we also measure the 6 (DOF) of for each wing centroid.

Figure 3.4: The visual hull clustered into four segments. The left wing is shown in blue, the right wing in red, while the body is shown in green.

To extract the insects kinematics from a flight image sequence, we compute the visual hull for each set of images captured by the recording apparatus (see §3.3). Because the wings of the fruit fly are extend out from the body we cluster this three-dimensional image using k-means clustering [44]. This allows us to identify the two wings and the body. The position and orientations of these segments is then computed relative to the lab frame. Details of how we recover poses of the fly from these the clustered visual hull may be found in [25, 37].

The Euler angles used to describe the orientation of the fly and its wings relative to the lab frame are shown in Fig. 3.5. We define these angles by describing the sequence of rotations that orients the wings and body relative to the lab frame (see [45, 46] for a similar treatment). The body is initially oriented so that its longitudinal axis (the vector from the thorax to the head) coincides with the x-axis and the wing attachment points are collinear with the y-axis. Simi-

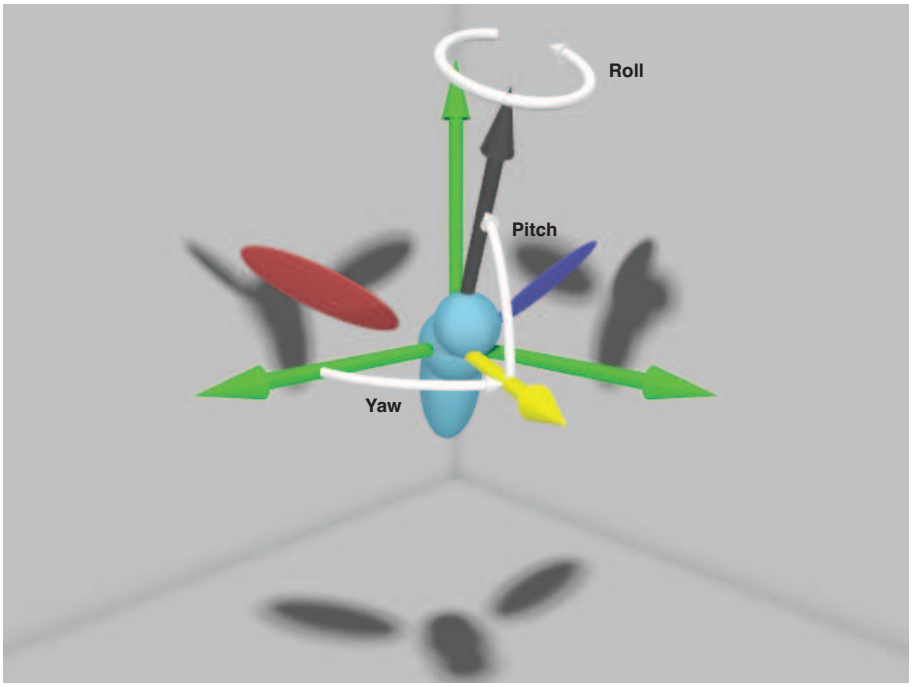

Figure 3.5: The orientation of the fly to the lab frame are depicted by three Euler angles. The body orientation of a fruit fly relative to the lab frame are named the yaw, pitch and roll. Similar Euler angles can be used to describe the wing orientations to the lab frame, however, it is more useful to describe their orientations relative to the body.

larly, each wing is initially oriented so the x- and y-axes coincide with its span and chord, respectively. Positive x- is directed from the base to the tip of the wing, and positive y- is directed from the trailing edge to the leading edge of the wing. The sequence of rotations that orients the segments (body, left wing and right wing) to the lab frame are,

- Rotate counterclockwise by ψ about x-axis in fixed frame to arrive at ξ_1-frame. The rotation matrix, $\mathbf{R}_x$ describing this rotation is,

$$\mathbf{R}_x = \begin{pmatrix} 1 & 0 & 0 \\ 0 & \cos\psi & -\sin\psi \\ 0 & \sin\psi & \cos\psi \end{pmatrix}. \tag{3.3}$$

- Rotate clockwise by θ about y-axis in ξ_1 frame to arrive at ξ_2-frame. The rotation matrix, $\mathbf{R}_y$, describing this rotation is,

$$\mathbf{R}_y = \begin{pmatrix} \cos\theta & 0 & -\sin\theta \\ 0 & 1 & 0 \\ \sin\theta & 0 & \cos\theta \end{pmatrix}. \tag{3.4}$$

- Rotate counterclockwise by ϕ about z-axis in ξ_2 frame to arrive at lab frame. The rotation matrix, $\mathbf{R}_z$, describing this rotation is,

$$\mathbf{R}_z = \begin{pmatrix} \cos\phi & -\sin\phi & 0 \\ \sin\phi & \cos\phi & 0 \\ 0 & 0 & 1 \end{pmatrix}. \tag{3.5}$$

The full sequence of rotations to orient a segment from the fixed frame to the lab frame is,

$$\mathbf{R}(\phi, \theta, \psi) = \mathbf{R}_z(\phi)\mathbf{R}_y(\theta)\mathbf{R}_x(\psi) \tag{3.6}$$

When appropriate, we use subscripts, r, l and b to differentiate, respectively, between the Euler angles of the right wing, left wing and body. In Fig. 3.5 we show the Euler angles that describe the body orientation. These are named yaw, ϕ_b; body-pitch, θ_b; and roll, ψ_b.

3.4.1 Determining Wing Amplitude, Deviation and Pitch

Although the wing's orientation and position relative to the lab frame are the tracked quantities and are used in computing aerodynamic forces (see §6), their description using these six DOF is redundant. The wings are constrained to rotate about a hinge on the fly's thorax [18], therefore, the orientation of each

wing may be specified by just three DOF relative to the body. Here, we describe the Euler angles that specify these three DOF.

The orientation of an insect's wings relative its body is physiologically meaningful because flight muscles are located entirely within the thorax and do not extend into the wings [17,20,21]. Therefore, the driving muscles are in the body frame. Furthermore, insect flight muscles are mirror symmetric between the left and right wings and can be split into two groups: indirect flight muscles and direct flight muscles [22]. The large indirect flight muscles deform the thorax of fly and are chiefly responsible for the flapping motion of insect wings. The indirect or steering flight muscles are used to control flight and generate the perturbations to strokes that ultimately alter maneuvers. We take care to choose a coordinates that reflect the underlying fly physiology.

During steady free-flight, the longitudinal axis of *D. melanogaster* is oriented at approximately 60° to the horizontal [47,48]. To isolate the driving amplitude from the other directions, we describe the orientation of the wings relative to this body-pose. The Euler angles used to define this orientation are very similar to those that define orientations relative to the frame. The one exception is that the left and right wing are described in a mirror symmetric manner. Because of the similarly in coordinate definitions, we use the same variables to describe these angles relative to the lab and body frames. When we need to distinguish between the different frames, we use a superscript L or B that precedes the variable to specify, respectively, whether it is in the lab or body frame (e.g. ${}^{L}\phi_r$ versus ${}^{B}\phi_r$).

We show the Euler angles used to describe the wing orientation relative to the fly's body in Fig. 3.6. They are are named - amplitude, ${}^{B}\phi$; deviation, ${}^{B}\theta$;

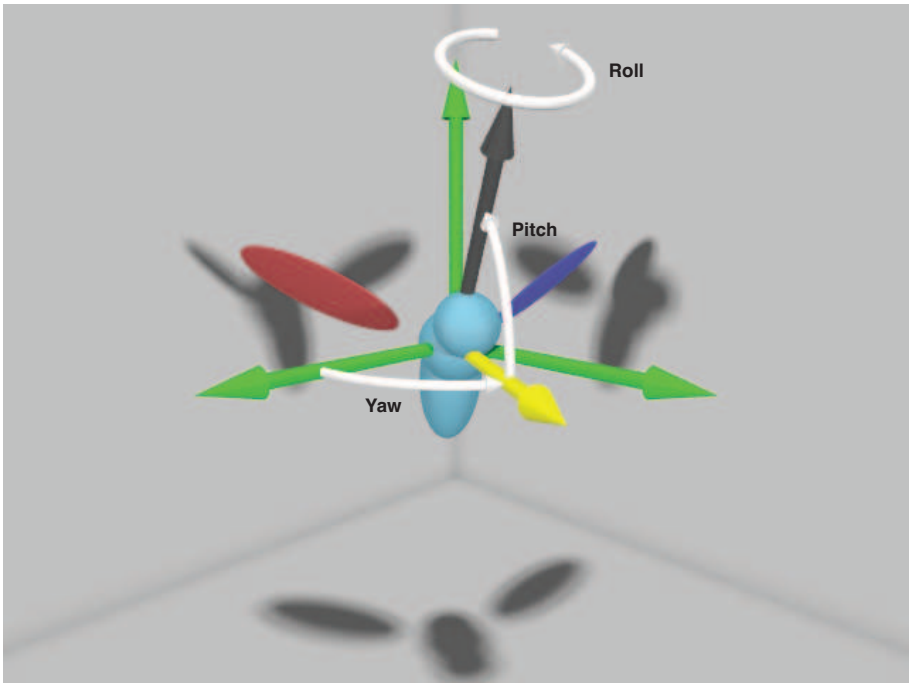

Figure 3.6: The wing orientation is described by the pitch, deviation and amplitude. The angles are oriented with respect to the body of the fruit fly and are mirror symmetric for the left and right wings. Above we show the Euler angles describing the orientation of the right wing.

and wing-pitch, ${}^{B}\psi$. These angles may be computed directly from the (tracked) lab frame coordinate by using Eq. 3.6. The rotation matrix that orients the right wing relative to the body may be computed by,

$$\mathbf{R}^{*}({}^{B}\phi_r, {}^{B}\theta_r, {}^{B}\psi_r) = \mathbf{R}^{-1}(\phi_b, \theta_b - 60^{\circ}, \psi_b)\mathbf{R}({}^{L}\phi_r, {}^{L}\theta_r, {}^{L}\psi_r), \tag{3.7}$$

where care is taken to find the orientation relative to the 60° inclined pose of the body. From R^{*}, the Euler angles that describe the wing's position are,

$$\begin{aligned}
{}^{B}\phi_r &= \begin{cases} -\tan^{-1}(\mathbf{R}^{*}_{2,1}, \mathbf{R}^{*}_{1,1}) & \text{if } {}^{B}\theta_r \neq \frac{\pi}{2} \\ 0 & \text{otherwise} \end{cases} \\
{}^{B}\theta_r &= \sin^{-1}\mathbf{R}^{*}_{3,1} \\
{}^{B}\psi_r &= \begin{cases} \tan^{-1}(\mathbf{R}^{*}_{3,2}, \mathbf{R}^{*}_{3,3}) & \text{if } {}^{B}\theta_r \neq \frac{\pi}{2} \\ \tan^{-1}(\mathbf{R}^{*}_{1,2}, \mathbf{R}^{*}_{1,3}) & \text{otherwise} \end{cases},
\end{aligned} \tag{3.8}$$

where subscripts on the rotation matrix indicate particular components of the matrix. For the left wing, we compute $\mathbf{R}^*$ identically to Eq. 3.7. Then

$$
\begin{aligned}
{}^B\phi_l &= \begin{cases} \tan^{-1}(\mathbf{R}^*_{2,1}, \mathbf{R}^*_{1,1}) & \text{if } {}^B\theta_l \neq \frac{\pi}{2} \\ 0 & \text{otherwise} \end{cases} \\
{}^B\theta_l &= \sin^{-1} \mathbf{R}^*_{3,1} \\
{}^B\psi_l &= \begin{cases} 180^\circ - \tan^{-1}(\mathbf{R}^*_{3,2}, \mathbf{R}^*_{3,3}) & \text{if } {}^B\theta_l \neq \frac{\pi}{2} \\ 180^\circ - \tan^{-1}(\mathbf{R}^*_{1,2}, \mathbf{R}^*_{1,3}) & \text{otherwise} \end{cases}
\end{aligned}
\quad . \tag{3.9}
$$

3.5 Visualization of Flight Sequences

To visualize the kinematics of the flight sequences reconstructed using HRMT [25], we map the recovered wing and body kinematics onto a virtual fly. In analog with the recovered kinematics, the virtual fly is modeled as a rigid body and two rigid wings. The body is represented by three ellipsoids, corresponding to the head, thorax and abdomen of the insect. The size of these segments is estimated from the images sequences used to reconstruct the kinematics. Each wing of the fly is represented by an ellipsoid. Two of the axes of the ellipsoid are matched to the chord and span of the insect. This is, once again, accomplished by estimating these quantities from the image sequences.

We visualize each frame of the kinematic sequence by rendering the virtual fly using [49]. In addition, we display the original frames captured by the filming apparatus (Fig. 3.1) in panels around the fly. The orientation of each panel corresponds to the orientation of the camera used to record the image sequence. Once rendered, these frames may be stitched together to depict the captured motion. To represent the motion of a fly in a figure, we render multiple re-

constructed poses of the insect within the same image. Similarly, the captured image frames are merged to match the panel images to the rendered poses.

3.6 Uncertainty in Kinematic Measurements

Flying insects are able to initiate complex maneuvers through very slight changes to their wing kinematics. To understand and characterize these maneuvers requires, not only accurate kinematic measurements, but also an understanding of the errors and limitations in of how these measurement are made. We, therefore, take great care to characterize the errors associated in the reconstruction of the poses of the fly. In this chapter, we describe the methods we use to characterize the measurement uncertainties on kinematic quantities. We also describe how systematic errors in the body roll, ψ_b, and measurements of the wing centroids, $\vec{x}_{r,l}$, are accounted for.

We model measurement of a kinematic quantity as,

$$\tilde{f}(t) = f(t) + X(t), \tag{3.10}$$

where $\tilde{f}(t)$ is the result of the measurement at time t and $f(t)$ is the true parameter value (also at time t). The measurement error, $X(t)$, is modeled as white noise,

$$\begin{aligned} E[X(t)] &= 0 \\ E[X(t_1)X(t_2)] &= \sigma(t)^2\delta(t_1 - t_2), \end{aligned} \tag{3.11}$$

where E is the expectation value, and $\sigma(t)$ is the variance of the random variable. For our measurements, we find that $\sigma(t)^2$ does not normally vary in time.

Measurements of the error profile (see [25] and method described in §3.6.2) confirm that this is an accurate model for random measurement errors. Systematic errors in the data acquisition are dealt with separately in §3.7.

3.6.1 Error Covariance Matrix from Kinematic Measurements

Because we can model measurement errors as white noise (Eq. 3.11), the error covariance matrix (ECM) of the measured kinematics can be simply estimated directly from the data. For two time series of measured kinematic variables, $\tilde{f}_i = \tilde{f}(t_i)$ and $\tilde{g}(t_i)$, with corresponding errors X_i and Y_i the 2×2 ECM is defined as,

$$\sigma_{xy} \equiv E[X_i Y_i], \tag{3.12}$$

where E is the expectation value of the random variables. By using a finite difference stencil to numerically differentiate each time series we amplify the errors. Specifically, by applying the second order derivative stencil to our data, we can show that,

$$\tilde{f}_{i+1} - 2\tilde{f}_i + \tilde{f}_{i-1} = \Delta t^2 \ddot{f}(t_i) + X_{i+1} - 2X_i + X_{i-1}, \tag{3.13}$$

where Δt is the time-step of the measurement, and $\ddot{f}(t_i)$ is the true derivative of the signal at time t_i. Because $\Delta t^2 \ddot{f}(t_i)$ is proportional to the discretization it is much reduced compared to the value of the random variables. Therefore, this term may be neglected in the approximation. Then the ECM can be found

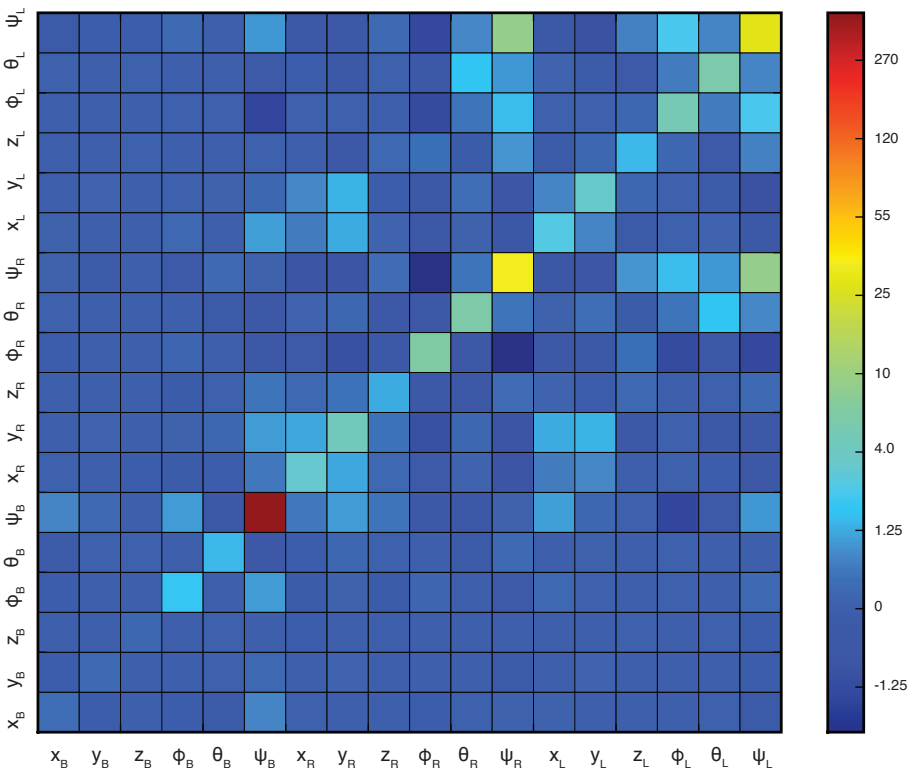

Figure 3.7: We estimate the error covariance matrix (ECM) using kinematic measurements of 12 flight sequences, totaling 5883 fly poses. We show the values of the ECM using a checkerboard plot. The covariance matrix is nearly diagonal as can be seen by the relatively high intensity of diagonal components compared to off-diagonal ones. Slight correlations exist between the errors in left and right wing's pitch angles, $\psi_{r,l}$.

estimated as,

$$\begin{aligned}
\sigma_{xy} &= \frac{1}{6}\mathrm{cov}(\tilde{f}_{i+1} - 2\tilde{f}_i + \tilde{f}_{i-1}, \tilde{g}_{i+1} - 2\tilde{g}_i + \tilde{g}_{i-1}) \\
&= \frac{1}{6}\mathrm{cov}(X_{i+1} - 2X_i + X_{i-1}, Y_{i+1} - 2Y_i + Y_{i-1}) \\
&= \frac{1}{6}\left(\mathrm{cov}(X_{i+1}Y_{i+1}) + 4\mathrm{cov}(X_iY_i) + \mathrm{cov}(Y_{i-1}X_{i-1})\right) \\
&= \mathrm{cov}(Y_iX_i), \qquad (3.14)
\end{aligned}$$

where the first line is the estimate we use and the others show the derivation of this formula. In Eq. 3.14, we use the fact that white noise is homogeneous in time (Eq. 3.11).

Table 3.1: The variance of the measurement uncertainties are estimated for each of the measured kinematic variables for the right wing, left wing and fly body. The estimates are computed directly from 12 distinct flight sequences totaling 5883 different poses of the fly.

Segment	$\sigma_{\vec{x}}$ (pixel)	σ_{ϕ} (°)	σ_{θ} (°)	σ_{ψ} (°)
Body	±0.5	±1.4	±1.2	±20
Wings	±2	±3	±2.5	±5.5

We show the estimate of the full 18×18 ECM from 12 distinct flight sequences totaling 5883 tracked poses in Fig. 3.7. The data is summarized as a checkerboard plot, where for each pair of variables the color of the checker represents the covariance between them. The colors are on a logarithmic scale due to the large separation of error scales that appear. Of importance is that the ECM is close to diagonal: the diagonal elements are larger than off-diagonal ones by at least a factor of two. This indicates that the measurement uncertainties may be summarized by diagonal elements alone.

In Tbl. 3.1 we quantitatively summarize estimates of the variances of the random error in the measured flight sequences. These values correspond to the diagonal elements of Fig. 3.7. As can be seen random errors in position are estimated to be within a few pixels and a few degrees for orientation angles. One notable exception is the roll angle of the body, ψ_b. The uncertainty on this Euler angle is measured to be 20°. This is because the fly body is highly symmetric for rotations about its longitudinal axis and therefore this quantity is very difficult to measure directly. In §3.7.1 we show how we compensate for the uncertainty in this measurement.

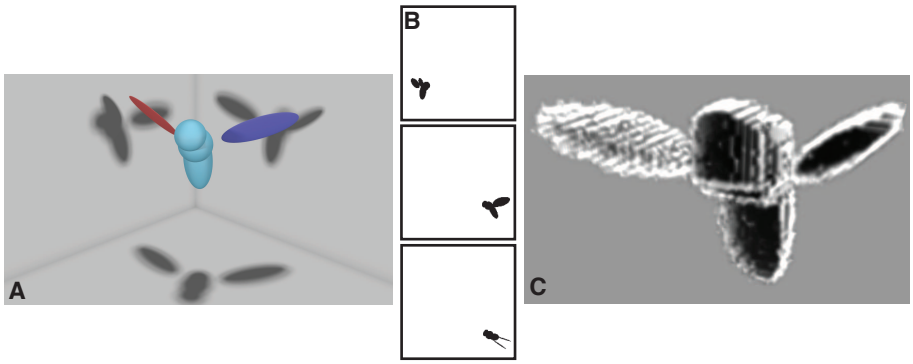

Figure 3.8: We prescribe kinematics to the virtual fly, compute the shadows of this fly and use HRMT to track the kinematics. We then compare the tracked kinematics to the prescribed one to validate the algorithm and measure the errors in reconstructing the three-dimensional kinematics.

3.6.2 Error Variances from Virtual Fly Pose

Although we can estimate the ECM directly from kinematic measurements of the fly, the accuracy of these estimates depend on how closely measurement errors resemble white noise (Eq. 3.11). We, therefore, determine measurement uncertainties with a more direct method to provide an alternative estimate, and confirm that white noise is an adequate model, of these errors. In particular, we model the fruit fly using the virtual fly shown in Fig. 3.8A (see also §3.5). The fly consists of two rigid wings and a body built from three ellipsoids. The sizes of each body segment is scaled to match those of real flies as estimated from the captured image sequences. By prescribing the kinematics of the virtual fly (i.e. the position and orientations each segment), we are able to generate realistic shadows of the virtual flies that estimate the types encountered in real measurements. We then apply the tracking method described in §3.4 to estimate the virtual fly's position from its shadows. By repeatedly tracking the virtual fly in a large number of orientations we are able to quantify how close the recovered positions are to the prescribed ones.

Table 3.2: Measurement uncertainties in the position and orientation of the model fly segments (right wing, left wing and body).

Segment	$\sigma_{\vec{x}}$ (pixel)	σ_{ϕ} (°)	σ_{θ} (°)	σ_{ψ} (°)
Body	±2	±2	±3	±7
Wings	±2	±5	±5	±5

We summarize the directly determined measurement variances for the kinematic variables of the fly in Tbl. 3.2 (for detailed results, see [25]). The results are similar to those shown in Tbl. 3.1. Centroid positions of the body can be recovered to better than 2 pixels, while the uncertainty in the orientation angles is ±5°. Once again, we note that the roll of the body can have large inaccuracies.

3.7 Systematic Errors in Tracked Kinematics

In §3.6.2 and §3.6.1 we characterized the random errors associated with kinematic tracking of the flight sequences. The systematic errors in the tracking of fly positions, however, remains to be addressed. It should be noted that by tracking the virtual fly in §3.6.2 both systematic and random errors may be estimated, however, the because of the relatively simpler morphology of the virtual fly when compared with a real *D. melanogaster*, we find that systematic errors are under estimated by this method. We therefore directly compare the originally measured fly silhouettes to the tracked fly poses.

For each tracked frame of a flight sequence, we map the recovered kinematics onto a virtual fly whose morphology is matched those measured from the video of the real fly. From the poses of this virtual fly we compute shadows that would be recorded by a camera, similarly to Fig. 3.8A and Fig. 3.8B. We finally overlay the shadows of the virtual fly onto the raw images of the fly to compare

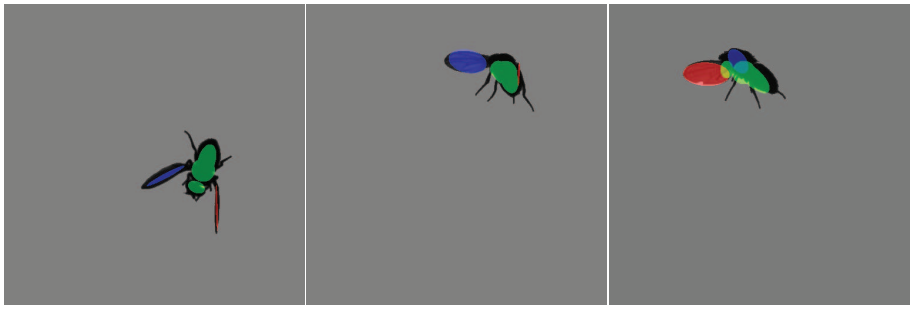

Figure 3.9: Comparison of virtual fly shadows to the corresponding measured frames of the flight sequence.

the quality of tracking. This may be done for all the frames of a flight sequence. We show the results of comparing a particular frame with the outlined method in Fig. 3.9. We find that the uncertainties in tracking the body position, orientation, and the wing orientations are in agreement with those in shown in Tbl. 3.2. We, however, find that large systematic errors appear in the centroid of the wings at the ends of strokes. These are caused by part of the wings being hidden by the body which makes detecting their centers difficult. We adjust for this systematic error in §3.7.1. We show our method for improving the detection of the body roll in §3.7.2.

3.7.1 Improving Estimates of Body Roll

Because *D. melanogaster* is roughly symmetric about the longitudinal axis of its body, the roll of the fly, ψ_b, is poorly determined the visual hull [25]. Although ψ_b plays no role in the computation of the forces on the fly, we use it to determine the orientation of the wings in the body frame (see §3.4.1). We, therefore, improve on its measurement by using observed constraints on the wing kinematics of the fly. We observe that the deviation angles of the wings, ${}^B\theta_l$ and ${}^B\theta_r$, are symmetric on average. Therefore, measurements of the lab frame angles

may be used to determine the roll angle of the body. We use Eqs. 3.8 and 3.9, to compute,

$$\begin{aligned} A &= \cos\theta_l \cos(\phi_b - \phi_l) - \cos\theta_r \cos(\phi_b - \phi_r) \\ B &= \sin\theta_l - \sin\theta_r \\ \rho &= \tan^{-1} \frac{A\sin(\theta_b - 60^\circ) - B\cos(\theta_b - 60^\circ)}{\cos\theta_l \sin(\phi_b - \phi_l) - \cos\theta_r \sin(\phi_b - \phi_r)}, \end{aligned} \tag{3.15}$$

where ρ is the roll angle that ensures ${}^B\theta_l =^B \theta_r$. Because the motion of the fly body is much slower than that of the wings, we coarse grain over the variations in ρ that come about due fast variations in $\Delta^B\theta$ using,

$$\psi_b = \int \frac{1}{\sqrt{2\pi}\mu} \mathrm{e}^{-\frac{(t-\tau)^2}{2\mu^2}} \rho(\tau) d\tau, \tag{3.16}$$

where we use the Gaussian smoothing kernel with timescale, μ, that is two wing beats wide [50]. This procedure ensures that the deviation angles of the wings are symmetric on average over the course of a few wings beats. By comparing the projected shadows of the virtual fly to images of the captured flight sequence (Fig. 3.9), we find that this method succeeds in reducing uncertainties in ψ_b to approximately $\pm 5^\circ$.

3.7.2 Improving Measurements of the Wing Centroid

As the wings of an insect beat back and forth, near stroke reversal approach each other to within less than 30°. Near these points, the body of the fly blocks part of the wings resulting in a large occlusion in the visual hull. Although the wing tips still allow the orientation of the wings at these points be reliably identified, the tracked wing centroids can have large occlusions at these points. To compensate for these errors, we use the physiology of the fly to adjust the raw

measured kinematics. Specifically, each of a fly's wings rotates about a hinge on its thorax (see [17] and also Fig. 4.3) and so constrains the wing and body kinematics. To improve measurements, we find the closest fly pose that satisfies this physiological constraint. Thus, we ensure that the reprojected (primed) coordinates of each wing are the closest to the measured coordinates (unprimed),

$$\left(\frac{x'-x}{\sigma_x}\right)^2+\left(\frac{y'-y}{\sigma_y}\right)^2+\left(\frac{z'-z}{\sigma_z}\right)^2+\left(\frac{\phi'-\phi}{\sigma_\phi}\right)^2+\left(\frac{\theta'-\theta}{\sigma_\theta}\right)^2+\left(\frac{\psi'-\psi}{\sigma_\psi}\right)^2, \tag{3.17}$$

in terms of the estimated uncertainty, σ_i, on the coordinate. We simultaneously ensure that the wing rotates about the wing hinge by enforcing,

$$\vec{x}' = \mathbf{R}(\phi', \theta', \psi')\vec{r}_c + \vec{x}_h, \tag{3.18}$$

where $\vec{x}'$ is the reprojected wing centroid, $\vec{r}_c$ is the vector in the wing frame that connects the wing hinge to the wing centroid, $\vec{x}_h$ is the position of the wing hinge in the lab frame, and $\mathbf{R}$ is the rotation matrix that connects the wing frame to the lab frame (see Eq. 3.6). We estimate $\vec{x}_h$ relative to the fly body directly from the captured flight sequence. Its lab frame position is then computed using the pose of the fly body. We verify that the kinematics are not distorted by this projection through comparison of the virtual shadows to the originally measured shadows as in Fig. 3.9.

3.8 Differentiation of Kinematic Data

Analysis of the measured kinematic data often requires, not only the measured position and orientation of the fly, but also derivatives of these measurements. For example, to model the aerodynamic forces on a flapping wing, both quasi-steady models and direct solutions of the Navier-Stokes equations require the

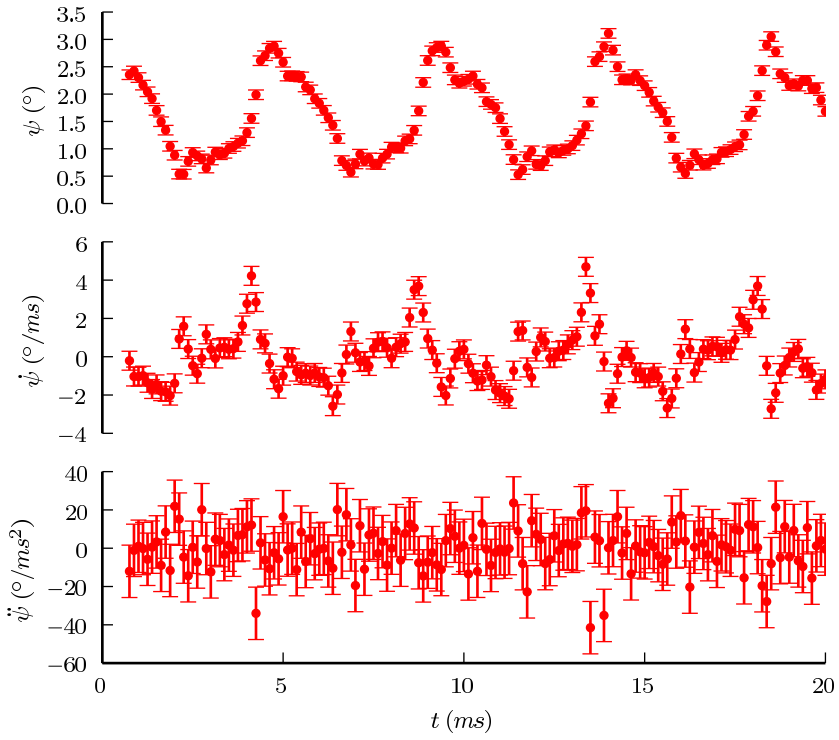

Figure 3.10: To demonstrate the amplification of measurement error by differentiation, we show the results of computing the derivatives of the wing pitch, ψ_r, for the right wing of a flight sequence using standard three point finite difference stencils.

velocity and the acceleration of the wings (see §6). Therefore, we require accurate procedures to systematically differentiate the measured flight kinematics and quantify the errors associated with this procedure.

Taking derivatives of experimental data tends to amplify measurement errors. We find that, by applying the standard central point differencing schemes to our data, that this amplification is so severe that no trends may even be observed in higher derivatives in the data. Consequently, we use smoothing procedures that are often applied to differentiate experimental data. Such smoothing procedures however, have pitfalls: they introduce an error associated with truncation of sharply changing features in the measurement data. For exam-

ple, one common method used to find the derivatives of flight sequence data is to use its Fourier series to compute higher of derivatives [31, 35, 42, 51–56]. This method, though intuitive and appropriate for certain situations, cannot be applied to the analysis of our free-flight data. The primary reason for this is that during flight maneuvers, the fly kinematics are not periodic, therefore the derivatives computed using a Fourier series are not guaranteed to converge to the true derivative [57]. In particular, this method tends to smooth out the beat-to-beat variations in kinematics that are associated with maneuvering flight.

Here, we describe the method we use to systematically differentiate the flight kinematic data. To address the problem of finding a trade off between truncation and experimental sources of error, we use a numerical technique very similar to those described in [58–62]. At its core, this technique ensures that, in smoothing the data, the truncation errors introduced remain smaller than the experimental error. In addition, this technique allows for propagating the experimental errors through the differentiation procedure so that the error in the extracted data can be determined.

3.8.1 Weight-Averaged Noisy Differentiation (WAND)

We model the measurement of a particular kinematic quantity as the sampling of a function, $f(t)$, at times, t_i. We assume that experimental measurements of flight kinematics have uncorrelated errors and that systematic errors are accounted for (see the analysis in §3.6). Therefore, we model measurement uncertainty with the addition of a zero-mean Gaussian random variable, X_i, to the

true value of the function, f_i,

$$\tilde{f}_i = f_i + X_i. \tag{3.19}$$

For our analysis, we consider functions that are sampled at regular time intervals, $t_{i+1} - t_i = h$, where the sample rate, h, corresponds to the frame-rate of the cameras.

There are two sources of error in the differentiation of f_i: the measurement uncertainty in the data itself and the procedure employed in approximating the derivative [58]. We refer to these two sources of error as random error and truncation error, respectively. Straightforward application of finite-differencing methods to the differentiation of noisy data results in minimal truncation error, but maximal amplification of the measurement noise [63]. Therefore, a smoothing procedure is employed to reduce this effect.

We introduce a weighted finite difference derivative operator,

$$D(f_i) = \sum_{j=1}^{r} w_j \frac{f_{i+j} - f_{i-j}}{2jh}, \tag{3.20}$$

where r is the averaging neighborhood and the weights, w_j, satisfy,

$$\sum_{j=1}^{r} w_j = 1 \text{ and } w_j \geq 0. \tag{3.21}$$

We find that for our data, this method is insensitive to the particular value of r as long as $r \geq 4$. We therefore use $r = 5$. The truncation error associated with D is given by the difference between the true derivative of the function, $\dot{f}_i$, and the value of the operator on noise free-data, f_i. By applying Taylor's remainder theorem, this error can be expressed in terms of the third derivative, $f^{(3)}(t^*)$, of the original function,

$$\bar{E}_i \equiv \left| \dot{f}_i - D(f_i) \right| = \frac{\left| f^{(3)}(t^*) \right| h^2}{6} \sum_{j=1}^{r} w_j j^2, \tag{3.22}$$

where $t^* \in (t_{i-r}, t_{i+r})$ and is usually unknown. Typically, this error is bounded by choosing a value for $f^{(3)}(t^*)$ that corresponds to the largest value for the physical system. Because the neurons and muscles that are ultimately responsible for this motion fire no faster than the flapping frequency [22], we use this timescale to approximate $f^{(3)}(t^*)$. The random error variance, $\bar{\sigma}_i^2$, of a time-series differentiated using Eq. 3.20 is,

$$\bar{\sigma}_i^2 = \sum_{j=1}^{r} \left(\frac{w_j}{2jh} \right)^2 \left(\sigma_{i-j}^2 + \sigma_{i+j}^2 \right), \tag{3.23}$$

where $\sigma_i = \mathrm{var}(X_i)$ is the, possibly time dependent, variance of the measurement error. For a particular set of differentiation weights, w_j, Eqs. 3.22 and 3.23 can be used to determine both the random, $\bar{\sigma}_i$, and truncation, $\bar{E}_i$, errors associated with using D.

Finding the differentiation operator D amounts to determining the weights, w_j, in Eq. 3.20. Ideally, this operator would minimize both the random error (Eq. 3.23) and the truncation error (Eq. 3.22). However, the more a function is smoothed to reduce $\bar{\sigma}_i$, the larger $\bar{E}_i$ becomes (Fig. 3.11). Consequently, these two equations cannot be simultaneously minimized [58] and a choice must be made on how large the truncation error is allowed to grow. Since $\bar{\sigma}_i$ is a property of the experimental measurement and can be characterized (see §3.6), while $\bar{E}_i$ depends on an inherent property of the true kinematics, $f(t)$, it is natural to require $\bar{E}_i \ll \bar{\sigma}_i$. Specifically, we find the w_j that minimize $\bar{\sigma}_i$ such that $\bar{E}_i$ remains smaller then the random error by some chosen factor f that is typically 50. Finally, we take as inputs the measured kinematic data $\tilde{f}_i$, the estimate on the bound for $f^{(3)}(t^*)$ and the factor f to perform the constrained convex minimization,

$$\underset{\vec{w}}{\mathrm{argmin}}\ \bar{\sigma}_i \quad \text{s.t.} \quad \bar{E}_i < f\bar{\sigma}_i, \tag{3.24}$$

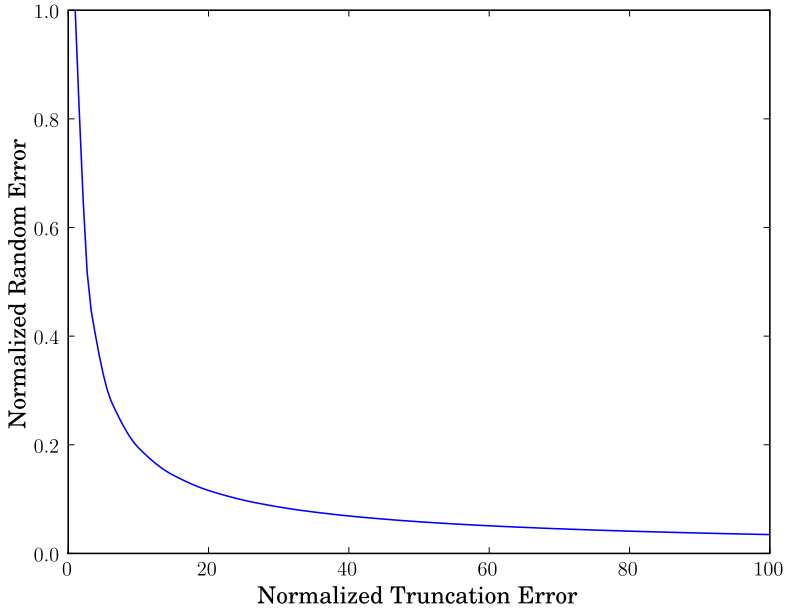

Figure 3.11: The trade-off between truncation and random errors for a function with random error whose distribution is independent of time, i.e. $\sigma_i = \sigma$. The scaled averaged random error, $\bar{\sigma}/\sigma$, and scaled truncation error, $\bar{E}/f^{(3)}(t^*)$ are shown. Each point on the curve represents the minimum random error that can be achieved for a particular value of the truncation error. The range of the truncation error is determined by the discretization, h, and the averaging neighborhood, r.

using standard quadratic programming packages (e.g. MATLAB or cvxopt). The resulting values for w_j define the optimal derivative D that ensures $\bar{E}_i$ is a factor f smaller than $\bar{\sigma}_i$. Throughout this work, we use this method to differentiate the measured flight kinematics. To determine second derivatives, we use an analogous method, but with Eq. 3.20 modified to compute the second derivative. We show the results of applying WAND to the same time-series as Fig. 3.10 in Fig. 3.12.

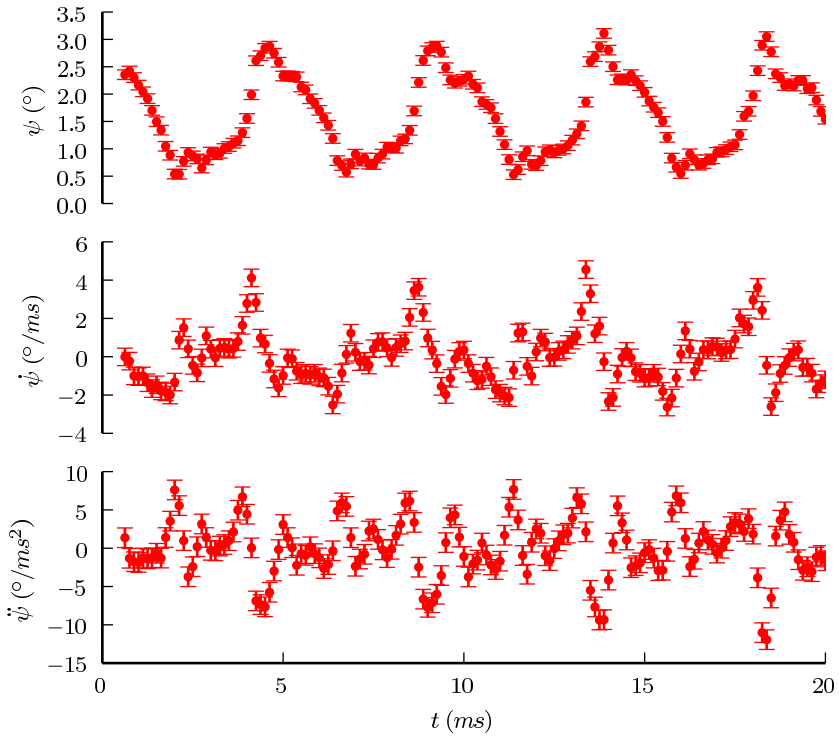

Figure 3.12: To demonstrate the success of weight averaged differentiation techniques in reducing the random error variance of differentiated time-series, we show the results of computing the derivatives of the wing pitch, ψ_r, for the right wing of a flight sequence using WAND.

3.8.2 Kernel Based Time-series Interpolation

We use a Kernel based nonparametric regression method to interpolate the measured fly kinematics [50, 59]. For the time-series, t_i, of a particular kinematic variable, e.g. the wing amplitude ϕ_i, we use

$$\Phi(t) = \frac{\int_{t_1}^{t_2} K(t,\tau)\phi(\tau)d\tau}{N(t)}, \tag{3.25}$$

where $\Phi(t)$ is the interpolated function measured from t_1 to t_2, $K(t,\tau)$ is a regression kernel, and the normalization,

$$N(t) = \int_{t_1}^{t_2} K(t,\tau)d\tau. \tag{3.26}$$

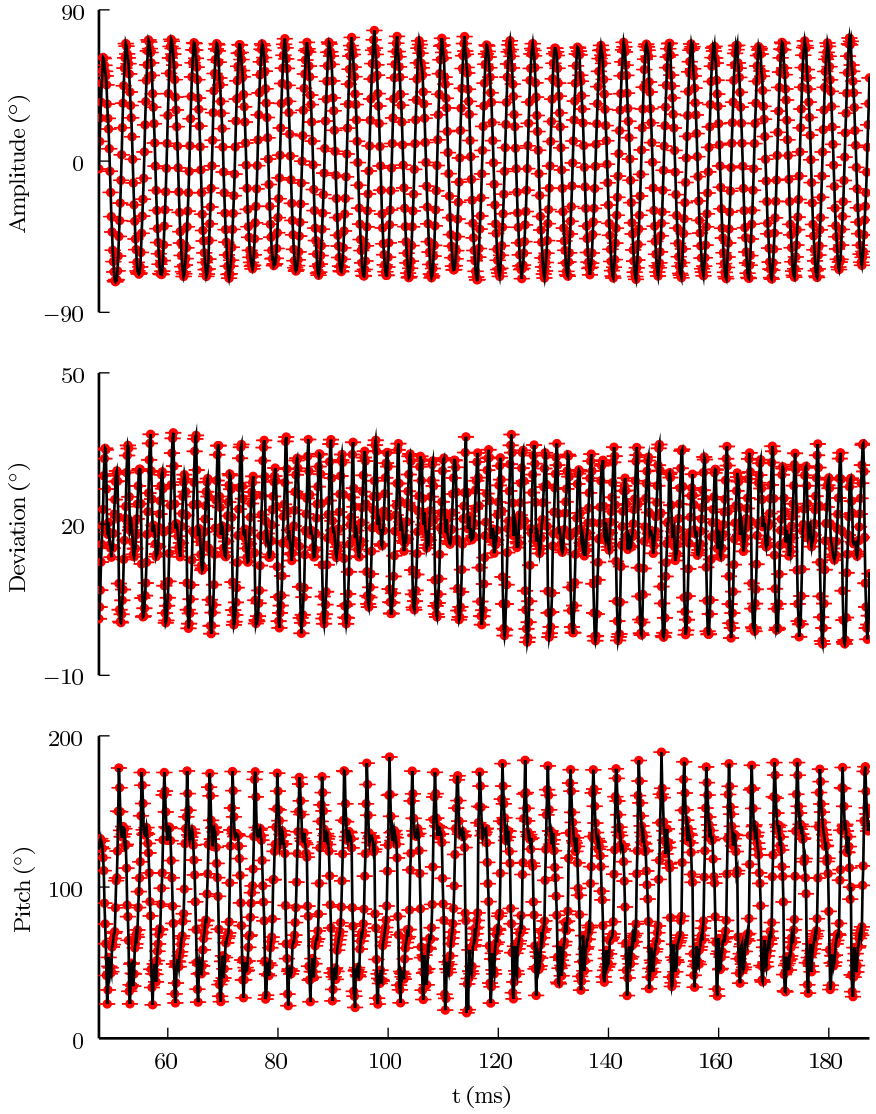

Figure 3.13: Orientation angles of the right wing of a fly from a 33 stroke flight sequence. The red dots correspond to measured frames, with error bars as shown. To interpolate these time-series with the black lines we use a nonparametric kernel based regression method.

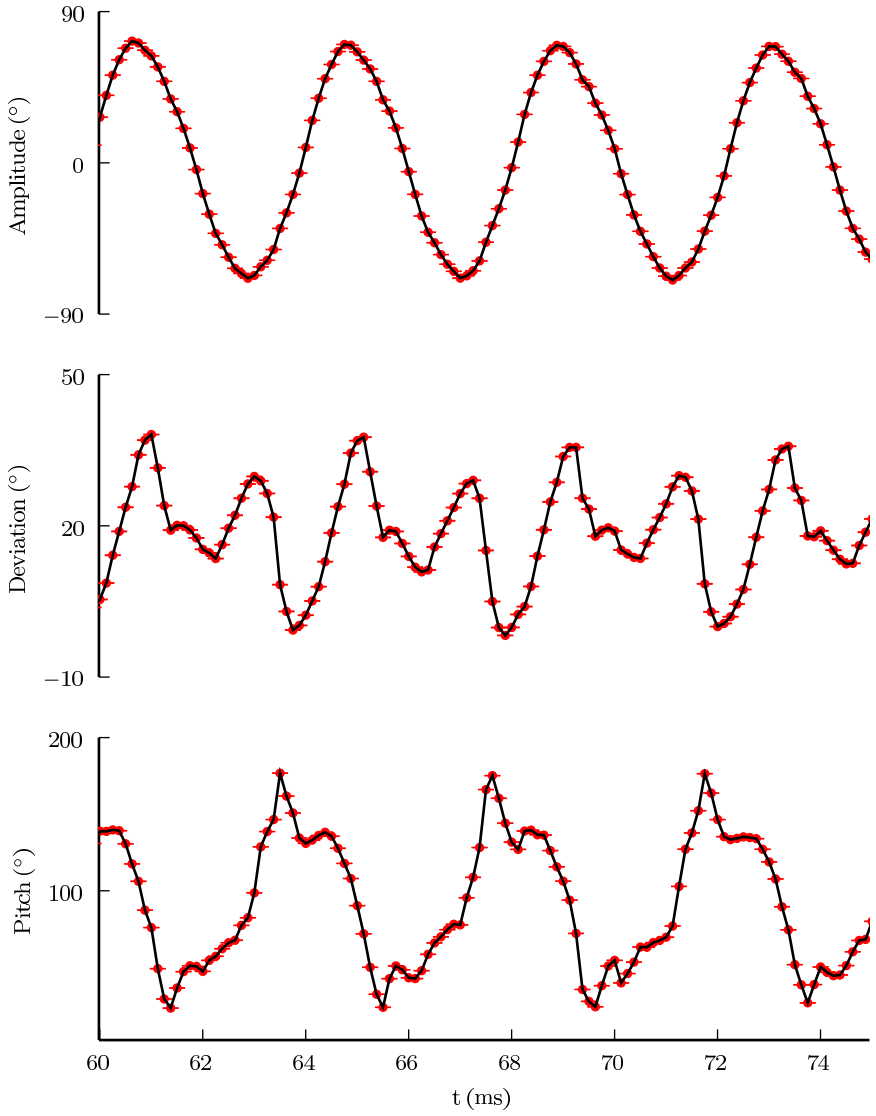

Figure 3.14: Orientation angles of the right wing of a fly from a 33 stroke flight sequence. The red dots correspond to measured frames, with error bars as shown. To interpolate these time-series with the black lines we use a nonparametric kernel based regression method. We show a zoomed in view of the 33 strokes in Fig. 3.13 to focus on only 3 wing beats and highlight interpolation.

The integrals in Eqs. 3.25 and 3.26 are evaluated numerically, e.g. using,

$$\begin{aligned} \Phi(t) &= \frac{\sum_{i=1}^{N} K(t,\tau_i)\phi(\tau_i)\Delta t}{N(t)} \\ N(t) &= \sum_{i=1}^{N} K(t,\tau_i)\Delta t. \end{aligned} \tag{3.27}$$

We use a Gaussian regression kernel,

$$K(t,\tau) = e^{-\left(\frac{t-\tau}{\sigma}\right)^2}, \tag{3.28}$$

where the bandwidth, σ, is chosen heuristically so that the peaks of the time-series are properly interpolated [59]. In Figs. 3.13 and 3.14, we show the results of interpolating the right wing orientation angles of a 33 stroke flight sequence. The measured orientation parameters are shown using the red circles with error bars and the interpolating function is shown in black.

To interpolate a function that is constrained to be periodic with period T, we modify the regression kernel,

$$D(t) = 1 - \cos\left(\frac{2\pi t}{T}\right) \tag{3.29}$$

$$K(t,\tau) = e^{-\left(\frac{D(t-\tau)}{\sigma}\right)^2}, \tag{3.30}$$

where Eq. 3.29 is derived from the chord-length between between two angles on a circle. In Fig. 3.15 we show the results of interpolating a time-series constrained to be periodic. The red circles with error bars correspond to the measured orientation parameters and the solid black line is the result of interpolation.

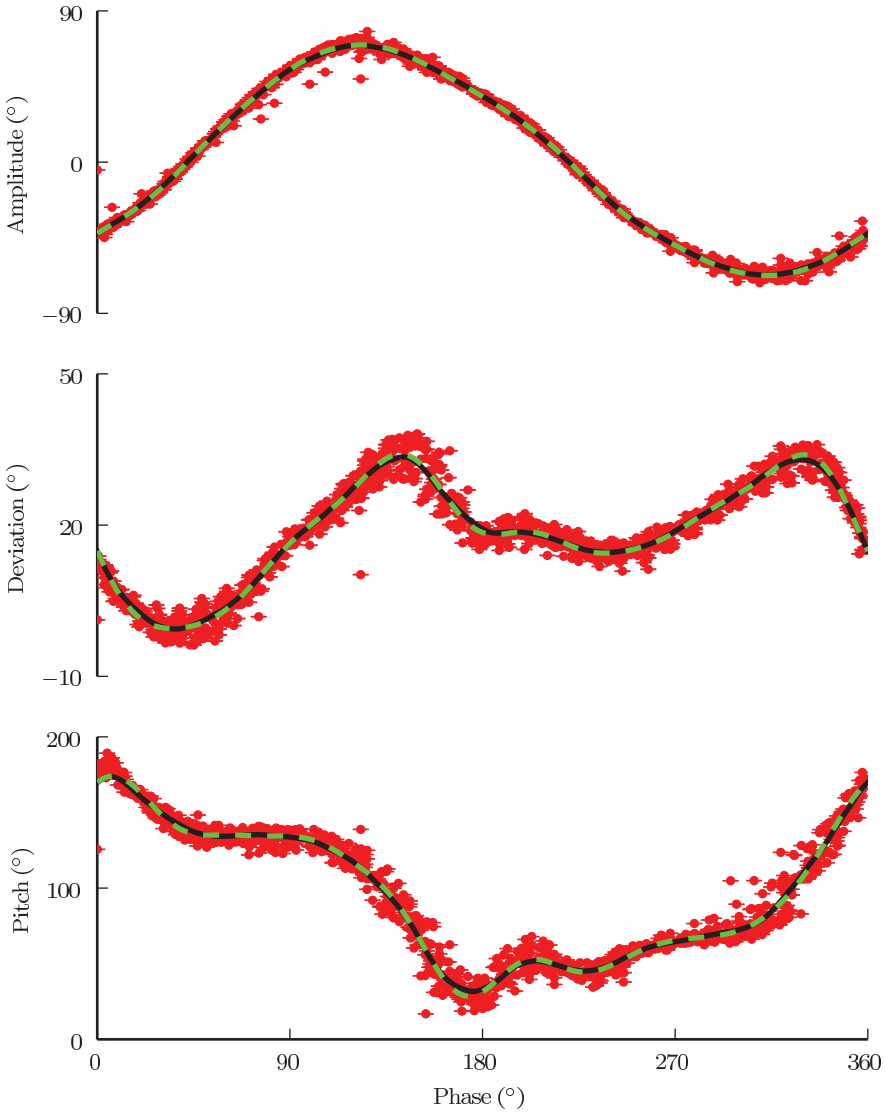

Figure 3.15: Phase reconstruction of the right wing orientation angles from a 33 stroke hovering sequence. The phase variable continuously winds around a circle at a constant rate. We show the result of plotting the phase angle mod 2π versus the wing angles. To find the "typical" phase averaged stroke, we use either a Fourier series (dashed lines) or a periodic Kernel based interpolation (solid line).

3.9 Phase Reconstruction of Flight Kinematics

Insects induce flight maneuvers by subtly altering the cyclical flapping motion of their wings [21]. To visualize these changes, we often find it useful to compare the "average" or "typical" wing-beats during steady flight and while the insect is performing the maneuver. Such comparisons help to surmise the changes in wing kinematics that an insect may use to control such a maneuver. To perform these comparisons, we find the average amplitude, deviation and pitch stroke of the wings. For a perfectly periodic noise-free time-series, strokes could be compared on a wing-beat to wing-beat basis, however, insect wing beats have inherent stochasticity due to both measurement and the underlying biology. Therefore, to make such a comparison, we first reconstruct the phase of the flight sequence using the method described in [64].

A periodic time-series can described by an angular variable, λ, which describes its position along a circle, e.g. for a perfectly periodic time-series, t_i, with frequency, f, the phase is $\lambda_i = 2\pi f t_i$ [64]. We estimate λ from the orientation angles of the insect wings as it winds around the circle. In Fig. 3.15 we show the results of reconstructing the phase of the 33 wing beat flight sequence shown in Fig. 3.13. Plotting the wing orientation angles versus the $\lambda \mod 2\pi$, obviates the periodicity of insect strokes and the wing beat to wing beat variations in the stroke. To reconstruct the average stroke from the red circles in Fig. 3.15, we either use the periodic kernel interpolation method described in §3.8.2 (shown using the solid black line in Fig. 3.15) or recover the phase space Fourier coefficients [65–68] (shown using the dashed blue line in Fig. 3.15). Both methods produce nearly identical results.

3.10 Summary and Conclusions

In this chapter, we described a method to measure, visualize and analyze the wing and body kinematics of freely-flying fruit flies. This method was developed in conjunction with Leif Ristroph and Gordon Berman.

We demonstrate that using this method, we are able to accurately determine the twelve degrees of freedom that describe a fruit flies orientation. These degrees correspond to the 6 degrees of freedom that describe the position and orientation of the flies body, and the 3 degrees of freedom that describe the orientation of each wing to the body. After correcting for systematic errors, we are able to discern angular positions to within a few degrees and positions to within a few voxels. With the hundreds of wing beats of maneuvering and freely flying insects this method enables us to capture we are able to probe the mechanisms that insects use to control their flight in a level of detail never before seen.

CHAPTER 4

THE DYNAMICS OF WING PITCHING IN *DROSOPHILA* FLIGHT

4.1 Introduction

Insects can fly because of the forces generated by their rapidly flapping wings. The wing motions themselves, however, result from a complex coupling of muscular, aerodynamic, inertial, and passive mechanical forces. Because of this complexity, how wing dynamics arise from these coupled forces remains an active area of research [22]. Here, we focus on determining how insects effect the orientation of their wings as they slice through the air. This motion, called the wing pitch, is important in the aerodynamics of both fixed and flapping wings alike [69,70]. In insect flight, research suggests that, for steady flight wing pitching may require no direct muscular actuation [18,29,53,71]. We, therefore, probe the passive mechanical forces that drive this motion.

To determine how insects induce wing pitching, we analyze free flight kinematics of *Drosophila melanogaster*, and infer the torques that these insects the exert to drive their wings. We use the apparatus and techniques described in [25] and §3 to measure the wing and body kinematics of the fruit flies. This method captures videos at 8000 frames per second allowing us to image approximately 35 frames for each wing beat of *D. melanogaster* which typically have wing beat frequencies of 200–250 Hz. In Fig. 4.1, we show the wing and body kinematics of a fruit fly during a 140 ms, 33 wing beat, flight sequence. In this sequence, the insect flies 0.75 cm forward, while ascending 0.5 cm. The orientation of the body pitch and roll remain steady at 55° and 0°, respectively. The yaw motion exhibits slight wiggles of less than 10°. At the same time, the wings of the fly are

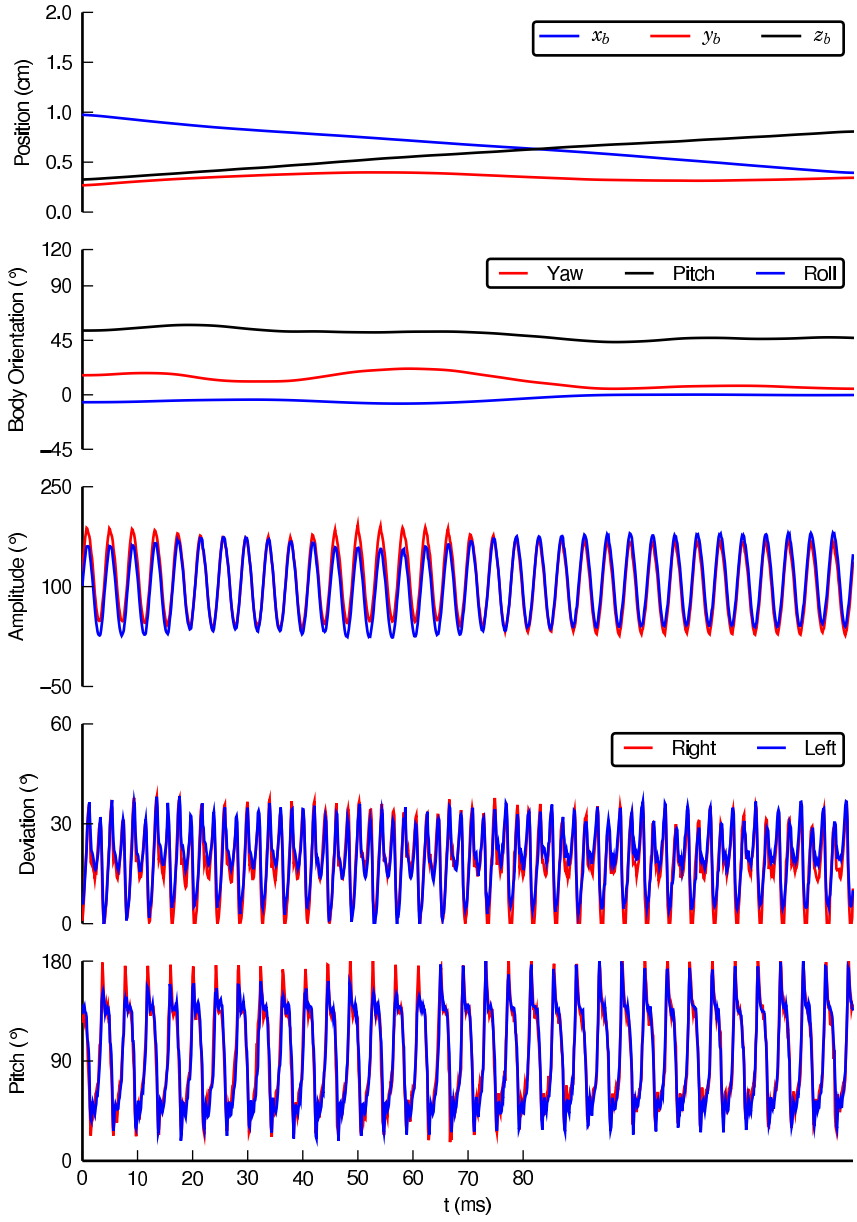

Figure 4.1: We show the wing and body kinematics of a freely flying fruit fly. In 140 ms, 33 wing beats, the insect flies 0.75 cm forward, while ascending 0.5 cm. The body pitch remains steady at 55°, the roll is approximately 0°. There are slight $\leq 10°$ wiggles in the yaw motion of the insect. Only slight asymmetries are visible between the left and right wings of the fruit fly.

close to left-right symmetric as they flap back and forth in a figure-eight motion. Although the following analysis is shown for this 33 wing beat flight sequence, we find analogous results for 16 additional flight sequences from distinct flies.

The remainder of this chapter is organized as follows: in §4.2 we determine the driving torques exerted by the fruit flies to move their wings. We confirm previous results to determine that insects do positive work to pitch their wings. We, however, find in §4.3 that the insects exert a restoring torque that is very important in determining the dynamics of the wings. We find that this torque is consistent with a spring dash-pot restoring torque that may result from elastic deformation of the wing material. In §4.4, we show this restoring force, when coupled to aerodynamic, inertial and driving forces can account for the pitching motion of insect wings. Finally, in §4.5, we summarize the spring and damping constants found for all 17 flight sequences.

4.2 Pitching Torque and Rotational Power

Insects rotate their wings about hinges on either side of their thorax (Fig. 4.2). This hinge is one of the most intricate joints found in nature: it transfers muscle forces to the insect wings and through its biomechanical properties allows wings to oscillate back and forth [16, 72]. Because flight muscles do not extend into the largely rigid wings of *Drosophila*, the muscular and passive mechanical forces exerted by the insect act like a point torque at this joint. Because the wings are attached to the hinges near their leading edge, the center of mass of the wing is behind the driving torque. Therefore, any actuation of the wing, results in a moment that will cause wing pitching [19, 28].

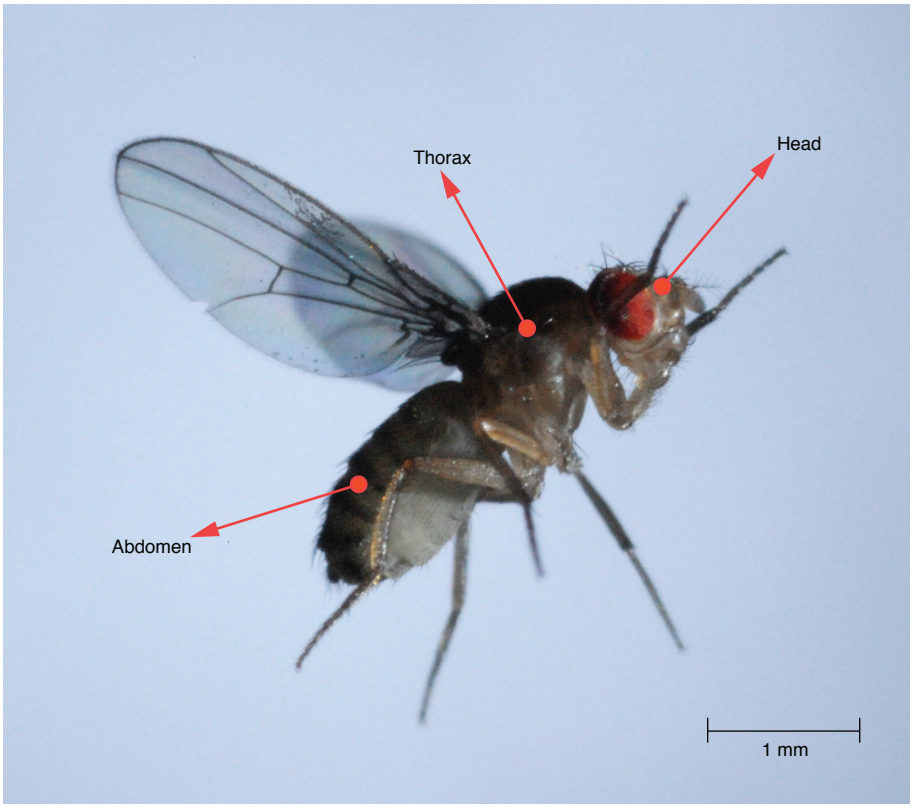

Figure 4.2: We analyze the wing dynamics of freely flying *D. melanogaster*. These insects are approximately 2 mm long and, like all insects, have a segmented body, consisting of a head, thorax and abdomen. The flight muscles of *Drosophila* are all located within the thorax and do not extend into the wing. *Image courtesy of Leif Ristroph*

When viewed in isolation, each wing of the fruit fly has two sets of external forces and torques on it: aerodynamic forces, $\vec{F}_a$ and τ_a, and driving forces and torques exerted by the insect, $\vec{F}_i$ and $\vec{\tau}_i$. These combine to determine the motion of the fly wing,

$$\begin{aligned} m_w \vec{a} &= \vec{F}_a + \vec{F}_i \\ \mathbf{I}\dot{\vec{\omega}} &= \vec{\tau}_a + \vec{r}_c \times \vec{F}_a + \vec{\tau}_i + \vec{r}_h \times \vec{F}_i. \end{aligned} \tag{4.1}$$

where m_w and $\mathbf{I}$ are the wing mass and moment of inertia, $\vec{a}$ and $\dot{\vec{\omega}}$ are the translational and angular acceleration of the wing center of mass. In Fig. 4.3 we show final two terms in Eq. 4.1: the wing center of mass to centroid vector, $\vec{r}_c$, and the

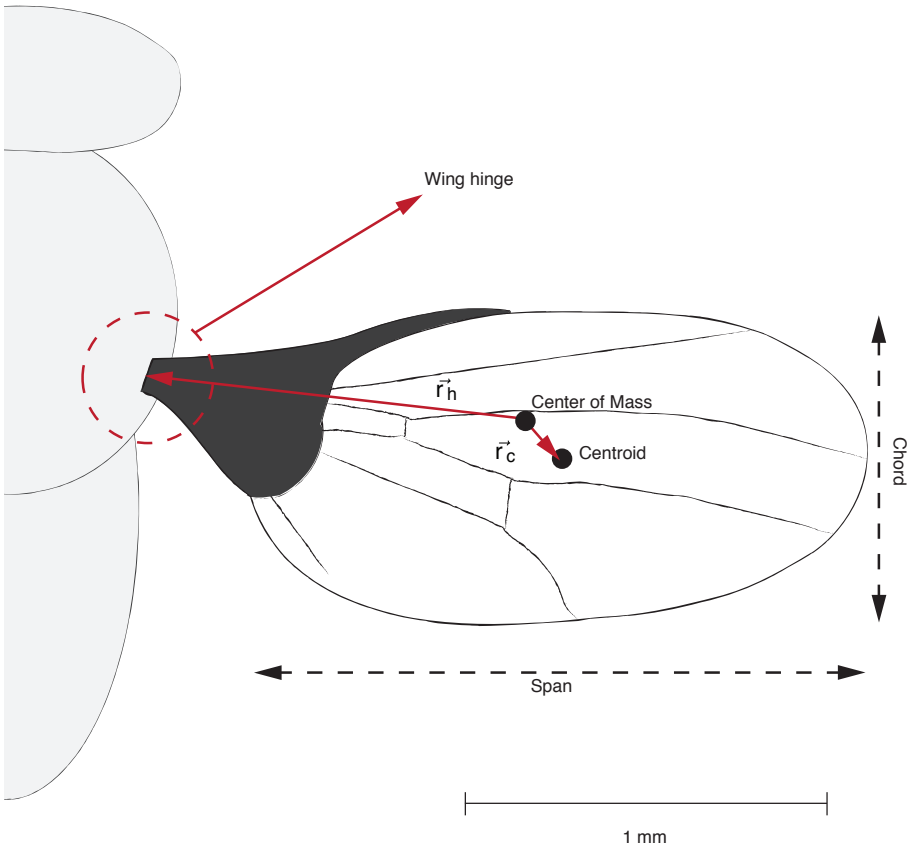

Figure 4.3: Top view of a fruit fly wing. *Drosophila* rotate their wings about a hinge attached to the thorax. The driving forces and passive mechanical elements in the wing act like a point torque at the wing hinge. Also labeled in the figure are the wing centroid, center of mass, span, and chord. The vectors $\vec{r}_c$ and $\vec{r}_h$ that, respectively, connect the wing center of mass with the centroid and wing hinge.

center of mass to wing hinge vector, $\vec{r}_h$. Because the both passive mechanical forces and muscle forces act like a point torque at the wing hinge, the force, $\vec{F}_i$ is just a constraining force that keeps the wing attached to the body. All muscle and passive mechanical actuation is encompassed in $\vec{\tau}_i$. This can be determined by inverting Eq. 4.1,

$$\vec{\tau}_i = \mathbf{I}_{cm} \cdot \dot{\vec{\omega}} - \vec{r}_h \times m_w \vec{a}_{cm} + (\vec{r}_h - \vec{r}_c) \times \vec{F}_a - \vec{\tau}_a. \tag{4.2}$$

To determine τ_i we measure m_w, $\vec{a}$ and $\dot{\vec{\omega}}$ and estimate $\mathbf{I}$, $\vec{r}_c$, and $\vec{r}_h$ by modeling the fruit fly wing as an elliptical disc with mass distribution approximated from

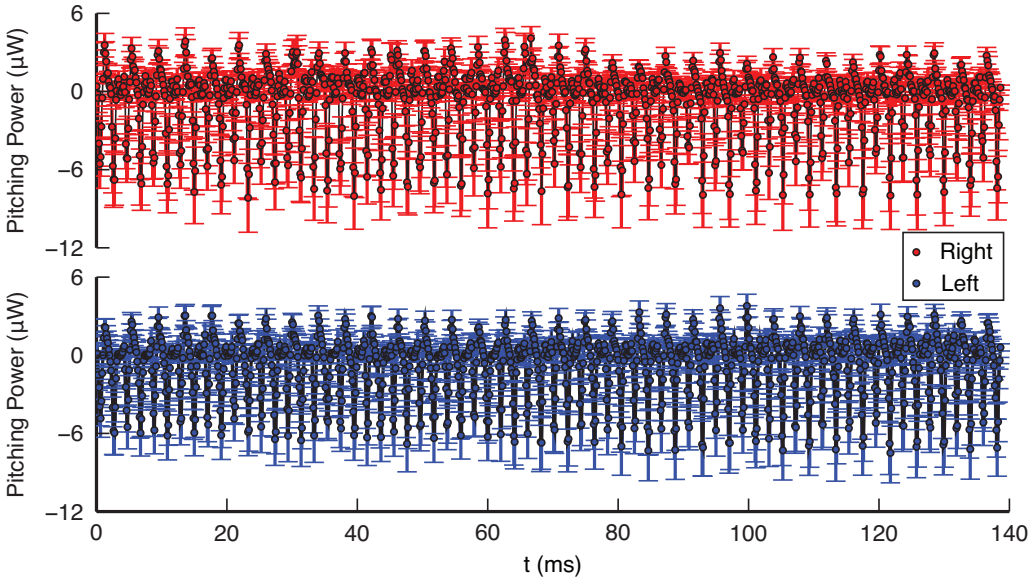

Figure 4.4: The mechanical power involved in pitching the insect wings, the rotational power P_{rot}, computed for the 33 wing beat flight sequence show in Fig. 4.1. Throughout the flight sequence, large negative peaks coincide with reversal of the wing pitch with much reduced positive peaks immediately after. The right wing is shown in red, and the left wing is shown in blue. Error bars are propagated from measurement errors on the wing kinematics.

[29]. We, then simulate $\vec{F}_a$ and $\vec{\tau}_a$ from the measured wing kinematics using the flapping wing model (see §6.3.2). The span-wise component of this torque, τ_p, is the torque exerted by the fly to pitch its wings.

To test whether flight muscles must exert active work to pitch the wings, we compute the mechanical power exerted by the insect to rotate its wings about the span. From Eq. 4.2 this is,

$$P_{rot} = \tau_p \omega_p, \tag{4.3}$$

where ω_p is the angular velocity of the wing about its span-wise axis. In Fig. 4.4 we show rotational power as a function of time for the 33 stroke sequence. Throughout the flight sequence, large negative peaks appear twice every wing beat followed by very small positive peaks. The large negative peaks coincide with wing pitch reversal and, in agreement with [53] and §2, indicate that the

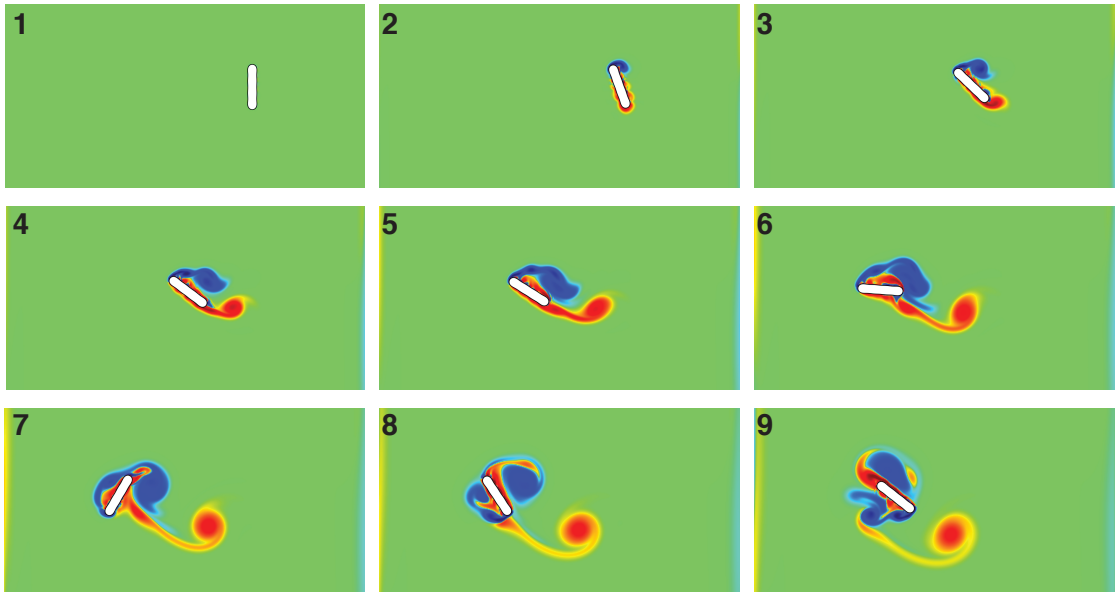

Figure 4.5: A wing that flaps back and forth with no torque constraining its pitch is very unstable. In the above example, the wing tumbles around point of rotation, the torsion axis.

insect need not exert energy to pitch its wings. This finding suggests that, for steady flight, direct muscular actuation may not used to pitch insect wings. This is in supported by measurements on tethered insects which indicate that flight muscles do not fire during wing pitch reversal [18].

4.3 Passive Mechanical Torques on Wing

We use a two-dimensional simulated flapping wing to test whether, as suggested in [73], wing pitching is fully explained by aerodynamic forces and wing inertia coupling to driving forces that are offset from the wing center of mass. We simulate the passively pitching flapping wing using methods in §6.2.1 and §6.2.2. In Fig. 4.5 we show the results of simulating a wing that is driven back and forth at its leading edge, and is allowed to freely rotate about the driving

point, termed the torsion axis. We find that the wing immediately tumbles at the end of this motion. Through many trials, we find that with no pitching torque, τ_p, the wing pitch is extremely unstable. Such a wing cannot produce sufficient lift for insects to sustain flight. Thus, we find that, although the insect does not exert any mechanical energy to for wing pitching, τ_p is pivotal in determining the dynamics of wing pitching.

Studies on tethered and dead flies suggest that τ_p may, in part, be caused by elastic deformations of the wing and wing hinge [18,73]. To test this hypothesis directly from the free flight measurements of *Drosophila*, in Fig. 4.6 we plot τ_p versus the wing pitch angle, ψ for the 33 wing beat flight sequence. Each measured frame of the fruit fly is summarized by one filled circle, where red circles are measurements of the right wing and blue circles are for the left wing. Each wing traces out an approximately elliptical trajectory in the $\psi - \tau_p$ plane for each wing beat. The direction of propagation around the curve is consistent with the fact that energy is dissipated by wing pitching Fig. 2.5. The negative correlation between ψ and τ_p indicates that τ_p acts like a restoring torque when the wing pitch deviates from the ellipse center. This is consistent with the behavior expected if τ_p is caused by viscoelastic material deformations. The restoring torque, τ_p^*, of such a material is described by the Kelvin-Voigt model [74],

$$\tau_p^* = -\kappa\,(\psi - \psi_0) - C\dot{\psi}, \tag{4.4}$$

where κ is the torsional constant of the attached biological material, C is viscous dissipation in the material, and ψ_0 is the equilibrium orientation of the material. Visually, in Fig. 4.6, κ is determined by the slope of the major axes of the ellipse, C is determined by the length of the minor axis of the ellipse, and ψ_0 is determined by the center of the ellipse.

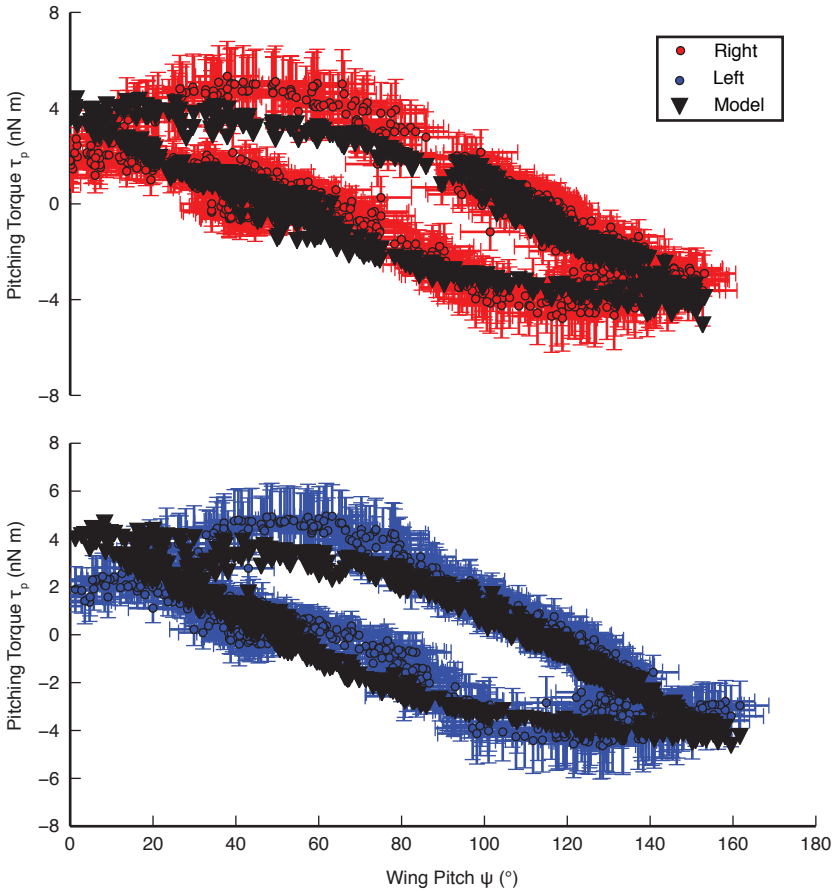

Figure 4.6: We show the dependence of the pitching torque, τ_p, on the wing pitch. Each filled circle corresponds to a captured frame from the 33 stroke flight sequence in Fig. 4.1. The right wing is shown in red and the left wing is shown in blue. Error bars are propagated from measurement errors. Each wing traces out an approximately elliptical trajectory in the $\psi - \tau_p$ plane for each wing-beat. The black triangles are computed from a spring dash-pot model that only depends on ψ and $\dot{\psi}$. The model parameters - torsion constant, κ, damping constant, C, and rest angle, ψ_0 - are fit to the entire time-series for τ_p.

Table 4.1: We summarize the extracted spring model parameters for the 33 wing beat flight sequence shown in Fig. 4.1. This model with the parameters shown below explain over 85% of the variance in the extracted pitching torque.

Parameter	left wing	right wing
κ $(pN\ m/^\circ)$	40.±7	41±7
C $(fN\ m\ s/^\circ)$	21±10.	24±10.
ψ_0 $(^\circ)$	76±1	79±1

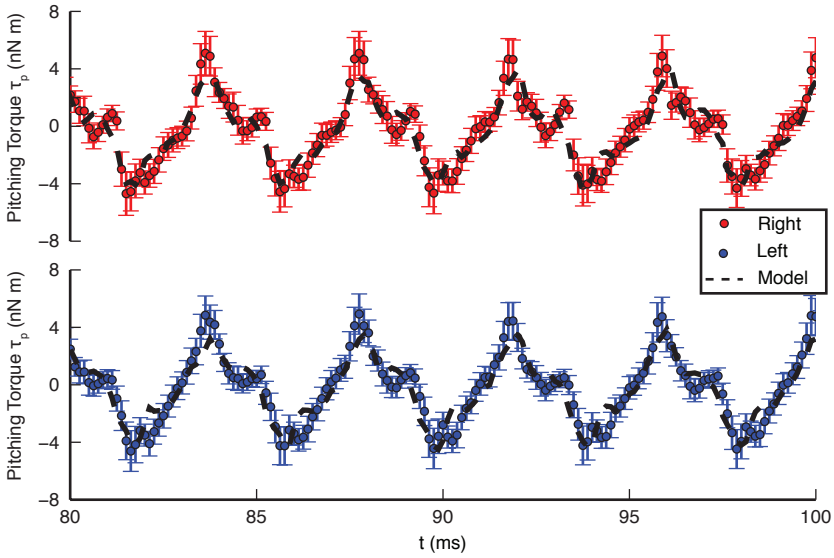

Figure 4.7: We infer the torque exerted by the insect to pitch its wings, τ_p, from experimentally measured kinematics and morphology. Filled circles correspond to the instantaneous torques determined for each from of the flight sequence. Error bars are propagated from experimental measurements. The right wing is shown in red, while the left wing is in blue. The dashed lines are computed from the spring dash-pot model for τ_p with parameter values extracted from the whole flight sequence. We show a representative range, 80–100 ms, of τ_p to highlight details.

To determine the gross viscoelastic properties that can lead to a restoring torque analogous to τ_p, we use the Levenberg-Marquard algorithm (LMA) to determine the κ, C, and ψ_0 that minimize the squared error between τ_p and τ_p^* (Eq. 4.4) for each wing of the fruit fly [75]. These parameters, along with propagated error bars are shown in Tbl. 4.1. In Fig. 4.7 we overlay the predictions of Eq. 4.4 using the parameters from Tbl. 4.1 (dashed black line) on a representative range of τ_p as a function of time. The red and blue circles correspond to τ_p determined from Eq. 4.2 for each measured frame of the left (blue) and right (red) wings. We find that the spring dash-pot model for this torque explains over 85% of the observed variance in τ_p. In fact, the model prediction largely lies within the uncertainty measurements of τ. To further highlight the corre-

spondence of the model to the experimentally determined pitching torque, we show model predictions with the black triangles in Fig. 4.6. The elliptical shape of the trajectory in the $\psi - \tau_p$ plane is recovered by this model.

4.4 Torsional Spring Explains Wing Pitching

Although we find that τ_p can be modeled by Eq. 4.4, ultimately, the test of this model is whether it agrees with the measured time-series for wing pitch. To test whether the pitching torque modeled by a spring dash-pot model is sufficient to explain the observed wing pitching, we simulate the dynamics of a passively pitching wing. We prescribe the torsion axis amplitude and deviation angles as measured experimentally (Fig. 4.1) and allow the wing to pitch passively in response to inertial, aerodynamic and torsional spring forces and torques (e.g. Eq. 6.21). In Fig. 4.8A we compare experimental measurements of the wing pitch (filled circles with error bars) to computer simulations of the passively pitching wings (black dashed line). The morphology of the simulated wing is matched to measurements of the actual fly's wings, and we use the torsion spring parameters shown in Tbl. 4.1. Currently, the aerodynamic forces on the wing are simulated using the flapping wing quasi-steady model. We find that the wing pitch is in quantitative agreement with experimental measurements. The overall characteristics of the wing pitch angles for both wings are recovered as is the peak to peak amplitude. We note that there is a very slight phase lag of the numerical simulations with respect to experimental measurements. Furthermore, the bump that exists in the wing pitch angle near 83 ms (and repeats periodically), is also not fully recovered. We believe that these effects may be explained through full unsteady simulations of the wing pitch.

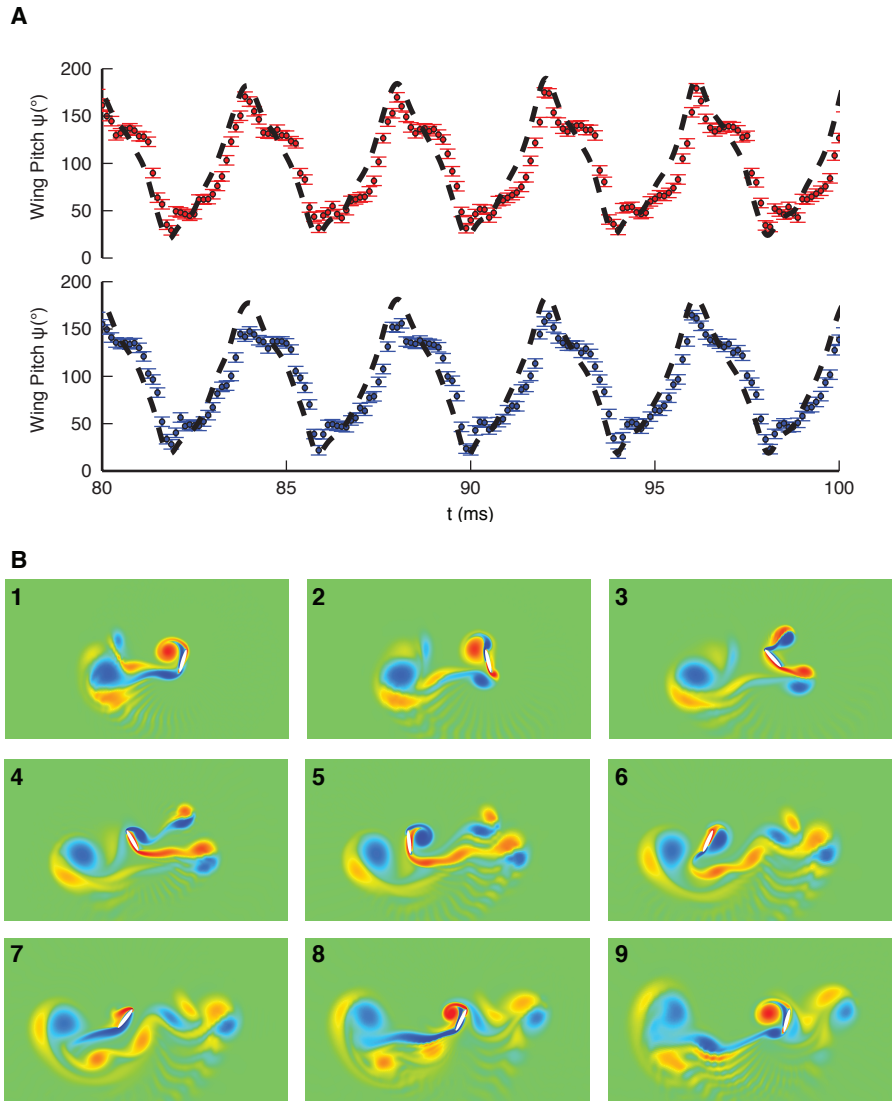

Figure 4.8: (**A**) We use the falling paper model to simulate a passively pitching wing that is driven at its torsion axis. The filled circles are measured values of ψ for the right (red) and left wings (blue). The error bars are the estimated experimental uncertainty. The dashed lines on the figure are the results of simulating the wing constrained to move as the measured kinematics in the amplitude and deviation direction, while pitch is determined by the inertial and aerodynamic torques and the pitching torque on it. (**B**) Preliminary simulations of a passively pitching wing with CFD simulations. The behavior of this wing is qualitatively very similar to the quasi-steady model.

Preliminary results of simulating a passively pitching with a spring dash-pot restoring torque and aerodynamic forces simulated using the two-dimensional Navier-Stokes equations are shown in Fig. 4.8B. The numerical simulations depict a wing whose morphology is matched to the experimental wing parameters being sinusoidally oscillated at the torsion axis using the method described in §6.2.2. We find that when a torsional spring with the parameters in Tbl. 4.1 constrains the passive wing pitch the wing no longer tumbles as in Fig. 4.5. Furthermore, we find that the wing pitch becomes periodic with a positive approximately 45° angle of attack on both the forward and reverse strokes qualitatively matching numerical simulations of the quasi-steady model. Our preliminary results also indicate that simulations in the unsteady fluid slightly advance the phase of the wing pitch relative to quasi-steady simulations. We also notice that a slight bump can be seen in the unsteady simulations when the wing rides over its leading edge vortex as in frame 2 of Fig. 4.8.

4.5 Summary

To ascertain the generality of these results, we repeat the preceding analysis on the additional 16 flight sequences. We find similar qualitative features in the $\psi - \tau$ figure, and find that the spring dash-pot model captures these structures equally well for these flight sequences. We summarize the distribution of κ and C in Fig. 4.9A and B, respectively. We find that, for the 17 total flight sequences, the mean value $\kappa = 53\ pN\ m/^\circ$, while the standard deviation is 20. $pN\ m/^\circ$. This latter value, when compared with the average uncertainty in $\sigma_\kappa = 13\ pN\ m/^\circ$ indicates that, within the resolution of our experiment, κ does not vary significantly. To test the sensitivity of the wing pitch to variations in κ we simulate the

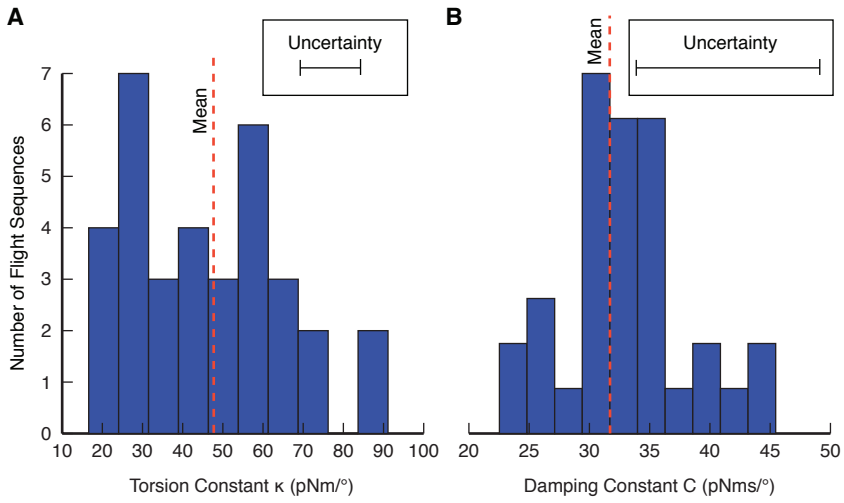

Figure 4.9: The distribution of torsion, κ, and damping, C, constants determined from 17 distinct flight sequences totaling 7129 frames and over 200 wing beats. Each flight sequence is considered two separate data-points, one for each wing of the fly. (**A**) The distribution of the torsion constant, κ. The mean κ is 53 $pN\,m/^\circ$ with average uncertainty on each value of 13 $pN\,m/^\circ$, and standard deviation of 20. $pN\,m/^\circ$ for the distribution. (**B**) The distribution of the damping constant, C. The mean C is 22 $pN\,m/^\circ$ with average uncertainty on each value of 12 $fN\,m\,s/^\circ$, and standard deviation of 5 $fN\,m\,s/^\circ$ for the distribution.

wing kinematics with varying values of κ. Quasi-steady results indicate that the value of κ has only a very slight effect on the kinematics and manifests itself as a variation in the phase of ψ relative to the stroke amplitude. Because errors in the wing mass and moment of inertia wing have a similar effect on the phase, uncertainties in these parameters do not currently enable us to conclusively state whether κ changes. Preliminary findings, however, reveal that because of the very subtle effect that κ has on the kinematics we are able to ignore changes to this parameter with negligible effects on aerodynamic forces. Furthermore, we find that these torsion constants agree with scaled estimates for the torsion constants taken from measurements on the wings of house flies [73].

We find that the distribution of the damping constant, C, has an average value of $C = 22\ pN\,m/^\circ$ and standard deviation 5 $fN\,m\,s/^\circ$. We also find that the

average measurement uncertainty on each value is $\sigma_C = 12\ fN\ m\ s/^\circ$. Therefore, within the resolution of our experiment C does not vary from flight sequence to flight sequence. For the torsion spring rest angle, ψ_0, we do not show the distribution. We, however, find that the average $\psi_0 = 90^\circ$, and the standard deviation is 10°. When compared to the average uncertainty on this parameter, $\sigma_{\psi_0} = 1^\circ$, we find that significant variations exist in this kinematic parameter between flight sequences. In fact, as we discuss in §5, we find that this parameter can vary within a flight sequence as well, and may be used by the insect to control its flight. We suspect that ψ_0 captures the effective action of flight muscles that can change the orientation of the wing hinge [16].

CHAPTER 5

DROSOPHILA MODULATE PASSIVE WING PITCHING TO INDUCE IN-FLIGHT TURNS

5.1 Introduction

To fly, insects must constantly flap their wings at frequencies that often exceed several hundred beats per second. Yet, subtle changes in wing motion can dramatically affect the resulting aerodynamic forces. Given these constraints, how do insects control their wings to produce such wonderfully complex flight maneuvers? At the root of this question lies one of the longest standing problems in insect flight: what aspects of their wing motions do insects actuate directly, and what aspects are the result of passive aerodynamic mechanisms like the ones that make a flag wave in the wind [1, 2]. Despite numerous studies focused on aerodynamic forces generated by flapping wing motions [5, 14, 76, 77], this fundamental question remains unresolved.

To determine which aspects of the wing motion are actuated by the insect to induce a turn, we combine novel experimental techniques with simulation and simple mathematical models to back out forces and torques that drive the wings. Our experiment consists of using three orthogonally positioned high speed video cameras to film *D. melanogaster* in free flight (see §3.2). The videos are captured at 8000 frames per second allowing us to image 35 frames for each wing beat. Using state of the art motion tracking techniques [25], we extract the wing and body kinematics for movies where the insects are turning by predominantly changing their yaw orientation. Such turns, while common, can exceed speeds of 1500 °/s [78, 79]. These extreme flight maneuvers tend to exagger-

ate the underlying control mechanisms and are therefore attractive for probing questions relating to wing actuation.

5.2 Asymmetries in Wing Pitch Cause Turn

We visualize the wing and body kinematics of a fruit fly performing a saccade in Fig. 5.1. The phases of motion are shown by overlaying six snapshots of the recorded images along with the reconstructed model of the fly. Our motion tracking method fully recovers the six degrees of freedom describing the position and orientation of the insect body. In addition, since the wings of the fruit flies are relatively rigid and rotate about a hinge [80], this method recovers three Euler angles - amplitude, ϕ, deviation, θ, and pitch, ψ - that define each wing's orientation relative to the fly body (see Fig. 3.5). During this sequence, the fly performs a 120° clock-wise turn in 80 ms, or 18 wing beats, while its center of mass moves approximately 16 mm. In addition, the insect remains level so that the turn consists mainly of changing the yaw direction of the insect, ϕ_b. Similar features are characteristic of all ten movies used in our analysis.

During each beat, the wings trace out a cyclical figure eight path through the air. A span-wise cross-section of the wing can be represented using a ball and stick diagram, where the ball corresponds to the leading edge of the wing, and the stick corresponds to the orientation of the wing chord (Fig. 5.1B). To turn, the insects must induce asymmetries between their left and right wing strokes. These asymmetries are most prominent in the 6 consecutive strokes that initiate the turning maneuver. We therefore use a phase averaging method to determine the average left and right wing motions for these 6 strokes [64]. The average

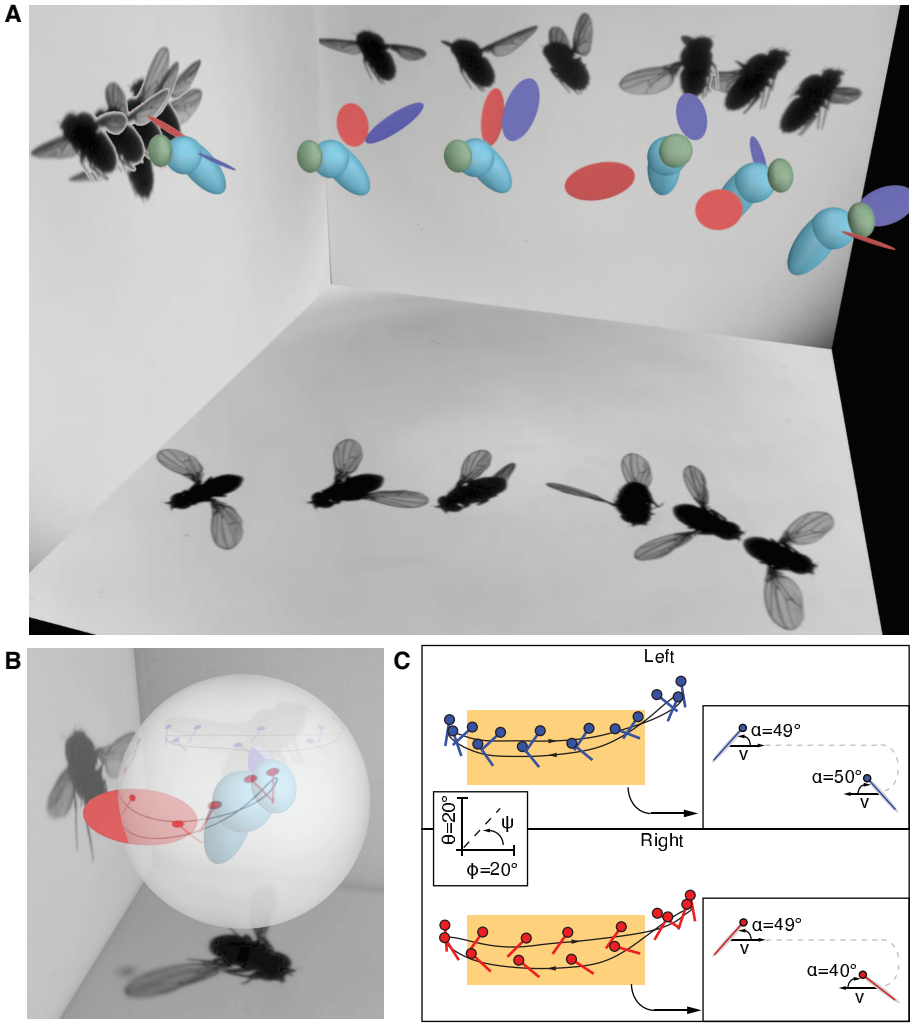

Figure 5.1: (**A**) Phases of motion of a fruit fly, *D. melanogaster*, during a turning maneuver (inspired by the chronophotographs of Étienne-Jules Marey). The panels depict the shadows of the fly as recorded by high speed videography, while the 3D model depicts the motion of the fly as reconstructed from the silhouettes. The fly starts out facing right and over the course of 18 wing beats, 80 ms, completes a 120° clockwise turn while moving 16 mm from right to the left. (**B**) Insects rotate their wings about a hinge. Thus, relative to the insects body, a cross section of the wing along the span moves approximately on a globe. (**C**) We show how the wing cross-section moves during a typical stroke of the maneuver. The average stroke is determined from measured kinematics using the method described in [64]. The lines are snapshots of the position and orientation of the wing chord, $\hat{c}$, during the stroke, while the circles indicate the leading edge of the wing. The color of the circles correspond to the angle of attack, α, of the wing. The turn is caused by a 9° asymmetry between the mid-stroke average fore- and the aft- angle of attacks of the wing.

motions are shown using the unwrapped ball and stick representations in Fig. 5.1C. The average left and right wing trajectories in the $\phi - \theta$ plane are shown by the black lines. In addition, we visualize the pitch of the wings at equally spaced time increments using the orientations of the ball and stick diagrams. The wing angle of attack, α, may be read from the diagram as the angle between the stick and its trajectory. The mid-stroke, labeled in orange, is where most of the aerodynamic forces are produced. Here, the fore- and aft- segments of the left wing motions are nearly symmetric and average α values of about 49° and 50°, respectively. Consequently, the thrusts produced by each stroke segment cancel. In contrast, the fore- and aft- segments of the right wing motions have α values of 49° and 40° respectively. This 9° difference in α breaks the fore-aft symmetry of the stroke and produces a differential thrust that turns the insect clockwise. Thus, the wing's angle of attack and consequently its pitch plays an important active role in maneuvering flight.

5.3 Wing Pitching Largely Passive

The observation that the insect is manipulating wing pitch is consistent with previous measurements of turning and sideways flight [24,25,27,80]. However, it has also been shown that the pitching motion of the wings can be passive [1, 18, 29, 53, 73]. To elucidate which aspects of the wing pitching are actively controlled, we back out the torque acting at the wing hinge,

$$\vec{\tau}_i = \mathbf{I}_w \cdot \dot{\vec{\omega}} - \vec{r} \times m_w \vec{a} - \vec{\tau}_a. \tag{5.1}$$

Here, we experimentally determine the acceleration $\vec{a}$ and rotational acceleration $\dot{\vec{\omega}}$ of the wing centroid, as well as the wing morphology parameters: mass,

m_w, moment of inertia, $\mathbf{I}_w$, and center of mass to hinge vector, $\vec{r}$. The aerodynamic torque on the wings, $\vec{\tau}_a$, is extracted from simulations (see §6.3.2). Using this calculation, we are able to back out the torque component associated with pitching, τ_p, for all 18 wing strokes. These data are used to analyze the differences between the torques applied during the turn and during steady flight.

For steady flight it has been shown that wing pitching is passive [29, 53, 71] and suggested that the pitching torques result from torsional deformation of the wing veins [18, 73, 81, 82]. To test whether these ideas can be integrated into a dynamical model for the wing hinge torques, we plot τ_p versus ψ for the final 9 consecutive strokes associated with symmetric wing motions (Fig. 5.2A). The torque data traces out an elliptical curve whose major axis has a negative slope. This negative correlation indicates that when the wing angle deviates from approximately 90° the hinge produces a restoring torque. The area enclosed by the ellipse indicates the energy dissipated by the hinge as it pitches the wing. These two observations suggest that the wing hinge acts like a damped torsional spring so that,

$$\tau_p = -\kappa\,(\psi - \psi_0) - C\dot{\psi}, \tag{5.2}$$

where the parameters κ, C, and ψ_0 correspond, respectively, to the torsion constant, damping constant and the rest angle of the torsional spring. Remarkably, we find that fitting this model to all 9 wing strokes, the values $\kappa = 91 \pm 9$ pN m/°, $C = 39 \pm 12$ fN m s/°, and $\psi_0 = 90° \pm 1$ account for about 95% of the variance of the pitching torque.

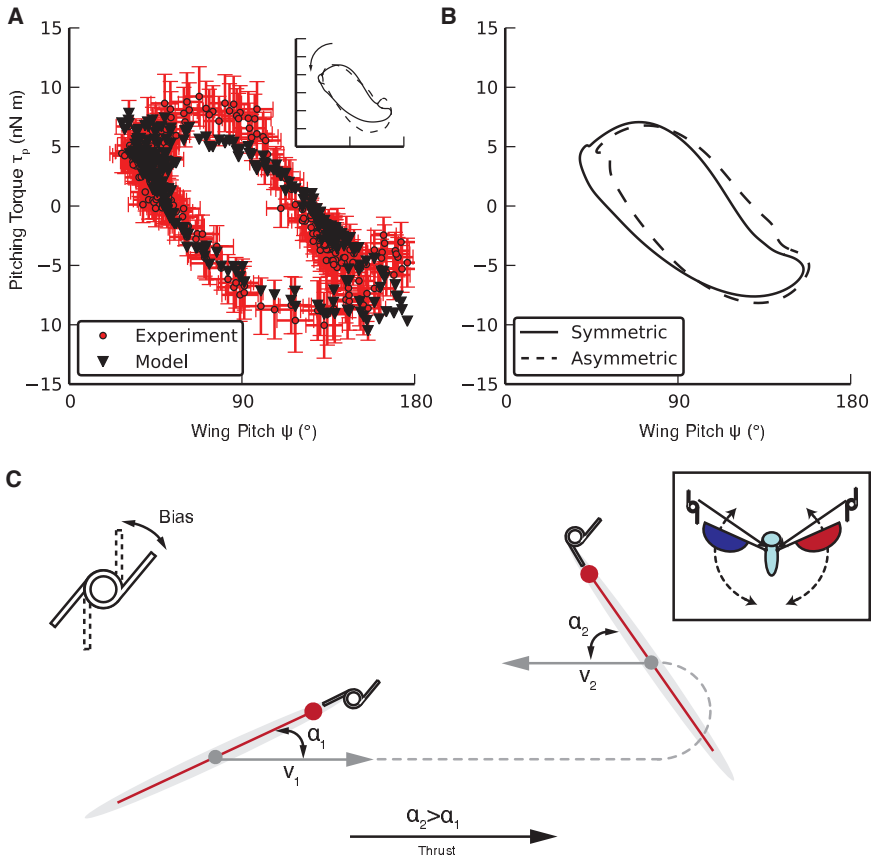

Figure 5.2: (**A**) We show the pitching torque, τ_p, as a function of the wing pitch angle, ψ, for the nine strokes associated symmetric wing movements. Each red dot is a snapshot corresponding to a frame of the flight sequence. Error bars are propagated measurement errors. Black triangles are the result of modeling τ_p using a damped torsional spring model. The torque is highly correlated to the wing pitch and traces out an elliptical curve. This is highlighted by the figure in the inset, where we show τ_p versus ψ for the phase averaged stroke with the solid line. The torsional spring model is shown by the dashed line. The direction of propagation along the curve indicates the motion is damped. (**B**) We show the results of comparing the phase averaged τ_p to ψ for strokes associated with symmetric wing movements and asymmetric ones that induce the turn. The elliptical curves are shifted relative to one and other. (**C**) We show the virtual fly model. We model each wing hinge of the fruit fly by like a damped torsional spring. Driving is modeled by prescribing the amplitude and deviation of the wings. The pitch of each wing and the yaw of the body are determined by the dynamical model that couples aerodynamic forces, the morphology of the body and wings with the torsional spring which is located at the wing base. By biasing the orientation of the torsional springs, $\Delta\psi_0$, the fly can produce an asymmetric angle of attack between the fore- and the aft- stroke and is the that ultimately induces a turn.

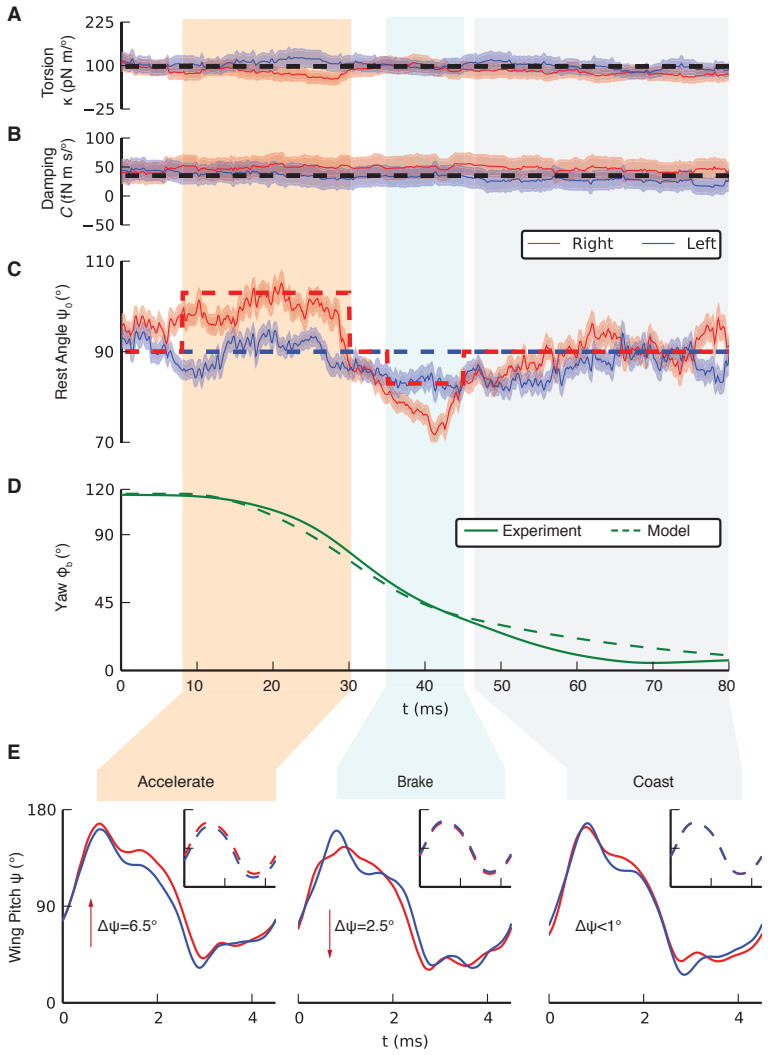

Figure 5.3: (**A**)–(**C**) The time dependence of the torsional spring parameters. Shaded regions indicate parameter values extracted from experiment. The thickness of each region corresponds to measurement uncertainties determined by a Monte Carlo method. The torsion and damping constants do not vary within error bars, while the spring rest angles have significant changes that correlate the yaw movements of the fly. For comparison the timescale of a wing beat is 4.5 ms. (**D**) We compare the measured yaw angle of the fly (solid-line) and the virtual fly (dashed-line). The virtual fly flaps with symmetric amplitude and no deviation angle, while κ and C are held constant as in (A) and (B) and ψ_0 is varied as in (C) (**E**) We show the phase-averaged wing pitch, ψ, for one complete stroke in the three labeled regions. Solid lines are experimental measurements, while dashed lines in the inset axis are corresponding strokes from the virtual fly. The shift $\Delta\psi$ in the three regions are 6.5° (accelerate), 2.5° (brake), and $< 1.0°$ (coast). The corresponding $\Delta\psi$ for the virtual fly are 8° (accelerate), 2.9° (brake) and 0° (coast).

5.4 Insects Modulate Passive Wing Pitching

To determine how the wing pitch is actuated differently during the turn, we repeat this analysis for the 6 strokes that initiate the maneuver. We then compare the phase averaged data for these strokes with the phase averaged data for the 9 steady strokes (Fig. 5.2B). We find that the data sets are shifted with respect to each other, indicating a change in ψ_0. In fact, by plotting the values for κ, C and ψ_0 as a function of time, we show that ψ_0 is the only parameter in the model that varies throughout the maneuver (Fig. 5.3A–C). Comparison with the yaw versus time data in Fig. 5.3E indicates that to initiate the clockwise turning maneuver (orange shading), the insect increases the ψ_0 of the right wing relative to the left by about 15° for six strokes. Interestingly, we find that for the two subsequent wing beats (blue shading) the insect decreases the ψ_0 of the right wing relative to the left by about 10°. This reversal in the sign of $\Delta\psi_0$ indicates that the insect is generating a counter-clockwise torque that slows its yaw. In the final 9 wing strokes (gray shading) we find that the ψ_0 values for the left and right wings are nearly equal so that no active torques are generated. This correlation between $\Delta\psi_0$ and the yaw dynamics of the fly is observed for all 10 movies we have analyzed. These data suggest that changes to ψ_0 alone are responsible for controlling wing pitch during the turn.

To further test this hypothesis, we simulate the coupled wing-body dynamics in a virtual fly. The driving of each wing is simulated by prescribing its amplitude and deviation angle while the spring model in Eq. 5.2 is used to determine the wing pitch. In response to aerodynamic forces on the wings, the virtual fly is allowed to freely yaw but is otherwise held fixed (see §5.7 for further details). To isolate the effect of varying ψ_0, the variables κ and C are held con-

stant (dashed lines in Figs. 5.3A,B), θ is set to zero, and ϕ is driven sinusoidally with a flapping amplitude and frequency that match the experiments. The rest angle ψ_0 for the left and right wings are prescribed, respectively, by the blue and red dashed lines in Fig. 5.3C, which capture the observed trends. Furthermore, we ensure that locally the area between the dashed lines match the total area enclosed between the two experimental curves. In Fig. 5.3D we compare the predicted and observed yaw dynamics. We find that the predicted yaw dynamics of the virtual fly (dashed line) quantitatively match the experimentally measure yaw data (solid line). In addition, this simple model also quantitatively recovers the average pitch asymmetries in the three different portions of the maneuver. As a final check, we also find that simulating the detailed amplitude and deviation angles of the stroke with a constant $\psi_0 = 90^\circ$ for both wings does not lead to asymmetric wing pitch angles and therefore does not yield a turn. These simulations confirm that changes to ψ_0 alone bias the passive wing pitching and lead to the observed yaw dynamics. This remarkable result elucidates how insects control their passively pitching wings even during extreme maneuvers.

5.5 Fruit Flies Control Turn by Modulating Wing Pitching

Our results show that to turn insects do not need to directly control all aspects of their wing motions. Such largely passive actuation mechanisms have been shown to greatly simplify the control needed to generate complex movements in aquatic and terrestrial locomotion [83,84]. To determine whether this strategy also leads to simple control for actuating turns in insect flight, we determine the dependence of body yaw on $\Delta\psi_0$. Simulations and experiments show that the

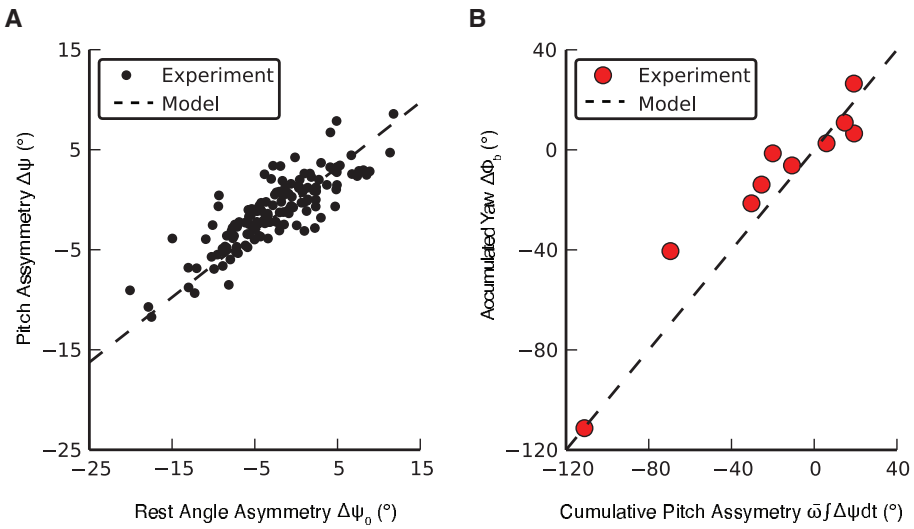

Figure 5.4: (**A**) The asymmetry in wing rest angles, $\Delta\psi_0$, is linearly related to the asymmetry in wing pitch angles, $\Delta\psi$. value found From simulations of a virtual we find that $\Delta\psi = \mu\Delta\psi_0$ with $\mu = 0.65$ (dashed line). This is in agreement with the value determined from experiment, $\mu = 0.5$. The errors in pitch asymmetry and rest angle asymmetry are on the order of the spread of the data and have been omitted for clarity. The data points on the figure are average values of $\Delta\psi$ and $\Delta\psi_0$ for over a stroke. (**B**) The yaw angle of a turn is linearly related to wing pitch asymmetry accumulated during the maneuver. We show analytically and with simulations of th virtual fly that this relationship is $\Delta\phi = \bar{\omega}\int\Delta\psi dt$, where $\bar{\omega}$ is the average angular frequency of the wings. The model prediction (dashed line) is in agreement with experimental measurements. The data points in the figure summarize ten turning maneuvers. The errors in the turn angle and the mean asymmetry are on the order of the size of the marker and have been omitted for clarity.

offset between wing pitch angles $\Delta\psi \approx \mu\Delta\psi_0$ (Fig. 5.4A and §5.8). The experimental data from 147 separately analyzed wing strokes (black points) indicates that $\mu = 0.5$. This is in agreement with simulations of the symmetrically flapping virtual fly (dashed line) where we find $\mu = 0.65$.

The offset in wing pitch angles can be related to the yaw dynamics by,

$$I_b\ddot{\phi}_b + 2\bar{\omega}C_\tau\dot{\phi}_b = 2C_\tau\bar{\omega}^2\Delta\psi, \tag{5.3}$$

where I_b is the moment of inertia of the fly about the yaw axis, C_τ is a parameter

that depends on the drag coefficient and the wing geometry, $\bar{\omega}$ is the average angular velocity of the wings, and ϕ_b is the yaw of the body (see 5.9). When $\Delta\psi = 0$, Eq. 5.3 reduces to the passively damped yaw motion characteristic of flapping flight [76, 77]. When $\Delta\psi \neq 0$, a driving torque actively yaws the fly. Furthermore, by integrating Eq. 5.3 over time we find that the accumulated yaw,

$$\Delta\phi_b = \bar{\omega} \int \Delta\psi dt \approx \bar{\omega}\mu \int \Delta\psi_0 dt. \tag{5.4}$$

Thus, adjustments to the relative rest angle of the wings provide a direct, linear control of the accumulated yaw angle for a turn. To determine if Eq. 5.3 alone accounts for the observed yaw dynamics we plot $\Delta\phi_b$ versus $\bar{\omega}\int\Delta\psi dt$ for the experiment data in Fig. 5.4B. We find that the data for all 10 turning maneuvers is in excellent agreement with the prediction of Eq. 5.4. This analysis demonstrates that the mechanical properties of the wing hinge, lead to a simple wing actuation mechanism with a single linear control variable, $\Delta\psi_0$ for inducing in flight turns.

This control strategy provides an elegant mechanism by which *Drosophila* can control their wings with flight muscles that have a slow response time to neural signals [20]. Specifically, fruit flies have musculature that affects the pitch of their wings [16, 19]. Within our model, these muscles act to bias the rest angle of their wings, ψ_0. Our analysis predicts that, to initiate a turn, *Drosophila* activate their steering muscles over the course of a few wing beats with no need for a fast response time. This prediction can be tested by measuring action potentials in flight muscles of tethered insects. The remaining parameters in our actuation model, κ and C, may describe material constants of the wing hinge. Beyond the fact that they do not vary during these maneuvers, we find that our estimate for $\kappa \approx 90$ pN m/° agrees with scaled estimates for the torsion constants

taken from measurements on the wings of house flies [73]. Finally, because the turning dynamics of isometrically scaled animals are similar over a wide range of length scales [77], we expect that the simple mechanism used by fruit flies may be used by a wide range of animals and, in fact, may greatly simplify the control of micro air vehicles [85].

5.6 Detailed Experimental Kinematics

We show the detailed wing and body kinematics of a freely flying D. melanogaster in Fig. 5.5. The fly performs a 120° clockwise turn in 80 ms (see Fig. 5.1). At the same time, the body pitch remains constant and the body rolls slightly from 0° to a maximum value of 25° near the end of the turn. During the turn, the fly moves 16 mm across the filming volume, while otherwise remaining level. Therefore, the motion of the fly consists mainly of a rapid reorientation in the yaw direction.

The fly induces this turn with subtle asymmetries between the wing motion of the its left and right wings. During the flight, the insect flaps its wings back and forth at an amplitude of approximately 150°. Initially, the amplitudes of the wings are symmetric and centered around 90°. This corresponds to a fly flapping similarly to Fig. 5.6A. In contrast, between 10–40 ms in Fig. 5.5 the amplitudes of the left and right wings can been seen to spread. The right wing drifts towards the anterior part of the fly (towards 0°), while the left wing approaches the posterior (towards 180°). This corresponds to a slow, nearly symmetric, rotation of the stroke amplitude about the fly body (Fig. 5.6B). From 40–70 ms the stroke amplitudes rotate back until they are once again symmet-

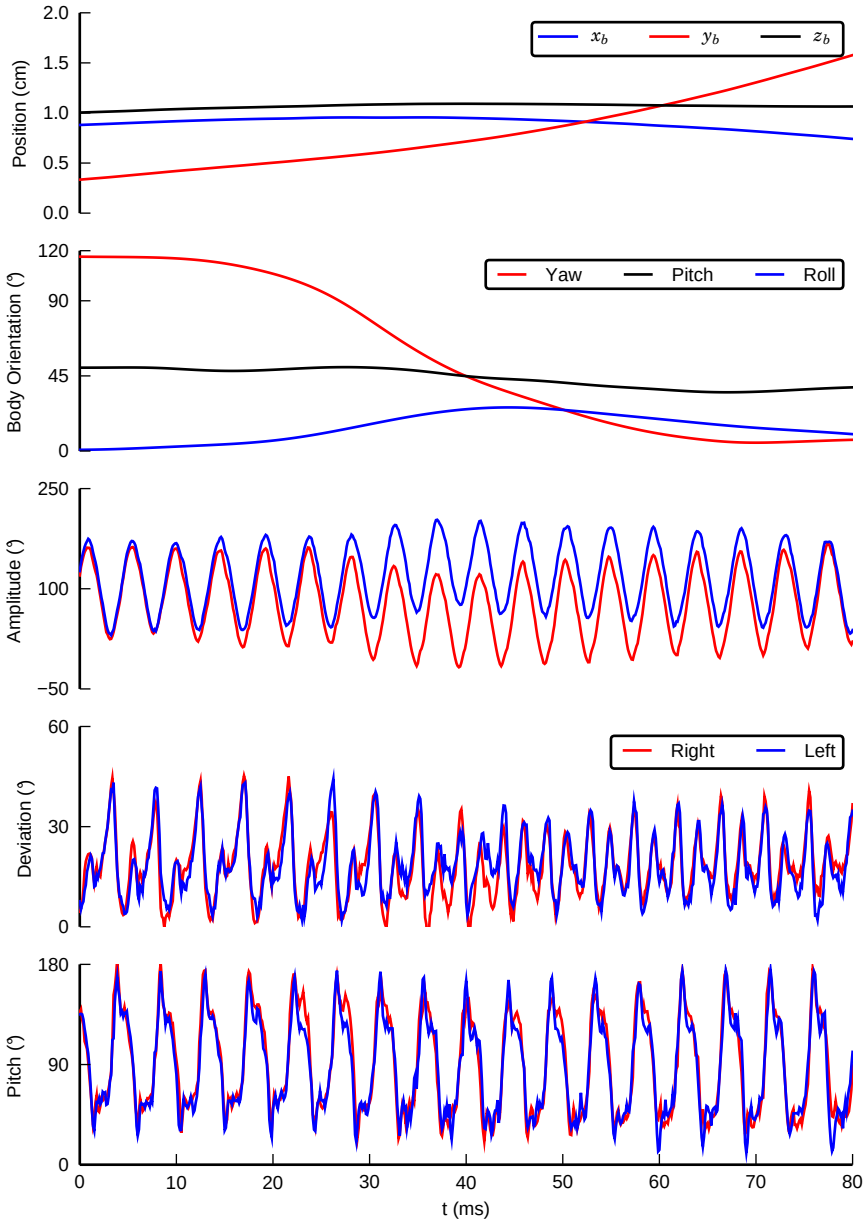

Figure 5.5: We show the kinematics of a freely flying *D. melanogaster*. During the 80 ms flight sequence the fly performs a 120° clockwise turn (Fig. 2.1), while the body remains level and moves 16 mm. The motion is mostly a reorientation of the yaw of the body.

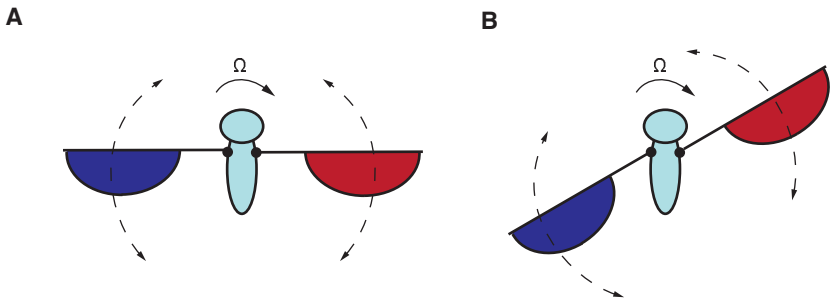

Figure 5.6: (**A**) We show a fly flapping with a symmetric stroke amplitude. (**B**) A fly flapping the stroke amplitudes rotated with respect to the body. This corresponds to the gradual spreading of amplitudes in Fig. 5.5

ric. This trend cannot be the cause of the maneuver: slowly rotating the sweep plane of the insect itself does not change the aerodynamic forces on the fly. In addition, the wings weigh only 0.3% as much as the body, therefore the inertial effect of this rotation is also negligible. Therefore, this motion alone does not result in a net force on the body. We, however, believe that this trend may result from a passive mechanical response of each wing to the aerodynamic drag that is induced by the turn and may reduce the flapping counter-torque experienced by the fly [77].

By removing this trend between the wings, we observe that the right wing flaps at a slightly higher amplitude (6° difference) than the left during the initiation of the turn (10–40 ms in Fig. 5.5). Furthermore, we find that the peak to peak deviation angle of the right wing is increased with respect to the left (especially visible from 30–50 ms in Fig. 5.5). We find that these asymmetries in the amplitude and deviation angles of the wings do not cause the torque that yaws the fly. In fact, we find that they provide a counter-torque to the yaw motion (Fig. 5.7). During the fore- portion of the stroke, the wings travel nearly identical angular distances. Therefore, they will have similar angular velocities and consequently experience similar drag. On the aft- port of the stroke, how-

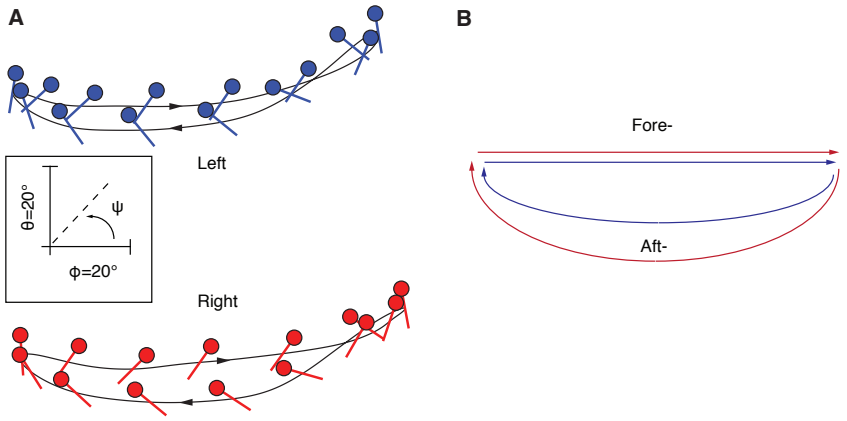

Figure 5.7: (**A**) We show the unwrapped ball and stick representation of the wing motion of the right and left wings. The right wing has a slight, but visible increase in amplitude with respect to the left of 6°. In addition, the peak to peak deviation angle of the right wing increases with respect to the left. This is visible from 30–50 ms in Fig. 5.5. (**B**) We highlight the differences in amplitude and deviation angles of the right and left wings by showing representations of their paths on top of each other. For the fore- stroke the right and left wing will have nearly equal velocities and therefore experience similar drag. For the aft-stroke the exaggerated deviation angle the right wing causes it to have an increased angular velocity and therefore increased drag. This effect results in a net counter-clockwise torque on the fly and thus opposes the motion.

ever, because of it's asymmetric deviation and pitch angles, the right wing has a higher angular velocity than the left. Consequently, it will experience increased drag. The net effect of these strokes is a counter-clockwise yaw torque on the fly that tends to oppose its yaw motion.

Finally, the fly also has a slight roll throughout this turn. This roll, however, is minimal until the end of the turn and therefore does not contribute to it. The increase of the right pitch angle with respect to the left is clearly visible from 15–40 ms in Fig. 5.5. We find through simulation and mathematical modeling that this asymmetry alone is sufficient to fully explain the yaw maneuver of the fly.

5.7 Virtual Fly: Simulation of Coupled Wing Body Turning Dynamics

We use the model fly shown in Fig. 5.2C to ascertain how direct actuation by the fruit fly couples with aerodynamic and passive mechanical forces on its wings to ultimately drive flight maneuvers. The model fly is allowed to freely yaw, but its position and orientation are otherwise fixed. We constrain the body dynamics to isolate the effect of the wing kinematics on only yaw without the need to focus on the active mechanisms that insects use to stabilize their body kinematics [22, 86]. The wing-mass of *D. melanogaster* is less than 0.3% of its body-mass, we therefore neglect inertial coupling between the wing and body. Driving by indirect flight muscles is thus simulated by directly prescribing the amplitude and deviation angles of the fly wings. The pitch of the wings is determined by a dynamical system that results from aerodynamic torques on the wings coupling with the torsional spring that is used to model passive mechanical compliance of the wing (Eq. 5.2). In addition, we model direct actuation of the wing pitch using the spring rest angle, ψ_0, in Eq. 5.2. The yaw angle, ϕ_b, of the body is determined by the aerodynamic forces on the wings. This results in a coupled dynamical system that determines the wing pitch and the yaw of the fly body,

$$\begin{aligned} I_w \ddot{\psi}_l &= \tau_\psi^{(l)} - \kappa\left(\psi_l - \psi_0^{(r)}\right) - C\dot{\psi}_l \\ I_w \ddot{\psi}_r &= \tau_\psi^{(r)} - \kappa\left(\psi_r - \psi_0^{(l)}\right) - C\dot{\psi}_r \\ I_b \ddot{\phi}_b &= \tau_\phi^{(r)} + \tau_\phi^{(l)} \end{aligned} \tag{5.5}$$

where $\mathbf{I}_w$ is the moment of inertia of each wing about its respective hinge, τ_ψ corresponds to the inertial and aerodynamic torques that pitch the wing and τ_ϕ's are the aerodynamic torques that yaw the body. Similar to [8], we employ

the quasi-steady model described in [87] to simulate aerodynamic forces.

5.8 Wing Pitch Control with Torsional Spring Rest Angle

By simulating the dynamics of a virtual fly (§5.7), we can show that the wing pitch asymmetry, $\Delta\psi$, and the wing rest angle asymmetry, $\Delta\psi_0$ are linearly related. Although the functional relationship cannot be derived analytically, we motivate it analyzing a closely related system. Ignoring the dependence of τ_ψ on the wing pitch and its derivatives, transforms it into the dynamical equation describing the motion of a damped, driven torsional oscillator,

$$I_w\ddot{\psi}(t) + C\dot{\psi}(t) + \kappa\left(\psi(t) - \psi_0\right) = \tau(t). \tag{5.6}$$

Furthermore, when the driving torque, $\tau(t)$, is periodic, the steady state solution of Eq. 5.6 is a periodic function of the form $\psi(t) = \beta(t) + \psi_0$ with the same period as $\tau(t)$. Varying ψ_0 does not change β. Therefore, the difference between two pitch angles governed by Eq. 5.6 but with different ψ_0 values is $\Delta\psi = \Delta\psi_0$. We find that the linear relationship is unchanged when the complete dynamics are considered for ψ, however, the slope is no longer one. By simulating a virtual fly with a symmetric stroke with the amplitude and wing beat matching experiments, we find that,

$$\Delta\psi = \mu\Delta\psi_0 \tag{5.7}$$

with $\mu \approx 0.65$. Moreover, when ψ_0 is varied as a function of time during a flight sequence, the relaxation time between steady state solutions is determined by I_w/C. We find that this is faster than a wing beat, therefore Eq. 5.7 is valid as long as ψ_0 varies slower than this timescale.

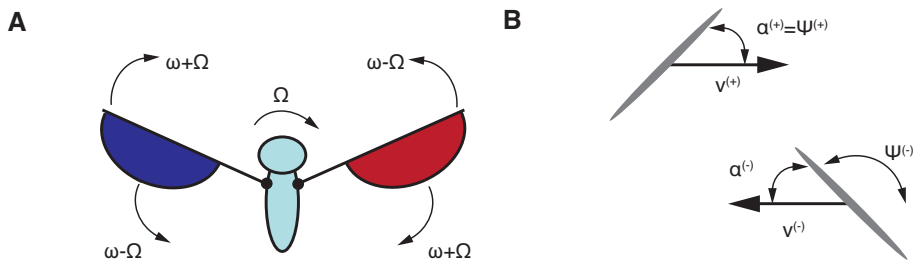

Figure 5.8: (**A**) We show a simplified model fly that is freely allowed to rotate but is otherwise fixed. The wings are fixed relative to the body and their weight is modeled as negligible compared to the body. Stroke amplitudes are left-right symmetric and periodic with constant angular velocities ω, on the fore-, and $-\omega$, on the aft-strokes. (**B**) We depict the cross-section of a wing of the fly. To model how pitch angle asymmetry alone can drive a turn, we consider strokes with constant angle of attack $\alpha^{(+)}$, on the fore-, and $\alpha^{(-)}$, on the aft-stroke. The angle of attack is in general allowed to vary between the left and right wings. Also labeled is the relationship of the geometric pitch angle to the angle of attack for the horizontal stroke plane shown.

5.9 Yaw Control with Wing Pitch Asymmetry

To analytically derive how the pitch asymmetry of a flapping insect can control its body yaw, we introduce the simplified model fly shown in Fig. 5.8. The model is allowed to freely rotate in response to aerodynamic forces on its wings. For the purposes of this analysis we consider a simplified stroke with constant angular velocity wing movements (with respect to the body) on the fore- and aft-strokes. This corresponds to coarse-graining over stroke details to consider only average stroke parameters. Forward strokes are denoted by a plus-sign on kinematic variables, while aft-strokes are denoted by a negative-sign.

During fore- and aft-strokes, the drag on the each wing causes an average torque on the on the fly body,

$$\tau_w^{(\pm)} = \chi \rho_f (\Omega \pm \omega)^2 C_D(\alpha_w^{(\pm)}), \tag{5.8}$$

where Ω is the angular velocity of the body, ω is the angular velocity of the wing, ρ_f is the density of air. The term $C_D(\alpha)$ is the angle of attack dependent drag parameter. This term is well approximated by $C_D(\alpha) \approx C_D \sin^2 \alpha$ [87]. Finally, χ depends on the wing geometry of the fly and is $\chi \approx \frac{7\pi}{8}\bar{c}^5$ where $\bar{c}$ is the chord-length of the wing. The sum of the torques (Eq. 5.8) from the fore- and aft-strokes of each wing is the net torque on the fly body. Thus,

$$I_b\dot{\Omega} = C_\tau\left((\Omega-\omega)^2(\sin^2\alpha_l^{(-)} + \sin^2\alpha_r^{(+)}) - (\Omega+\omega)^2(\sin^2\alpha_r^{(-)} + \sin^2\alpha_l^{(+)})\right), \tag{5.9}$$

where $C_\tau = \chi C_D \rho_f$.

We consider a stroke with a mean shift between the left and right pitch angles of a fruit fly $\psi_l - \psi_r = \Delta\psi$. This allows us to write $\alpha_r^{(\pm)} = \alpha_\pm$ and $\alpha_l^{(\pm)} = \alpha_\pm \pm \Delta\psi$ (See Fig. 5.8B). In addition, because $\Omega \ll \omega$ and $\Delta\psi$ are small,

$$I_b\dot{\Omega} \approx C_\tau\left(-2\Omega\omega(\sin^2\alpha_+ + \sin^2\alpha_-) + \omega^2\Delta\psi(\sin 2\alpha_+ + \sin 2\alpha_-)\right). \tag{5.10}$$

The first term in the above equation corresponds to the exponential decay due to passive damping, while the latter term is a driving torque that arises due to the mean shift in the pitch angles of the fruit fly.

Integrating Eq. 5.10 over a time period such that $\Omega(t_1) = \Omega(t_2)$ yields,

$$\Delta\phi = \omega\frac{\sin 2\alpha_+ + \sin 2\alpha_-}{2(\sin^2\alpha_+ + \sin^2\alpha_-)}\int_{t_1}^{t_2}\Delta\psi dt = \omega\gamma N\Delta\bar{\psi}, \tag{5.11}$$

where $\Delta\phi$ is the net yaw of the fly during a turn. Thus, the body yaw during a turn is directly proportional to the average pitch asymmetry between left and the right wings, $\Delta\bar{\psi}$, the duration (in strokes) of the asymmetry, N, and the mean angular frequency of the flapping wings, ω. For fruit flies, $\alpha_+ \approx \alpha_- \approx 45^\circ$ and so $\gamma \approx 1$.

CHAPTER 6

AERODYNAMIC FORCES ON FLAPPING WINGS

6.1 Introduction

The quantitative study of how insects control their flight requires accurate models of the aerodynamic forces acting on their wings. Not only do these forces propel an insect through the air, but the motion of the wings themselves is also highly coupled to these forces. When viewed in isolation, insect wings have just two sets of external forces acting on them: forces exerted by the flies and aerodynamic forces. Because the wings support the entire weight of flies, these forces balance. Thus, aerodynamic forces and driving forces play a nearly equal role in determining the insect's wing kinematics. In this chapter, we describe the methods that we use to model aerodynamic forces on flapping wings. Although the airflow over an insect's body can play an important role in the insect's neurosensory response [88, 89], the aerodynamic forces on the body are far smaller than the forces on the wings [21]. We therefore do not address these forces here.

The aerodynamic forces acting on flapping wings have been extensively studied and the mechanisms behind force production are established [22]. We, therefore, base our study on extensions to well-tested models. These models fall into two categories: simulation of the flow field around a flapping with using computation fluid dynamics (CFD), and reduced order steady-state models (quasi-steady). Each of these methods allows us to determine the time-dependent aerodynamic forces on a flapping wing, and consequently total aerodynamic force on the insect.

In §6.2 we describe the CFD methods that we use to study the aerodynamic forces on insect wings. We also discuss the modifications that we make to these standard numerical methods to model a wing that passively rotates in response to the fluid flow around it. In addition to CFD methods, in §6.3, we describe the reduced order models that we use to extract forces from the wing kinematics measured in §3.2. We also compare the aerodynamic forces predicted by these quasi-steady models to the net force on the fly as determined from Newton's second law. Finally, we discuss how we propagate errors using these reduced order models.

6.2 Two-Dimensional Navier-Stokes Equations

Insects flap their wings, by rotating their wings about a hinge on their body. The airflow induced by these rotating airfoils is inherently three-dimensional [4, 21, 24, 90–92], however, researchers have shown that the aerodynamic mechanisms behind flapping flight, can be approximated by two-dimensional models [9, 11, 93, 94]. We, therefore, model the airflow around insect wings using these two dimensional computer simulations.

We consider each side of the insect separately. Thus for a fruit fly we simulate the flow field around one wing at a time (see §3), for dragonflies we simulate them two at a time (see §2). To project the motion of each of an insect's rotating wings to a two-dimensional plane, we approximate the motion of a wing to the motion of a cross-section of the wing located at 66% of of the span (Fig. 6.1). This span-wise location is close to the average center of pressure and the point where DPIV measurements indicate that the circulation around insect wings

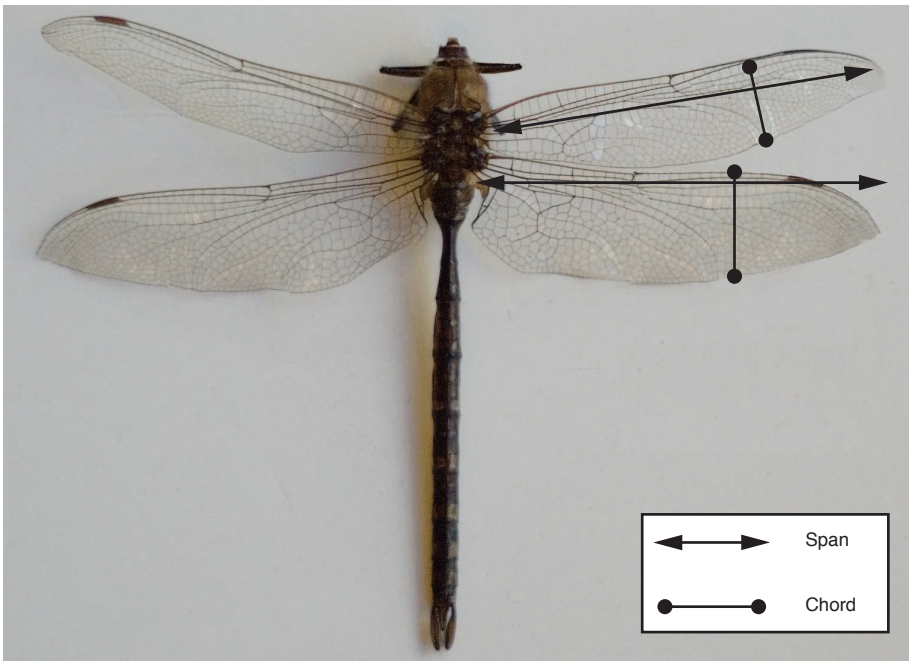

Figure 6.1: To determine the aerodynamic forces on an insect wing from two dimensional solutions of the Navier-Stokes equations, we simulate the motion of a chord located at 66% of the length of the span. Pictured above is a dragonfly, *Libelulla pulchella*, with the approximate chord cross-sections labeled. For CFD simulations, we only simulate the wing(s) on one side of the insect at time.

is the greatest [73, 93]. This procedure transforms the kinematics of a three-dimensional wing rotating about a hinge to a translating and rotating plate. In §6.2.1 and §6.2.2 we detail the numerical methods that we use to simulate the flow around these plates.

6.2.1 Immersed Interface Method

To determine the aerodynamic forces on multiple flapping insect wings, we use the immersed interface method (IIM) [95]. This method determines the unsteady velocity, $\vec{v}$, and pressure, p, fields in a volume of fluid by solving the

Navier-Stokes equations,

$$\begin{aligned} \frac{\partial \vec{v}}{\partial t} + \vec{v} \cdot \nabla \cdot \vec{v} &= -\nabla p + \frac{1}{Re} \Delta \vec{v} + \sum_{l=1}^{M} \vec{B}_l \\ \nabla \cdot \vec{v} &= 0 \end{aligned} \tag{6.1}$$

with body forces, $\vec{B}_l$ described below and boundary and initial conditions,

$$\begin{aligned} \vec{v}\,|_{\delta\Omega} &= 0 \\ \vec{v}(\vec{x}, 0) &= 0 \end{aligned} \tag{6.2}$$

on a staggered Cartesian grid. The Reynolds number, $Re = UL/\nu$ depends on the kinematic viscosity, ν, velocity, U, and length, L, scales of the flow. For flapping wings, U is determined by the amplitude and frequency of flapping, and L is the chord length of the wing. In our simulations, $100 \leq Re \leq 350$, which is matched to the range of fruit flies ($Re \approx 100$) and house flies ($Re \approx 350$). The dimensionless forces (lift and drag coefficients), however, are insensitive to Re in the flow regime that corresponds to insect flight [26, 96, 97]. Therefore, we use $Re = 350$ to simulate the wing motion of a dragonfly even though its flight corresponds to $Re \approx 1000$.

To simulate the flow around flapping wings, boundaries are represented by the addition of time-dependent singular body forces in Eq. 6.1,

$$\vec{B}_l(\vec{x}, t) = \oint_{\delta\Omega} \vec{b}_l(\alpha, t) \delta(\vec{x} - \vec{X}_l(\alpha, t)) d\alpha, \tag{6.3}$$

where $\vec{X}_l(\alpha, t)$ is the (time-dependent) position of each (Lagrange) point on the surface of the boundary, $\delta\Omega$, that is parametrized by non-dimensional parameter α (Fig. 6.2). The motion of the boundary is determined by,

$$\frac{\partial \vec{X}_l(\alpha, t)}{\partial t} = \vec{v}(\vec{X}(\alpha, t), t). \tag{6.4}$$

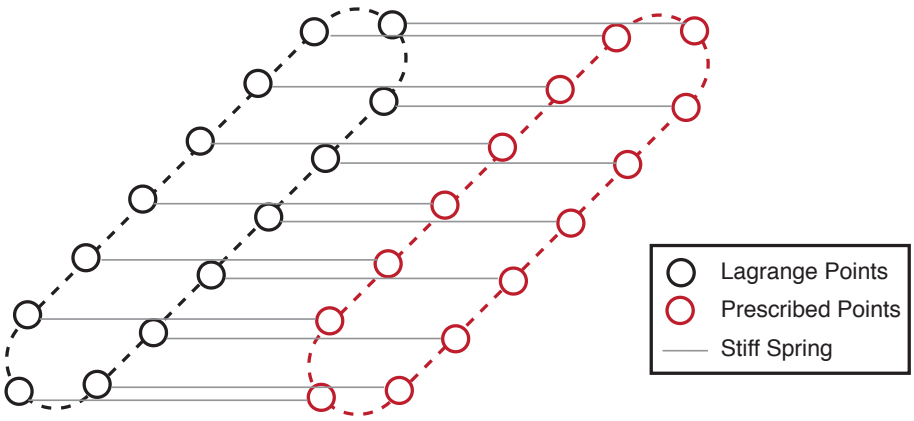

Figure 6.2: The coordinates of surface l are represented by a set of Lagrange points, $\vec{X}_l(\alpha_n, t)$, where $n = 1..N$ are shown by the black circles above. The continuous function $\vec{X}_l(\alpha, t)$, shown by the dashed black line, is interpolated from $\vec{X}_l(\alpha_n, t)$. To prescribe $\vec{X}_l(\alpha_n, t)$ to desired positions $\vec{X}_l^{(e)}(\alpha_n, t)$, represented by the red circles, we connect $\vec{X}_l^{(e)}(\alpha_n, t)$ to $\vec{X}_l(\alpha, t)$ with stiff springs. The singular force density at a black circle is the force of the spring connecting it to the corresponding red circle.

For IIM, the jumps caused in Eq. 6.1 by the singular force density, $\vec{b}$, are incorporated directly into finite differencing scheme used in the numerical method [98]. This enables the method to attain second order spatial accuracy.

To prescribe the motion of the a boundary to $X_l^{(e)}(\alpha, t)$, we let

$$\vec{b}_l(\alpha, t) = -\kappa(\vec{X}_l(\alpha, t) - \vec{X}_l^{(e)}(\alpha, t)), \tag{6.5}$$

where κ is a stiff spring constant with value of $\kappa = 10^4$, and

$$\vec{X}_l^{(e)}(\alpha, t) = \mathbf{R}(\psi_l(t))\vec{X}_0(\alpha) + \vec{x}_l(t), \tag{6.6}$$

is the prescribed boundary position of a wing whose centroid is $\vec{x}_l(t)$, orientation is $\psi_l(t)$, and shape is parametrized by $\vec{X}_0$. We represent $\vec{b}$, $\vec{X}_l$ and $\vec{X}_l^{(e)}$ by discretizing their values over the surface of the wings. The prescribed boundary pulls the points on the surface along its trajectory (Fig. 6.2). Accurate prescription of wing kinematics requires springs with very large spring constants, therefore,

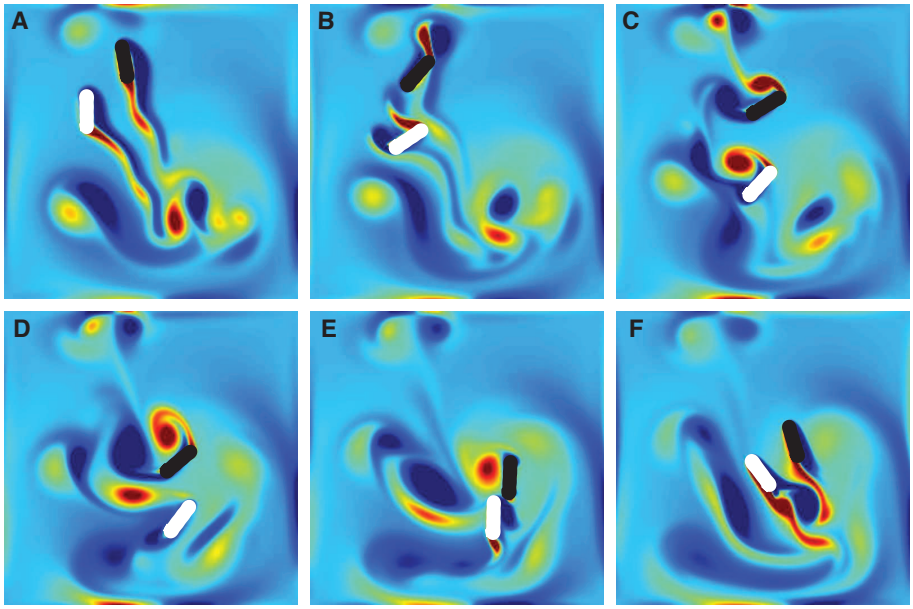

Figure 6.3: Six equally spaced time increments of the vorticity during a single stroke of two simulated flapping boundaries. The kinematics are those corresponding to a dragonfly forewing (shown in black) and hindwing (shown in white). Red is positive vorticity and blue is negative vorticity.

the system becomes very stiff [99]. We find that these springs are the limiting factor that determine the maximum stable time-step of the simulation.

In Fig. 6.3, we show six equally spaced time increments of the vorticity field during a single stroke of prescribed dragonfly wing kinematics simulated with IIM (see §2). From such a simulated flow field ($\vec{b}_l(\alpha, t)$, $\vec{v}(\vec{x}, t)$ and $p(\vec{x}, t)$), the aerodynamic forces on the boundaries are,

$$\vec{F}_l(t) = -\oint_{\delta\Omega} \vec{b}_l(\alpha, t) d\alpha + m\ddot{x}_l(t), \tag{6.7}$$

where m is the mass of fluid enclosed by the wing boundary [95]. The torque about the wing centroid is,

$$\tau = \oint_{\delta\Omega} \epsilon_{ij} r_i \sigma^+_{jk} n_k ds, \tag{6.8}$$

where ϵ_{ij} is the two dimensional Levi-Civita symbol, r_i is the vector from the

centroid of the wing to its boundary, and n_j is the outward pointing surface-normal. We drop the superscript l on τ, $\vec{r}_l$ and σ_l for clarity. The stress tensor on the outer surface of the wing, σ^+, can be written in terms of

$$\sigma^+_{ij} = -\frac{b_i}{J} + \sigma^-_{ij} n_j, \tag{6.9}$$

σ^-_{ij}, the stress tensor on the inner surface of the wing boundary, and the surface Jacobian, $J = \frac{ds}{d\alpha}$ [98]. Then,

$$\begin{aligned}
\tau &= -\oint_{\delta\Omega} \vec{r} \times \vec{b} d\alpha + \oint_{\delta\Omega} \epsilon_{ij} r_i \sigma^-_{jk} n_k ds \\
&= -\oint_{\delta\Omega} \vec{r} \times \vec{b} d\alpha + \oint_{\Omega} \vec{r} \times \left(-\nabla p + \frac{1}{Re} \nabla^2 \vec{v} \right) dA \\
&= -\oint_{\delta\Omega} \vec{r} \times \vec{b} d\alpha + \frac{\mathrm{d}}{\mathrm{d}t} \int_{\Omega} \vec{r} \times \vec{v} dA,
\end{aligned} \tag{6.10}$$

Numerical Validation

To test the robustness of the aerodynamic forces determined with IIM to numerical approximations, we simulate the kinematics of a tethered dragonfly (See §2). For the sake of brevity, we show only the fluid power, $P = \vec{F} \cdot \dot{\vec{x}} + \tau\dot{\psi}$, of the dragonfly's hindwing. This quantity is chosen because its computation involves all the aerodynamic forces and results are identical to those for $\vec{F}$ and τ. In addition, by choosing the hindwing, we ensure that the down-wash from the forewing remains resolved. For all robustness tests, the wing motion is simulated at $Re = 200$ for two wing beats and then the comparisons of P are shown for the subsequent three wing beats.

To test the spatial convergence of simulations, we simulate aspect ratio, $AR = 6$, flapping wings in an 8×8 chord-length box, and $dt = 5 \cdot 10^{-4}$. We find that a

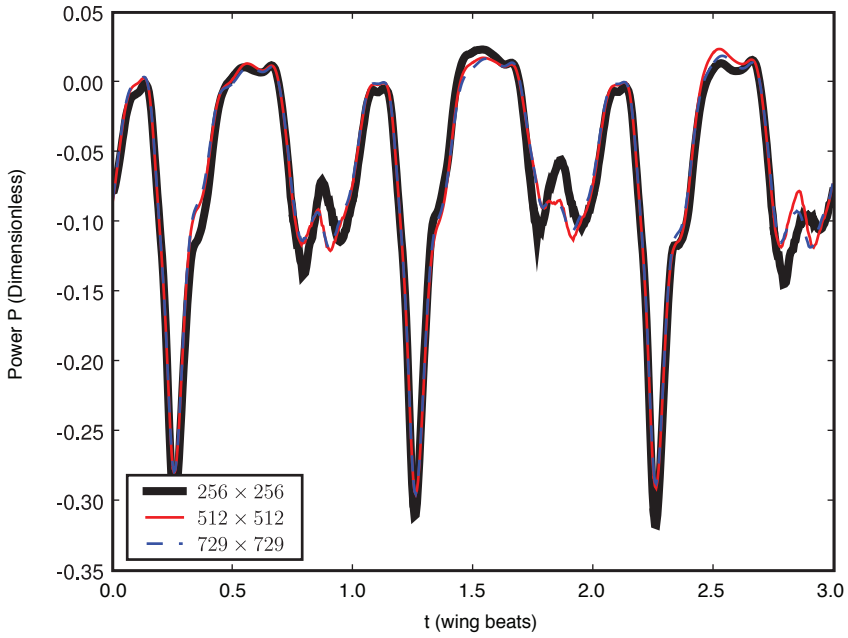

Figure 6.4: Spatial convergence tests for IIM are conducted by simulating dragonfly wing kinematics (see §2.4) at grid resolutions of 256×256, 512×512 and 729×729 in an 8×8 chord length domain size. Above, we show the rate of work done by the fluid on the hindwing, P. We find that a grid resolution of 256 is sufficient to ensure convergence of average aerodynamic quantities to better than 1% compared to the 729×729 grid. Quantities are shown in dimensionless form, with the dimensions of time being beats, and force being the weight of the dragonfly.

grid resolution of 256×256 is sufficient to ensure convergence of P to within 1% for a 256×256 grid when compared to a 729×729 grid (Fig. 6.4). To test the time resolution of the simulation, we vary the time-step as shown in Fig. 6.5 with an $AR = 6$ wing, in an 8×8 chord-length box and a grid resolution of 256×256. We find that $dt = 5 \cdot 10^{-4}$ (10000 time-steps per wing beat) is sufficient to ensure convergence of P to within 1% (Fig. 6.5).

To test the effect of the size of the simulated domain on aerodynamic quantities, we simulate the varying domain sizes, while holding all other parameters constant. The dominant effect of domain size changes is to disrupt the nearly

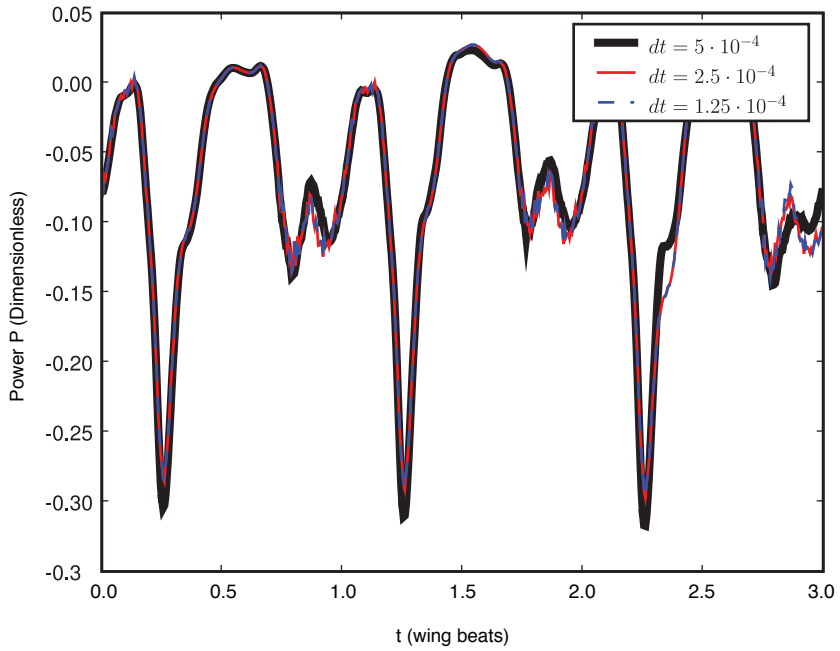

Figure 6.5: We test temporal convergence of IIM by simulating dragonfly wing kinematics (see §2.4) at time resolutions of $dt = 5 \cdot 10^{-4}$, $dt = 2.5 \cdot 10^{-4}$ and $dt = 1.25 \cdot 10^{-4}$, where $t = 1$ corresponds to one wing beat period. Above, we show the rate of work done by the fluid on the hindwing, P. We find that $dt = 5 \cdot 10^{-4}$ is sufficient to ensure convergence of average aerodynamic quantities to better than 1%. Quantities are shown in dimensionless form, with the dimensions of time being beats, and force being the weight of the dragonfly.

vertical jet ejected by the flapping wings (see Fig. 6.3). We therefore show the results of lengthening the domain size in the vertical direction. The wings are simulated in domains with width equal to 8 chord lengths and lengths, $L = 8,\ 16\ 23$ and 128 chord lengths. We find that restricting the domain size to a 8×8 chord-length grid has negligible (P converes to better than 3%) effect on aerodynamic forces and torques (Fig. 6.6A–B).

Insect wings typically have an extremely high cross-sectional aspect ratio. This makes exact simulations of their morphology infeasible [14]. To investigate the effect of wing shape on the aerodynamic forces of a flapping plate, we simulate flapping dragonfly wings in an 8×8 chord-length box, on a 256×256

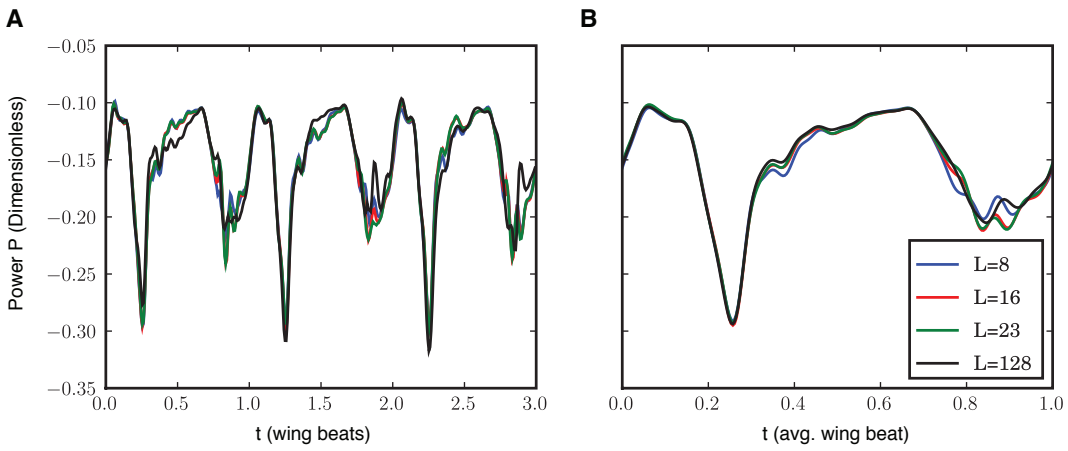

Figure 6.6: (**A)** To test the sensitivity of simulations to domain size, we simulate dragonfly wing kinematics (see §2.4) in domains ranging from 8×8 to 8×128 chord lengths. The dominant effect of domain size is the vertical is to disrupt the vertical jet that is created ejected by the flapping wings we, therefore, show only the results of extend the domain in this direction. Above, we show the rate of work done by the fluid on the hindwing, P. We find that the domain size has less than 3% effect on the average P, and lesser effect on forces. (**B)** Because interaction with vorticies varies wing beat to wing beat we show the phase averaged P for a stroke constructed from the average of 5 wing beats. This highlights that extending the domain size has little effect on P. Quantities are shown in dimensionless form, with the dimensions of time being beats, and force being the weight of the dragonfly.

grid with $dt = 5 \cdot 10^{-4}$ for three different aspect ratios, $AR = 3$, 4, and 6, of rounded rectangle wings. We show the results of our simulation for the aerodynamic power of the fluid on the wing Fig. 6.7. We find that the aerodynamic forces on the flapping wings are very similar (mean P difference is less than 3%) for $AR = 4$ and $AR = 6$, however we find significant changes between these and $AR = 3$. This result is in agreement with findings that, for typical wing strokes, aerodynamic forces are insensitive to wing aspect ratio when $AR \geq 4$ [100, 101].

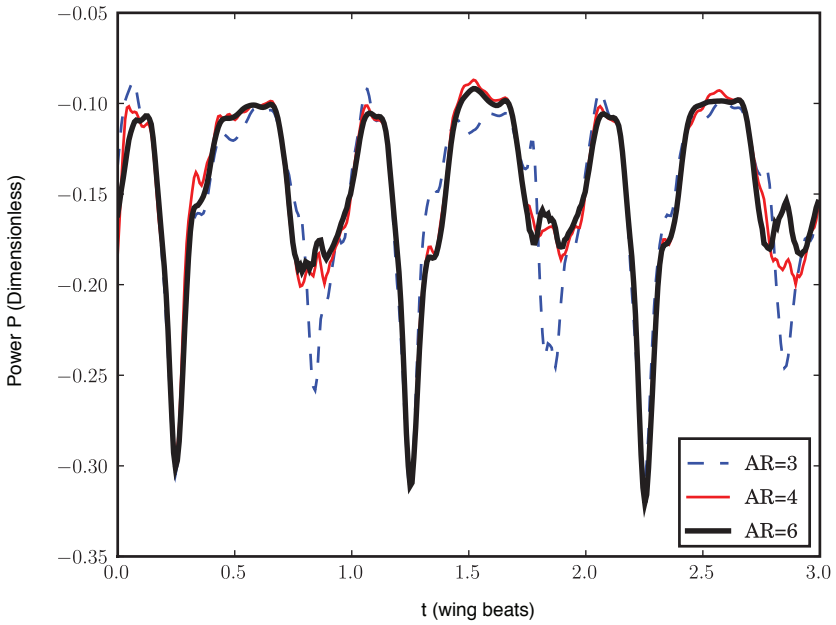

Figure 6.7: To test the sensitivity of simulations to wing aspect ratio, AR, we simulate dragonfly wing kinematics (see §2.4) using rounded rectangle wings of aspect ratio $AR = 3$, $AR = 4$ and $AR = 6$. Above, we show the rate of work done by the fluid on the hindwing, P. We find that there are significant differences in P between the $AR = 3$ curves and the other, however $AR = 4$ and $AR = 5$ converge to better than 3%. Quantities are shown in dimensionless form, with the dimensions of time being beats, and force being the weight of the dragonfly.

Passive Wing Pitching in IIM

The pitch of an insect wing is its orientation about the wing span (Fig. 6.1). Within the two dimensional model of flapping flight pitch maps to the orientation of the boundary in the flow, ψ (Fig. 6.8). Here, we describe modifications we made to IIM to model a wing where ψ, like a sheet of paper waved back and forth, is determined passively by the wing's interaction with the surrounding fluid (see §2–5). We show the specific wing which is simulated in Fig. 6.8. To model a passively pitching wing, we simulate a wing where the x- and y- motion of a point near the leading edge of the wing, the torsion axis, (black circle)

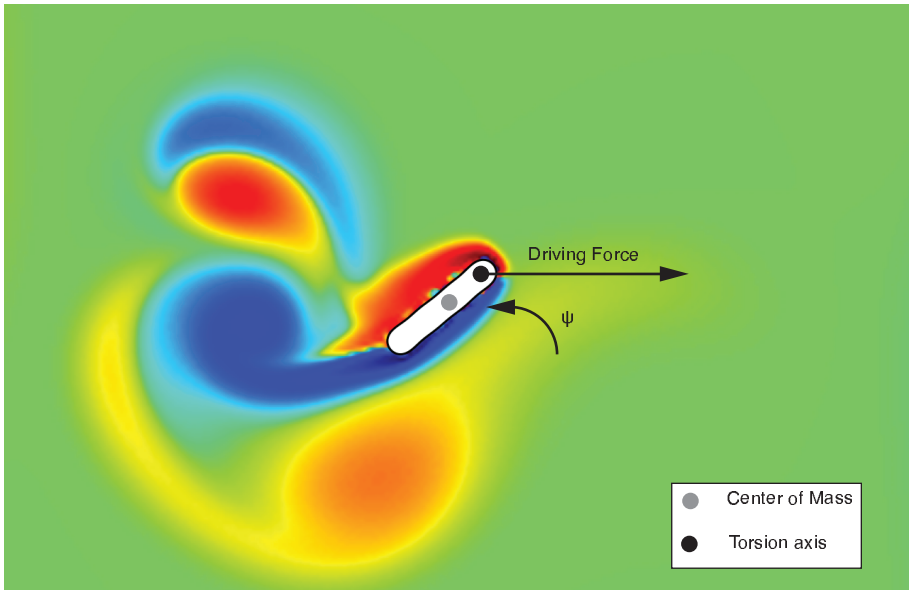

Figure 6.8: We simulate a wing that pitches passively in response to aerodynamic forces. Above we show a snapshot of the vorticity from simulation of a wing being driven at its torsion axis (black circle) at a constant amplitude . The center of mass (gray dot) of the wing is behind the torsion axis. In response to aerodynamic forces and a torsional spring torque acting at the torsion axis, the wing pitches angle (labeled ψ) rocks back and forth periodically like a sheet of paper that is waved back and forth.

is prescribed and ψ is determined by the fluid forces on the wing, the moment of inertia of the wing, the location of the center of mass of the wing (gray circle) and a torque, τ_p, that may act at the torsion axis axis. We model such a wing with IIM, by redefining Eqs. 6.3 and 6.5 to be,

$$\vec{b}(\alpha, t) = \vec{b}_1(\alpha, t) + \vec{b}_2(\alpha, t) + \vec{b}_3(\alpha, t) + \vec{b}_4(\alpha, t), \tag{6.11}$$

where b_1–b_4 are separate singular force components used to enforce the model. In Eq. 6.11, and subsequent equations in this section, we drop the subscript l denoting the particular object for the sake of clarity. All the equations shown, however, apply to the singular forces of each passively pitching wing.

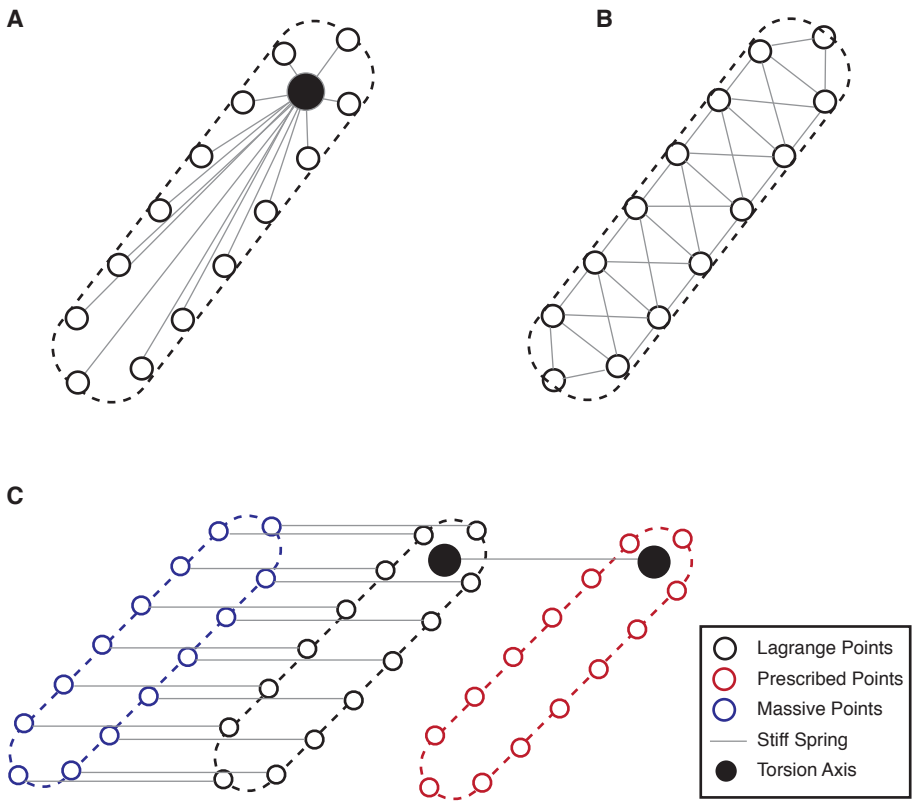

Figure 6.9: (**A**) To ensure the surface follows the torsion axis (black circle), but is allowed to freely rotate around it, we connect each Lagrange point (white circles) to the torsion axis. The rest length of each spring are set as shown above by the grey lines. (**B**) To ensure the surface remains rigid in the flow we prescribe spring interconnections between the Lagrange points as shown by the gray lines above. (**C**) A penalty based method is used to prescribe mass to the shape: by connecting each Lagrange point (white circles) to a massive virtual point (blue circles) with a stiff spring the surface behaves as if it has mass in the flow. Only the position of the torsion axis is connected to the prescribed shape, thus the wing (black dashed line) is allowed to freely rotate in the flow.

We use b_1 to prescribe the position of the torsion axis,

$$\vec{b}_1(\alpha,t) = -\kappa_2\left(\left|\vec{X}(\alpha,t) - \vec{x}_t(t)\right| - R_t(\alpha)\right)\frac{\vec{X}(\alpha,t) - \vec{x}_t(t)}{\left|\vec{X}(\alpha,t) - \vec{x}_t(t)\right|}, \tag{6.12}$$

where $R_t(\alpha)$ is the rest length of the spring connecting a Lagrange point to the torsion axis position $\vec{x}_t(t)$ (Fig. 6.9A). This formula ensures that the position of the surface points remain a fixed distance from the torsion axis, and yet allows them to rotate around the point. Because of this change, the motion of the La-

grange points is no longer fully prescribed (unlike those in Fig. 6.2). Therefore, without additional forces, the wing tends to deform in response to the flow. We use b_2 to ensure that the wing remains rigid,

$$\vec{b}_2(\alpha,t) = \oint_{\delta\Omega} -\kappa_1(\alpha,\alpha')\left(\left|\vec{X}(\alpha,t)-\vec{X}(\alpha',t)\right| - R_s(\alpha,\alpha')\right)\frac{\vec{X}(\alpha,t)-\vec{X}(\alpha',t)}{\left|\vec{X}(\alpha,t)-\vec{X}(\alpha',t)\right|}d\alpha' \quad (6.13)$$

where $R_s(\alpha,\alpha')$ is the rest length of the spring connecting two Lagrange points, and $\kappa_1(\alpha,\alpha')$ defines the pattern of interconnections between Lagrange points. We use the cross-hatched spring pattern shown in Fig. 6.9B to preserve the wing structure during translation.

For a fully prescribed boundary, the inertia of the wing plays no role in its motion and therefore may be ignored in simulations. This is not the case when the pitch of wing is is allowed to respond to the flow. In fact, wing-inertia becomes a dominant factor in the pitching motion of the wing (see [53] and §2). We, therefore, use a penalty based method to simulate a wing with mass [102]. This is implemented by b_3 in our simulations,

$$\vec{b}_3(\alpha,t) = -\kappa_3\left(\vec{X}(\alpha,t)-\vec{X}_m(\alpha,t)\right), \quad (6.14)$$

where $\vec{X}_m(\alpha,t)$ is a surface, whose dynamics are governed by,

$$m(\alpha)\vec{X}(\alpha,t) = -\kappa_3\left(\vec{X}(\alpha,t)-\vec{X}_m(\alpha,t)\right), \quad (6.15)$$

where $m(\alpha)$ is the simulated mass of corresponding the surface point $\vec{X}(\alpha,t)$. We show the result of simulating a surface with mass with this method in Fig. 6.9C: the spring forces from $\vec{X}_m(\alpha,t)$ tend to pull on $\vec{X}(\alpha,t)$ resulting in an effective wing mass,

$$m_w = \oint m(\alpha)d\alpha \quad (6.16)$$

and moment of inertia,

$$I_t = \oint m(\alpha)\left|\vec{X}(\alpha,t)-\vec{x}_t(t)\right|^2 d\alpha \quad (6.17)$$

about the wing torsion axis.

Finally, we also allow for a torque, τ_p, to act at the torsion axis of the wing. This torque is further discussed in §4 and §5. To distribute τ_p to the surface as a singular force, we set,

$$\vec{b}_4 = \hat{z} \times \left(\vec{X}(\alpha, t) - \vec{x}_t(t) \right) \frac{m(\alpha)}{I_t} \tau_p, \tag{6.18}$$

where $\hat{z}$, the vector coming out of the plane, is used to define the perpendicular vector to $\vec{X}(\alpha, t) - \vec{x}_t(t)$. This definition of b_4 produces an equivalent torque to τ_p on the body, with no net force. Furthermore, in a vacuum, this prescription of forces would result in the Lagrange points moving as a rigid body.

The results of simulating a wing with this method are discussed in §4, specifically in Fig. 4.5. Throughout the thesis, the wings are simulated with $\kappa_1 = \kappa_3 = 10^4$ and $\kappa_2 = 10^3$.

6.2.2 EC4 in Elliptical Coordinates

In addition to IIM, we also solve the Navier-Stokes equations using the stream-function vorticity formulation in elliptical coordinates,

$$\begin{aligned} \frac{\partial (S\,\omega)}{\partial t} + \left(\sqrt{S}\,\vec{v} \cdot \nabla \right) \omega &= \frac{1}{Re} \nabla^2 \omega \\ \nabla \cdot \left(\sqrt{S}\,\vec{v} \right) &= 0, \end{aligned} \tag{6.19}$$

where the scaling factor,

$$S(\mu, \theta) = \cosh^2 \mu - \cos^2 \theta \tag{6.20}$$

is determined by the conformal map from Cartesian to elliptical coordinates [9, 93,103]. The details of the numerical method are omitted, as it is commonly used

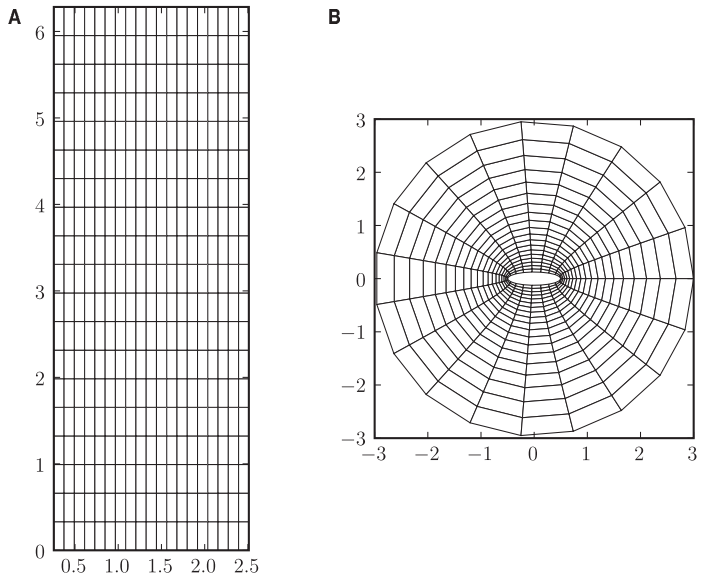

Figure 6.10: (**A**) A Cartesian coordinate system can be mapped to an (**B**) Elliptical coordinate system with the conformal map $x + iy = \cosh(\mu + i\theta)$.

to study flapping flight and is has been described in [9,32,87,103–106]. Here, we focus on the modifications that are made to the method to enable a wing to pitch passively. Unlike, IIM where the wings are represented by body forces acting on the fluid, in EC4 they are actually represented by boundary conditions. As such, we specify the wing motion by directly prescribing $\vec{x}(t)$ and $\psi(t)$, the motion of the wings, and the centroid. We modify the standard algorithm, by allowing $\psi(t)$ and $\vec{x}(t)$ to vary in response to fluid forces. Specifically, as for IIM we prescribe the translational motion of the torsion axis $\vec{x}_t(t)$. Then, in response to inertial and fluid forces the dynamical equation for ψ is,

$$I_t\ddot{\psi} = \tau_a - rF_{y'} + r_{cm}m_w a_{y'} + \tau_p, \tag{6.21}$$

where τ_a is the aerodynamic torque about the wing centroid, r is the distance from the torsion axis to the wing centroid, F'_y is the aerodynamic force perpendicular to the wing, r_{cm} is the distance from the centroid to the center of mass,

$a_{y'}$ is the component acceleration perpendicular to the wing, m_w is the mass of the wing, I_t is the moment of inertia of the wing about the torsion axis and τ_p is some user-defined torque about the torsion axis. The position of the wing centroid may be written in terms of ψ and the prescribed position of the torsion axis,

$$\begin{aligned} x(t) &= x_t(t) - r\cos(\psi) \\ y(t) &= y_t(t) - r\sin(\psi). \end{aligned} \tag{6.22}$$

The boundary conditions on Eq. 6.19 can then be computed at each time-step from Eqs. 6.21 and 6.22. To accomplish this, we discretize Eq. 6.19 using a fourth order spatial stencil, and use explicit Euler for time-stepping [107]. Thus to iterate from the n-th to (n+1)-th time-step,

$$\begin{aligned} \frac{\psi^{(n+1)} - \psi^{(n)}}{\Delta t} &= \omega^{(n)} \\ I_t \frac{\omega^{(n+1)} - \omega^{(n)}}{\Delta t} &= \tau_a^{(n)} - rF_{y'}^{(n)} + r_{cm} m_w a_{y'}^{(n)} + \tau_p^{(n)}, \end{aligned} \tag{6.23}$$

where ω is the angular velocity of the wing, and Δt is the time discretization. Results of simulating a passively pitching wing using the above outlined method can be seen in §4, specifically in Fig. 4.8B.

6.3 Quasi-Steady Models

The high computational cost of determining aerodynamic forces on insect wings using the CFD methods described in §6.2 often prohibit their use to determine the aerodynamic forces on wings for many wing beats. We find that, especially when analyzing free-flight experimental data, simplified models of aerodynamics are necessary to estimate these forces. For this purpose, we use quasi-steady

models based on steady state approximations from air foil theory. These models average over the details in the airflow around insect wings to estimate the aerodynamic forces using only the wings instantaneous velocity, acceleration and orientation. Because of this simple dependence on the wing kinematics, such models significantly reduce computational costs. In addition, measurement uncertainties in the wing kinematics can be easily estimated on the forces computed using these aerodynamic models (see §6.3.3). In fact, we find that the measurement errors inherent in experimental kinematics can nullify the benefit of added accuracy from CFD models.

Using quasi-steady models to understand the aerodynamics of insect flight has been an intensely researched topic [12, 14, 108–110]. Early attempts at applying steady state theory directly, met with mixed success: although the aerodynamic properties of steady state airfoils matched those observed for animals in fast forwards flight [108], researchers found that, to sustain hovering flight, insect wings needed unreasonably high lift coefficients [14]. It was later found, however that the high lift coefficients can be explained by the presence of a strong attached leading edge vortex in flapping flight [35, 91]. Once this effect is incorporated into quasi-steady models, the average vertical forces predicted by such models are in closer agreement with measurements. However, only modeling the translational circulation due to the attached vortex fail to predict the time trace of forces on a flapping wing. This is because the effects of wing rotational were unaccounted for [70]. Researchers showed that wing rotation results in and increased circulation around a wing due to the attached fluid [87, 111]. When these rotational, and translational added mass effects of the attached fluid are taken into account the time course of forces can be predicted with a quasi-steady model [15, 87, 93, 112–114].

In this chapter, we detail the quasi-steady methods we employ throughout this thesis. In §6.3.1 we describe a two-dimensional quasi-steady model which predicts aerodynamic forces on a rotating and translating blade. In §6.3.2 we show how we extend this quasi-steady model using propeller theory to estimate the aerodynamic forces on a flapping wing.

6.3.1 Falling Paper Model

The specific two-dimensional quasi-steady model we use throughout the thesis is the force model developed to study fluttering and tumbling plates in fluids [36, 87, 115]. Due to the similarity in the Reynolds number regime of these phenomena, these models are quantitatively similar to those used to study insect flight [15] and have been successfully applied to modeling the forces on insects [26, 42, 53, 93]. We briefly review the method and compare it to simulations using IIM in this section.

To compute the aerodynamic forces, $\vec{F}$, and torque (about the centroid), τ, on a wing with chord length $2c$, and thickness $2b$ (Fig. 6.11) we use,

$$\begin{aligned} F_{x'} &= -m_{11}\dot{v}_{x'} + m_{22}\dot{\psi}v_{y'} - \rho_f \Gamma v_{y'} - F^{\nu}_{x'} \\ F_{y'} &= -m_{22}\dot{v}_{y'} - m_{11}\dot{\psi}v_{x'} + \rho_f \Gamma v_{x'} - F^{\nu}_{y'} \\ \tau &= -I_a\ddot{\psi} + (m_{11} - m_{22})v_{x'}v_{y'} - \tau^{\nu}, \end{aligned} \tag{6.24}$$

where $v_{x'}$ and $v_{y'}$ are the wings velocity components, Γ is a model of the circulation around the wing, and $\vec{F}^{\nu}$, τ^{ν} respectively model the viscous force and torque on the wing. The added mass coefficients - $m_{11} = \pi\rho_f b^2$, $m_{22} = \pi\rho_f a^2$, and $I_a = \frac{1}{8}\pi\rho_f(a^2 - b^2)$ - model the added inertia caused by attached fluid to an accelerating wing. Their particular values are determined from inviscid theory [116].

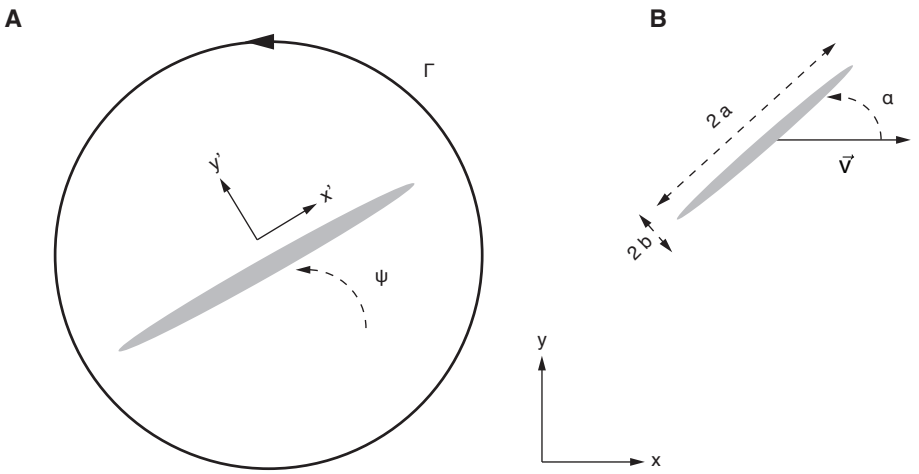

Figure 6.11: (**A**) A two dimensional wing that translates and rotates. The circulation around the wing is represented by Γ. The angle ψ is the orientation of the wing to the lab frame coordinate system x- and y-. The primed coordinate system is instantaneously co-rotating with the wing's velocity vector. (**B**) We model a wing with chord length $2a$ and thickness $2b$. The angle of attack, α of a wing is the angle between the chord of the wing $\hat{c}$ and its velocity vector relative to the lab frame.

The angle ψ is the orientation of the wing to the lab frame (unprimed coordinate system). The primed coordinate system is co-rotating with the wing (Fig. 6.11).

To model the circulation around the wing,

$$\Gamma = -C_T a v \sin 2\alpha + 2C_R a^2 \dot{\psi}, \tag{6.25}$$

where the term multiplied by dimensionless constant C_T models the translational circulation around the wing including the unsteady effects due to delayed stall. The term multiplied by dimensionless constant C_R models the added circulation due to wing rotation. The angle of attack $\alpha \equiv \tan^{-1}(v_{y'}, v_{x'})$ is the angle between the wings chord and its velocity vector. We model vicious drag, $\vec{F}^{\nu}$, and the viscous torque, τ^{ν}, as

$$\vec{F}^{\nu} = \rho_f a \left(C_D(0) \cos^2 \alpha + C_D(\pi/2) \sin^2 \alpha \right) v \vec{v}' \tag{6.26}$$

$$\tau^{\nu} = \pi \rho_f a^4 \left(f\mu_1 + \mu_2 \left| \dot{\psi} \right| \right) \dot{\psi}, \tag{6.27}$$

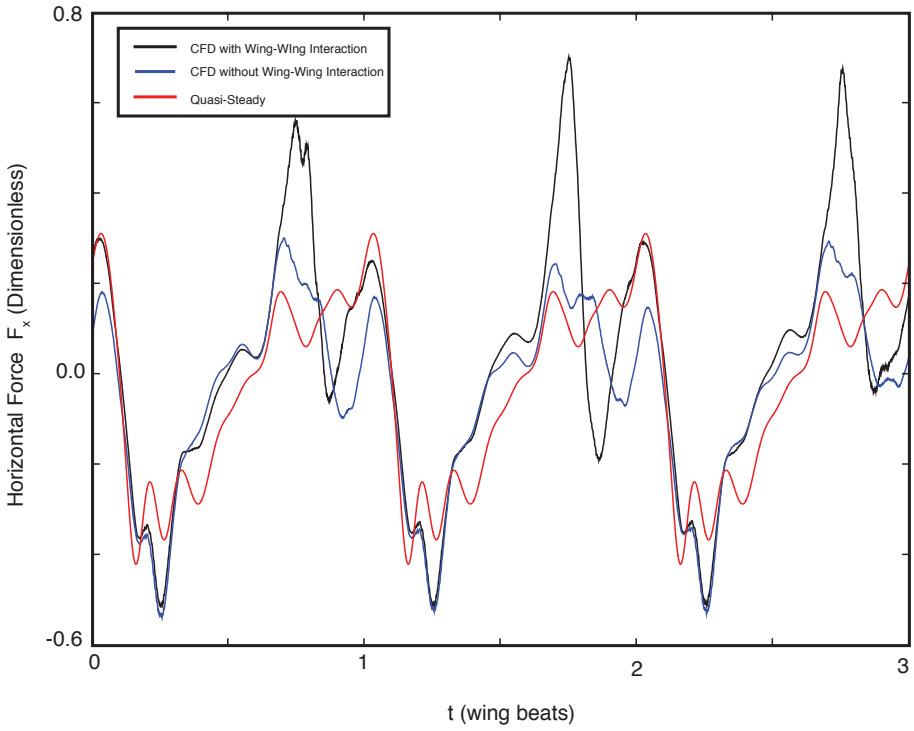

Figure 6.12: We compare the horizontal force predicted by the quasi-steady model to CFD simulations using IIM for the dragonfly wing kinematics described in §2. We show the horizontal force due to motion of the hindwing: in red are results predicted by the quasi-steady model, in black we show simulations from IIM where both the fore- and hindwings are simulated, in blue we show the results of simulating only the hindwing with IIM. Quantities are shown in dimensionless form, with the dimensions of time being beats, and force being the weight of the dragonfly.

where f is the wing beat frequency and the dimensionless constants $C_D(0)$, $C_D(\pi/2)$, μ_1 and μ_2 are Reynolds number dependent properties of the flapping wings.

Comparison to Immersed Interface Method

Past research indicates that the quasi-steady model can quantitatively predict the aerodynamic forces on a two-dimensional flapping wing [15, 87, 93]. These results analyze the applicability of these models to wings that flap in a horizon-

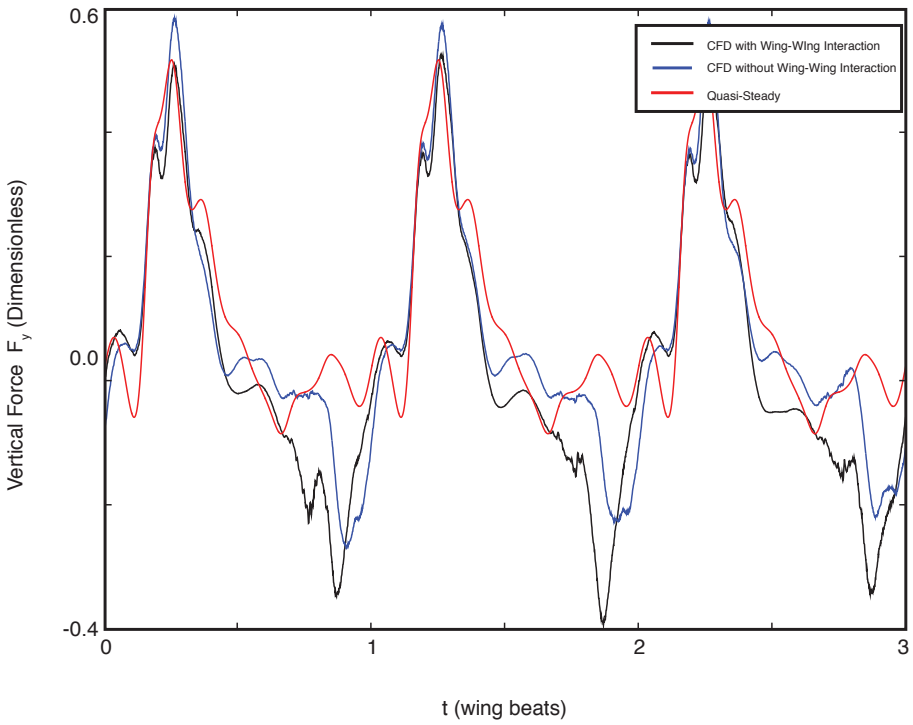

Figure 6.13: We compare the vertical force predicted by the quasi-steady model to CFD simulations using IIM for the dragonfly wing kinematics described in §2. We show the vertical force due to motion of the hindwing: in red are results predicted by the quasi-steady model, in black we show simulations from IIM where both the fore- and hindwings are simulated, in blue we show the results of simulating only the hindwing with IIM. Quantities are shown in dimensionless form, with the dimensions of time being beats, and force being the weight of the dragonfly.

tal stroke plane such as the wings of a fruit fly. Here, we analyze the results of applying the quasi-steady model to dragonfly wing kinematics (see §2). Dragonflies flap using an inclined stroke plane, and have two wings flapping on each side. We, therefore, focus on how the interaction between the two flapping wings and the inclined stroke plane affects the force calculations and assess the quality of quasi-steady model predictions in this context. For all simulations quasi-steady parameter values match those in [36].

In Figs. 6.12–6.14 we compare $\vec{F}$ and τ predicted by the quasi-steady model

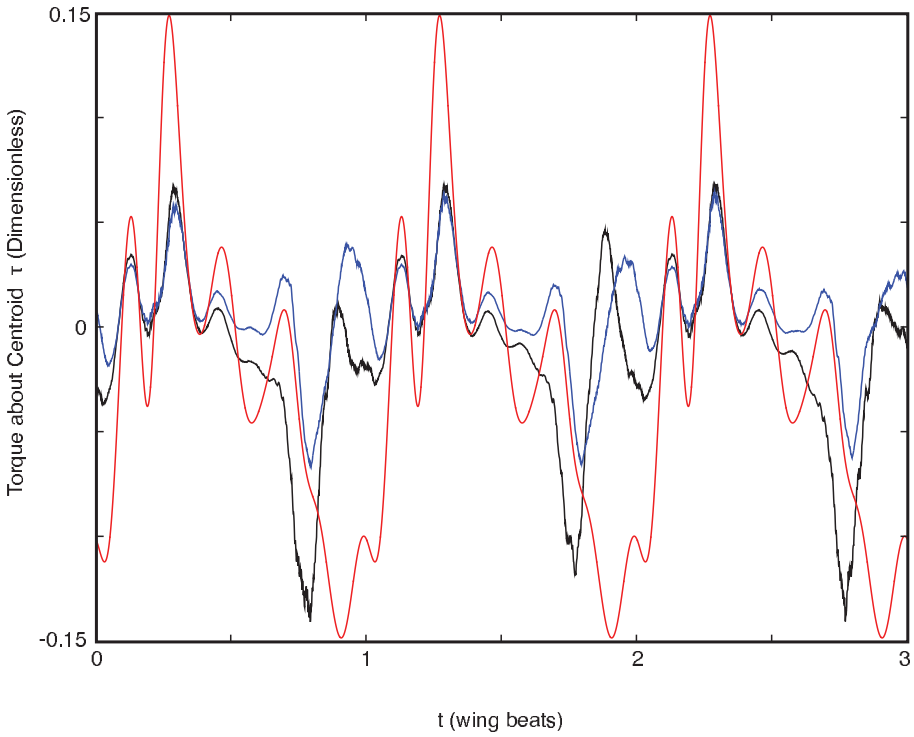

Figure 6.14: We compare the torque about the wing centroid, τ, predicted by the quasi-steady model to CFD simulations using IIM for the dragonfly wing kinematics described in §2. We show τ due to the motion of the hindwing: in red are results predicted by the quasi-steady model, in black we show simulations from IIM where both the fore- and hindwings are simulated, in blue we show the results of simulating only the hindwing with IIM. Quantities are shown in dimensionless form, with the dimensions of time being beats, and force being the weight of the dragonfly.

(red lines) to simulations of dragonfly wing kinematics using IIM (black and blue lines). All results are shown for the hindwing of the dragonfly because the down-wash from the forewing tends to exaggerate wing-wing interaction effects. To separately isolate the effects of wing-wing interaction and the effect of the inclined stroke plane, we show results of simulating the motion of both the fore- and hindwings (black line) and the hindwing alone (blue line) using IIM.

Comparing quasi-steady model predictions of $\vec{F}$ to simulations including

wing interaction effects, we find that the general trend of forces is predicted by the quasi-steady model, however, significant discrepancies exist. The most significant difference is that the large peaks in F_x (Fig. 6.12), and the large dips in F_y (Fig. 6.13), are missed by the quasi-steady model. Consequently, the model under-predicts the average F_x and over-predicts the average F_y. The missed peaks coincide with the hindwing crossing the jet ejected by the fore-wing in Fig. 6.3E–F. Including this downdraft in the quasi-steady model has the effect of reducing F_y while increasing F_x as observed in IIM simulations. The effect of this jet is further underscored by the simulations of the isolated hindwing where the discrepant peaks are significantly reduced (blue lines in Figs. 6.12 and 6.13).

Quasi-steady model predictions of $\vec{F}$ match simulations of the isolated hindwing more closely than when wing interaction effects are included. The discrepancies that exist are largely because the inclined stroke plane of the dragonfly hindwing causes the wing to interact with the net down-wash of its flapping motion [26]. This interaction results in a slight over-prediction of F_y and slight under-prediction of F_x by the quasi-steady model.

In Fig. 6.14 we compare τ as predicted by the quasi-steady model to both simulations of the hindwing motion with wing interaction effects and simulations of the isolated hindwing motion. We find that the quasi-steady torque model captures the general trend of τ, however, significant discrepancies exist. Insect wings, however, are driven by flight muscles through the torsion axis which acts near the leading edge of the wings [19,28]. Because the torque about the torsion axis from aerodynamic forces, $rF_{y'}$, is much larger than the torque about the wing centroid, τ plays only a minor role in insect wing kinematics and these discrepancies no not affect the results of this thesis. In §7, however,

we introduce a genetic programming method that may, in the future, improve the quality of the quasi-steady torque model.

6.3.2 Flapping Wing Model

In this section, we extend the two-dimensional quasi-steady model described in §6.3.1 to estimate the aerodynamic forces on a three dimensional flapping wing. When non-dimensional constants are experimentally determined such quasi-steady models can accurately predict the aerodynamic forces on a robotic wing that is a scaled to match the Reynolds number regime of flying insects [15].

We proceed by deriving the spatial (6-component) velocity of the insect wings and body in terms of the position and orientation parameters described in §3.2. We consider two different frames, the lab frame and the wing or body fixed frame, where the coordinate system is oriented along the axes of the body. As derived in [45], for Euler angles, ϕ, θ and ψ the angular velocity in the wing-fixed frame is,

$$\vec{\omega}_{\text{fixed}} = \begin{pmatrix} \dot{\phi}\sin\theta + \dot{\psi} \\ \dot{\phi}\cos\theta\sin\psi - \dot{\theta}\cos\psi \\ \dot{\theta}\sin\psi + \dot{\phi}\cos\theta\cos\psi \end{pmatrix}, \tag{6.28}$$

and similarly in the lab frame,

$$\vec{\omega}_{\text{lab}} = \begin{pmatrix} \dot{\theta}\sin\phi + \dot{\psi}\cos\theta\cos\phi \\ \dot{\psi}\cos\theta\sin\phi - \dot{\theta}\cos\phi \\ \dot{\phi} + \dot{\psi}\sin\theta \end{pmatrix}. \tag{6.29}$$

It follows that a point attached to the wing moves with velocity,

$$\vec{v} = \dot{\vec{x}}_c + \vec{\Omega} \times \vec{r}, \tag{6.30}$$

where $\dot{\vec{x}}_c$ is the velocity of the centroid, and $\vec{r}$ is the vector from the wing centroid to the point. Henceforth, we refer to wing-fixed coordinates as primed and lab frame coordinates as unprimed.

The span-wise flow along the wing is smaller than in the other two directions; therefore, as in [15, 42, 53], we use a blade element model oriented along the span of the wing to compute all components of aerodynamic force, except for the added mass. The force, $d\vec{F}(r)$, and torque, $d\vec{\tau}(r)$, on a particular blade element, located r away from the centroid along the span of the wing, can then be computed from,

$$\begin{aligned} d\vec{F}_{\text{fixed}} &= \begin{pmatrix} 0 \\ -\rho_f \Gamma(r) v_{z'} - F^{v}_{y'}(r) \\ \rho_f \Gamma(r) v_{y'} - F^{v}_{z'}(r) \end{pmatrix} \\ d\vec{\tau}_{\text{fixed}} &= \begin{pmatrix} -\frac{\pi \rho_f c(r)^4}{16} \left(\frac{\mu_1}{T} + \mu_2 \left| \Omega_{x'} \right| \right) \Omega_{x'} \\ 0 \\ 0 \end{pmatrix}. \end{aligned} \tag{6.31}$$

where ρ_f is the density of air, μ_1 and μ_2 are dimensionless constants and T is the inverse of flapping frequency. The remaining terms Γ and $\vec{F}^{v}$ model circulation and viscous drag terms, respectively. They can be computed from

$$\begin{aligned} \Gamma &= -C_T c(r) \frac{v_{y'} v_{z'}}{\sqrt{v_{y'}^2 + v_{z'}^2}} + \frac{1}{2} C_R \Omega_{x'} c(r)^2 \\ \vec{F}^{v} &= \frac{\rho_f c(r) \vec{v}}{2 \sqrt{v_{y'}^2 + v_{z'}^2}} \left(C_D(0) v_{y'}^2 + C_D(\pi/2) v_{z'}^2 \right), \end{aligned} \tag{6.32}$$

where C_T, C_R, $C_D(0)$ and $C_D(\pi/2)$ are the dimensionless constants described in [36,42,53] and $c(r)$ is the cross-sectional chord length of the wing model. The six aerodynamic spatial force components about the wing centroid can be found by

integrating along the span,

$$\begin{aligned} \vec{F} &= \int_{-a}^{a} d\vec{F} \\ \vec{\tau} &= \int_{-a}^{a} \left(\vec{r} \times d\vec{F} + d\vec{\tau} \right). \end{aligned} \tag{6.33}$$

As mentioned, the above derivation neglects added mass terms. This is done because these terms depend on the wing acceleration and therefore span-wise components may be significant due to centripetal accelerations. As a result, we use the full 3D form the added mass components of the fluid force. In the wing-fixed frame, we can write the added mass spatial force, $\vec{F}^{\text{am}}$ and $\vec{\tau}^{\text{am}}$, using Einstein-summation notation as

$$\begin{aligned} F_j^{\text{am}} &= -m_{ij}\dot{v}_i - \epsilon_{jkl} m_{li} v_i \Omega_k \\ \tau_j^{\text{am}} &= -\dot{v}_i m_{j+3,i} - \epsilon_{jkl} v_i \Omega_k m_{l+3,i} - \epsilon_{jkl} v_k v_i m_{li}, \end{aligned} \tag{6.34}$$

where m_{ij} is the 6×6 added mass tensor, v_i is the object velocity, and $\dot{v}_i$ is the acceleration relative to the wing-fixed frame [117, 118]. In Eq. 6.34 summations over repeated indexes are carried out such that $i = 1, 2, 3, 4, 5, 6$ and $j, k, l = 1, 2, 3$. Then v_1, v_2 and v_3 correspond to $v_{x'}$, $v_{y'}$ and $v_{z'}$, while v_4, v_5 and v_6 refer to $\Omega_{x'}$, $\Omega_{y'}$ and $\Omega_{z'}$, respectively.

For an elliptic disc, the added mass tensor, $m_{ii'}$, in the wing-fixed coordinate

system is diagonal. Components along its diagonal are

$$\begin{aligned} m_{11} &= m_{22} = 0 \\ m_{33} &= \frac{4\pi\rho_f ab^2}{3E(k)} \\ m_{44} &= \frac{4\pi\rho_f}{15}\frac{ab^4\left(a^2-b^2\right)}{\left(2a^2-b^2\right)E(k)-b^2K(k)} \\ m_{55} &= \frac{4\pi\rho_f}{15}\frac{a^3b^2\left(a^2-b^2\right)}{\left(a^2-2b^2\right)E(k)+b^2K(k)} \\ m_{66} &= 0, \end{aligned} \tag{6.35}$$

where $K(k)$ and $E(k)$ are the (complete) elliptic integrals of the first and second kind, while $k = \sqrt{1-\left(\frac{b}{a}\right)^2}$ is the elliptic modulus [72]. The total spatial force on the insect wing about the centroid is then,

$$\begin{aligned} \vec{F}^{\text{aero}} &= \vec{F}^{\text{am}} + \vec{F} \\ \vec{\tau}^{\text{aero}} &= \vec{\tau}^{\text{am}} + \vec{\tau}. \end{aligned} \tag{6.36}$$

Throughout this thesis, the quasi-steady model parameters - $C_T = 1.833$, $C_D(0) = 0.21$, $C_D(\pi/2) = 3.35$, $C_R = 1.5$ - are set to the experimental values, measured using a scaled mechanical model of a fruit fly wing [119]. No measurements are available for the dissipative torque parameters therefore, we use, $\mu_1 = 0.2$ and $\mu_2 = 0.2$, the values from [105].

Validation with Body Forces

To test the flapping wing model using only experimental data, we follow the suggestion in [14], and examine how closely the aerodynamic forces predicted from wing kinematics match the motion of freely flying *Drosophila melanogaster*. For an ideal model, combining measurements of the free-flight kinematics of an

insect with simulation of forces should yield,

$$M_b\vec{a} = \vec{F}_l^{(a)} + \vec{F}_r^{(a)} - M_b g\hat{z}, \tag{6.37}$$

where M_b and $\vec{a}$ are the mass and acceleration of the insect, g is the acceleration of gravity, and $\vec{F}_l^{(a)}$ and $\vec{F}_r^{(a)}$ are the aerodynamic forces on the left and right wings, respectively. By measuring the morphology and free-flight kinematics of a fruit fly, then simulating aerodynamic forces, we can compare how well the left and right side of Eq. 6.37 match to determine the quality of the aerodynamic model. This method, however, stresses measurement capabilities as much as it does the aerodynamic model (see §3). Specifically, there are two experimental complications. The first, is that the mass of *Drosophila* can vary significantly (by as much as 30-35%) between individuals. In fact, even within the same individual, from the beginning of flight to the end of flight lasting only a few minutes we find that the mass of a fly can vary by 10%. Therefore, to test model accuracy to better than 30%, insects must be individually weighed and placed in the flight chamber alone (see §3). This tedious procedure severely restricts the number of flight sequences that can be measured and, to date, we only have two that we can compare. In addition, the fruit flies generally move very little on a stroke to stroke basis. Therefore, the error bars on body accelerations (see §3.8.1), and consequently the left side of Eq. 6.37, are very large compared to the wing beat to wing beat variation in aerodynamic forces. Therefore, currently, we can only compare time averaged values the left and right sides of Eq. 6.37 for an entire time-sequence.

In Tbl. 6.1, we compare the inferred and computed forces for a 33 wing beat flight sequence. In this sequence the fly moves very little so we refer to this flight sequence as "hovering". In Tbl. 6.2, we compare the inferred and computed forces for a 17 wing beat flight sequence for a fly that travels in the $y-$

Table 6.1: Comparison of time-averaged forces on the fruit fly as measured by experiment, and using the flapping wing model. Averages are over 33 wing beats of a freely-flying *D. melanogaster*. The difference in force predictions should be compared to the body weight of the fruit fly which is 6.9 ± 0.3 μN. The flight sequence corresponding to this calculation is shown in Fig. 4.1.

Force (μN)	Experimental	Model
F_x	0.9±0.3	0.3±0.1
F_y	-0.2±0.2	-0.2±0.1
F_z	6.6±0.3	5.8±0.2

Table 6.2: Comparison of time-averaged forces on the body as computed directly from the body kinematics (Experimental) and using a quasi-steady force model (Model). Averages are taken over 17 wing beats of a freely flying *D. melanogaster*. The difference in force predictions should be compared to the body weight of the fruit fly which is 11 ± 2 μN. The flight sequence corresponding to this calculation is shown in Fig. 5.5

Force (μN)	Experimental	Model
F_x	-0.7±0.7	-1.6±0.1
F_y	1.1±0.7	2.5±0.1
F_z	11.6±2.1	12.1±0.6

direction across the filming volume. For both sequences, although the magnitude of forces can differ, they only do so by about two standard error bars, the direction is correctly predicted.

6.3.3 Estimating Uncertainties on Forces and Torques

The quasi-steady models detailed in §6.3 allow for easy propagation of measurement uncertainties on computed aerodynamic quantities. For experimental data where the uncertainty in measured parameters can be estimated (see §3.6) with a quasi-steady model the uncertainties can be propagated using Taylor series uncertainty propagation [120]. For example, for a computed force component, F, (e.g. quasi-steady force) that is a function of the time-series of kinematic mea-

surements of the fly, y_i. We propagate the measurement uncertainties on y_i to F by adding errors in quadrature,

$$\sigma_F^2 = \sum_i \left(\frac{\partial F}{\partial y_i} \sigma_{y_i} \right)^2 . \tag{6.38}$$

Computing uncertainties in F in this way corresponds to the assumption that errors in y_i are uncorrelated and approximately Gaussian. This is a reasonable approximation for our positional errors [25]. We use this technique to estimate all uncertainties on computed quantities in §4 and §5.

Although techniques exist to estimate uncertainties on computed forces using CFD simulations [121], such methods are computationally intensive for our problems.

CHAPTER 7

A GENETIC PROGRAMMING METHOD TO IMPROVE THE FALLING PAPER MODEL

7.1 Introduction

In this chapter, we discuss a topic somewhat disjoint from the rest of the thesis. Despite this, we believe that the topic is of interest and therefore worth discussing. Here, we apply Genetic algorithms to scientific discovery. Genetic algorithms are extremely versatile optimization methods [122]. They are particularly useful when no specific method exists to solve a problem. As such, they have been applied to countless scientific problems, including understanding optimality in nature [42], engineering design, and even scientific discovery. Here, we develop a method that can "discover" the equations of motion behind a certain process. The application of genetic algorithms to such symbolic regression problems is called genetic programming.

We specifically develop this method for improving a class of models with which the aerodynamic forces on a two-dimensional flapping plate can be computed. The physical laws behind these forces are known. Specifically, the Navier-Stokes equations describe the flow of an incompressible fluid [123]. These partial differential equations,

$$\begin{aligned} \frac{\partial \vec{v}}{\partial t} + \vec{v} \cdot \nabla \cdot (\vec{v}) &= -\nabla p + \frac{1}{Re} \Delta \vec{v} \\ \nabla \cdot \vec{v} &= 0, \end{aligned} \tag{7.1}$$

describe the evolution of a fluid volume's velocity, $\vec{v}$, and pressure fields, p when given appropriate boundary conditions and flow regime specified by Re. Thus,

the forces on a flapping plate can be computed from $\vec{v}$ and p. These equations, however, are nonlinear and, in general, require the solution of the entire flow field to compute forces. Therefore, they are computationally expensive to solve. For many classes of problems direct solution of Eq. 7.1 is not feasible. As such, there is a demand for reduced order models that accurately capture the underlying physics without the need for solving the full equations.

The falling paper model (FPM) can predict the forces and torque acting on a two-dimensional flapping plate when $10 \leq Re \leq 5000$ ([87] and see also §6.3.1). This quasi-steady model coarse grains over the fluid flow, to make these predictions using only a wing's instantaneous kinematics. Applying this model to predicting the dynamics of a wing, e.g. a plate falling under the influence of aerodynamics and gravity, requires the solution of a set of ordinary differential equations. This is in contrast with Eq. 7.1, where the already difficult solution of partial differential equations is exacerbated by time-dependent boundary conditions that are coupled to the flow. Due to their simplicity, FPM and other similar models are applied to the solution of many problems. Of particular interest to us, is the common use of FPM to extract the aerodynamic forces on, and to understand the dynamics of, the wings of flapping insects [42, 53]. Thus, improving its accuracy is an important goal.

We find that the aerodynamic forces on a flapping wing are well modeled by FPM (see §6.3.1 and [42, 53, 87, 103, 105]). The torque about the wing's centroid, however, is not well-understood (see Fig. 6.12 and [103]). Consequently, we seek to improve its current state. Because asymptotic expressions for this torque cannot be derived from Eq. 7.1, we develop a genetic programming method to discover an improved model of the torques about a wing's centroid. In effect,

we introduce a method to "data mine" for a reduced order model whose predictions agree with those of the Navier-Stokes equations.

7.2 Methods

The set of equations that comprise the Falling Paper Model are described in §6.3.1. Here, we focus on developing a method to discover an approximate symbolic equation for the torque about a wing's centroid, τ. To determine a model for τ, we first compute target torques, τ_0, that we try to match. For testing of the method, we generate τ_0 using a known function. We then apply the method to determine an improved torque model, by generating τ_0 using direct solutions of Eq. 7.1 for several motions of a flapping wing. We use the Immersed Interface Method (see [124] and see also §6.2.1) to measure τ_0 for these flapping wings.

In accord with quasi-steady models of fluid flow, we seek a model of τ of the form,

$$\tau = \tau(\theta, \dot{\theta}, \theta, u, v), \tag{7.2}$$

where θ is the orientation of the wing in the flow and u, v, and $\dot{\theta}$ are the velocities of the wing centroid and angular velocity of the wing, respectively. Because an accelerating wing may have fluid attached to it during its motion, in general τ can also also depend on $\dot{u}$, $\dot{v}$, and $\ddot{\theta}$. We do not allow for these terms, because in this case, the genetic programming method will trivially rediscover Newton's laws of motion $\tau = I\ddot{\theta}$ and $\vec{F} = m\dot{\vec{v}}$. To account for the attached fluid, we use analytical expressions for the added moment of inertia, I_a, to modify τ_0 [116, 117]. Thus, we find,

$$\tau_0 - I\ddot{\theta} = (1 + \frac{I_a}{I})\tau_0 \approx \tau(\theta, \dot{\theta}, u, v). \tag{7.3}$$

7.2.1 Representation and Genetic Operators

We use a tree representation of genetic programs where operators are represented as nodes in the tree and variables and constants are represented as leaves. The implemented operators are $\sin x$, $\cos x$, $|x|$, $x \cdot y$, $\frac{x}{y}$, $x + y$, $x - y$, $\log x$, x^y and $\sqrt{x}$. The operators are implemented so as to make them easily extensible. Initially there were two types of leaf nodes, constants and variables, however it was found to be useful to limit the number of constants that the genetic algorithm can use, and therefore constants were also represented as variables, with a single value for all runs.

Crossover between two trees is implemented by swapping two random subtrees between them [125]. We use three types of mutation operators: structural mutation, hill-climbing, and local-optimization. Structural mutation corresponds crossing over an individual from the population with a random expression tree. Hill-climbing mutation replaces a constant in the expression tree of an individual from the population, with a random value of standard deviation 0.1 centered around the original constants value. We found that with only hill-climbing mutation, the constants converge very slowly towards desired values. Therefore, we use the local-optimization mutation to perform a Nelder-Mead simplex search for the local optimum of a particular constant in an individual expression trees. To prevent over-fitting, the pool of points used for local-optimization is independent of the pool used for training and testing. The use of this technique dramatically improved results.

We compare two different cost functions in this method: the average sum of square errors between the target and model torque (sse), and the squared-correlation coefficient (r^2). We show that the latter produces more accurate mod-

els when used on simulated data.

7.2.2 Genetic Algorithm

Using a standard genetic algorithm to solve the regression problem leads to bloated expressions [122]. Consequently, as simulated generations progress, the expression trees become increasingly complex and eventually unreadable. Because we are seeking a simple quasi-steady model, we require that the expression trees remain small and human readable. We compare two methods to accomplish this: parsimony pressure methods, and multi-objective methods [126, 127].

Bloat control methods that using parsimony pressure modify the cost function with a pressure term that tends to reduce population size [122, 126]. We find that constant and two-tier parsimony pressures both can produce succinct models that are accurate on simulated data. However, we find that the quality of results from both of these methods is highly sensitive to their parameter values. Therefore, when no a-priori knowledge of the solution is available, finding correct values for these parameters is not feasible.

To reduce bloat, multi-objective methods optimize, not only the quality of fit of an expression, but also the size of the expression tree [128,129]. Consequently, the genetic programming method, produces a Pareto set of optimal solutions. The user must choose the solution that has the best trade-off between size and correctness. In practice, we find that the NSGA-II multi-objective optimization method works well for this symbolic regression problem [130]. We, however, find that because small expression trees are easy to produce (i.e. crossover be-

tween two small threes invariably leads to small trees), the population quickly fills with homogeneous small models [131]. Therefore, we must enforce population diversity artificially.

To maintain diversity, we modify the crossover operator in the genetic algorithm. Instead of choosing the crossover node randomly from the expression trees, we choose an internal node with 90% probability [125]. This prevents crossover from generating many small trees. We also modify the ranking of optima in NSGA-II, to ensure that solutions dominate themselves. This small change ensures that multiple identical trees are not all considered equally fit, but one is chosen as the true optima. We find that while these methods suffice to maintain diversity an additional increase in convergence speed by maintaining a small pool of individuals that evolve separately [132]. The two pools are combined every 50 generations, and the small pool regenerated with random individuals.

The full training sets used for symbolic regression ranged between 1000–10000 target torque values with corresponding values for u, v, θ and $\dot{\theta}$. To improve convergence, generalization performance and speed-up the evaluation of the fitness function, we co-evolve a subset of the training set that we use as the target values in symbolic regression [133]. We find that using a predator-prey model to co-evolve these subsets produces good results on training data, but fails on the real torque values. This is because for these values, it becomes too easy to evolve subset pools where symbolic regression can make no progress. Therefore, we use how well the fitness on the whole dataset is approximated by the subset for a set of randomly chosen individuals from the symbolic regression set as the fitness function for the co-evolving subsets. This fitness function,

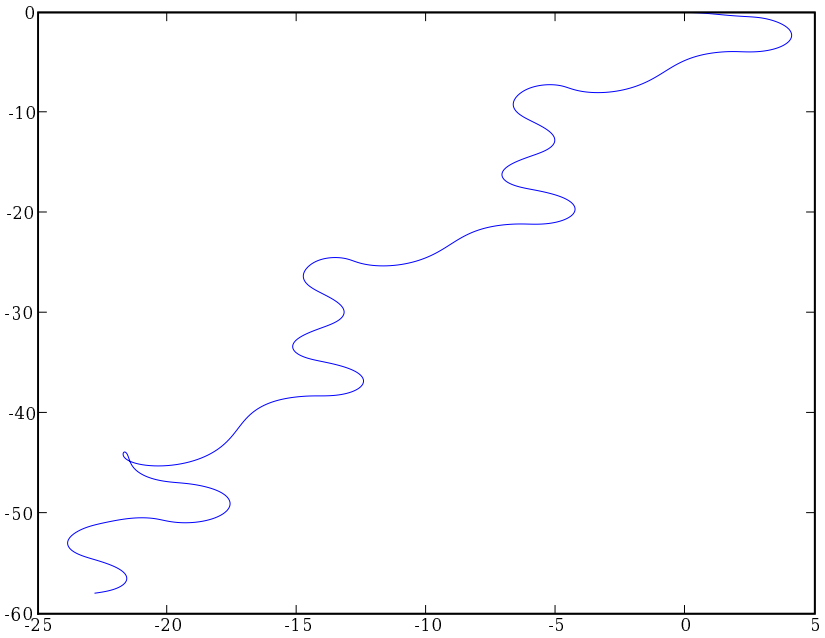

Figure 7.1: Motion trace of data generated using original falling paper model.

though costly to evaluate, produces faster and higher quality results than evaluating the fitness of the expression trees on the entire training set.

7.3 Results and Discussion

7.3.1 Generated Data

To test the symbolic regression method in §7.2.2, we use the unmodified falling paper model to generate a series of trajectories of a freely falling paper under the influence of gravity. We find that the particulars of the trajectory are unimportant as long as it contains sufficient distinct states of the falling plates. We, therefore, use the trajectory shown in Fig. 7.1 in our analysis. This trajectory

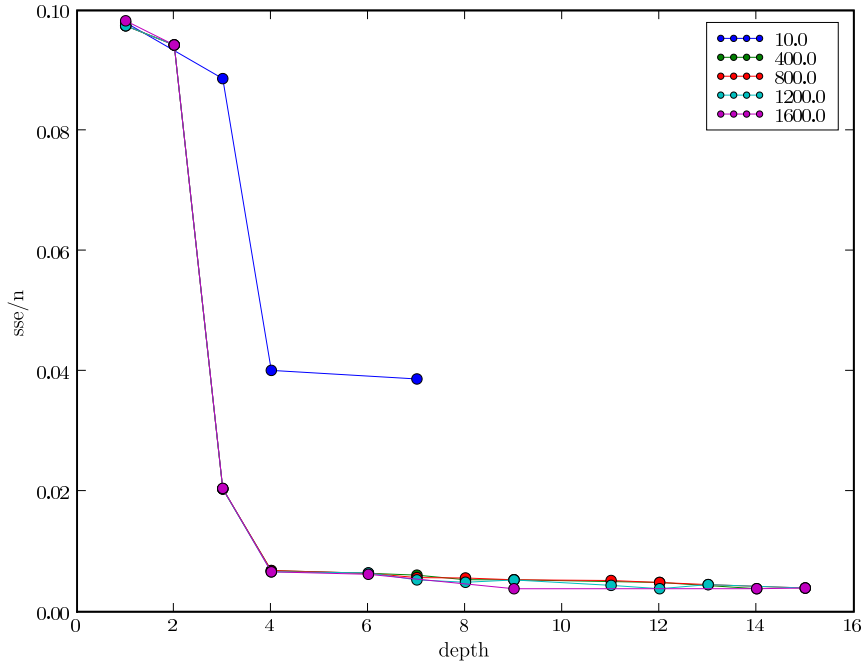

Figure 7.2: Pareto front for the sum of squared errors versus the depth of the expression tree. Note that good solutions are minimized under both axes.

corresponds to 1000 distinct u, v, θ and $\dot{\theta}$ points. We also modify the torque model in FPM, to see how well models of varying complexity are recovered by the GA. For brevity, we show the results of applying it to,

$$\tau_0 = -uv - (0.2 + 0.2\,|\omega|)\omega, \tag{7.4}$$

and find similar results for other models. To compare fitness functions, we apply the symbolic regression program using both sse and r^2 to this dataset.

We show the Pareto optimal front of sse and depth for the symbolic regression in Fig. 7.2. The results are shown after iterations 10, 400, 800, 1200 and finally 1600. After the 10th iteration little learning takes place. Once the population has converged to the optimal front, we see that the sse of the expressions have a large jump from expressions of depth 2 to expressions of depth 4. Past

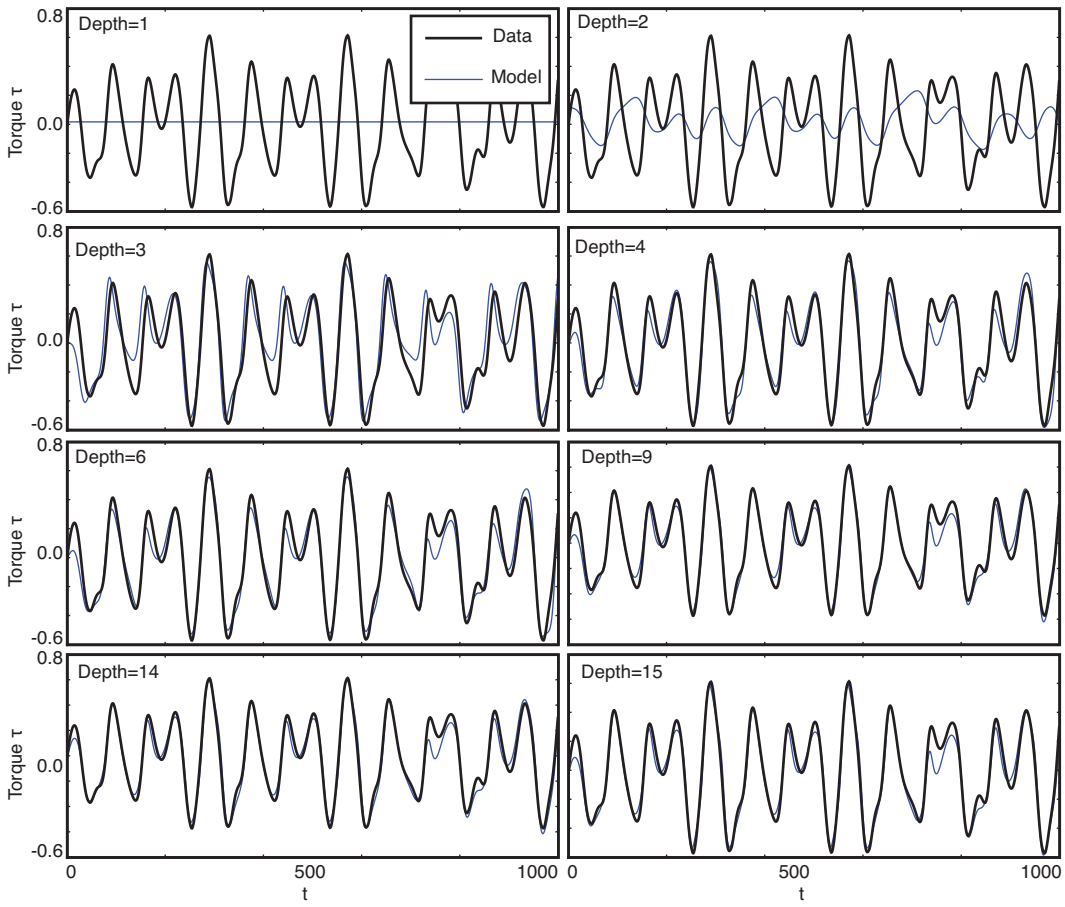

Figure 7.3: Time trace of torque for the generated data from a simulated run of falling paper model and as predicted by various depths of converged of symbolic regression trees. Sum of squared errors are used as the cost function of the optimization.

this point, diminishing returns can be seen in the addition of additional tree levels.

We show the time traces of torque, τ^{ν}, as generated by the falling paper model, and as predicted by the symbolic regression. Expression trees of varying depths are compared from the converged Pareto front. As above, it is apparent that the depth of four nodes expression makes predictions that are very close to the generated data. Adding additional depths to the tree produces only negligible improvement in the approximation. The equation predicted by the tree of

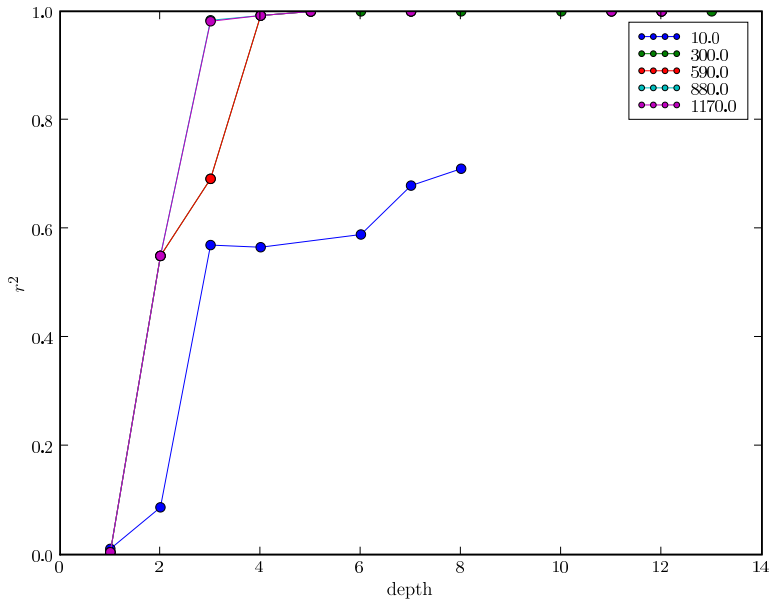

Figure 7.4: Pareto front for the r^2 versus the depth of the expression tree. Note that good solutions are maximized under the r^2 axis and minimized under the depth axis.

depth four nodes is,

$$\tau = (0.0183472 + 0.478082 \cdot v) \cdot (\sin(\theta) - 0.714295 \cdot u). \tag{7.5}$$

Above, we note that the $u \cdot v$ dependence of the generated data can be seen, however the expression has no ω dependence, indicating that either more runs are necessary or, more likely, that a local optima was obtained. The more complex solutions show a similar lack of dependence on ω. We note that this run is typical of the ones observed - namely this fitness function often falls into local optima where incorrect dependence on variables is predicted.

We repeat the above procedure to analyze the results of using the Pearson's r^2 coefficient as the cost function for the symbolic regression. We show the Pareto optimal front as a function of iteration is shown in Fig. 7.2. Generation 10, 300, 500, 880 and 1170 are shown above. For this cost function, learning

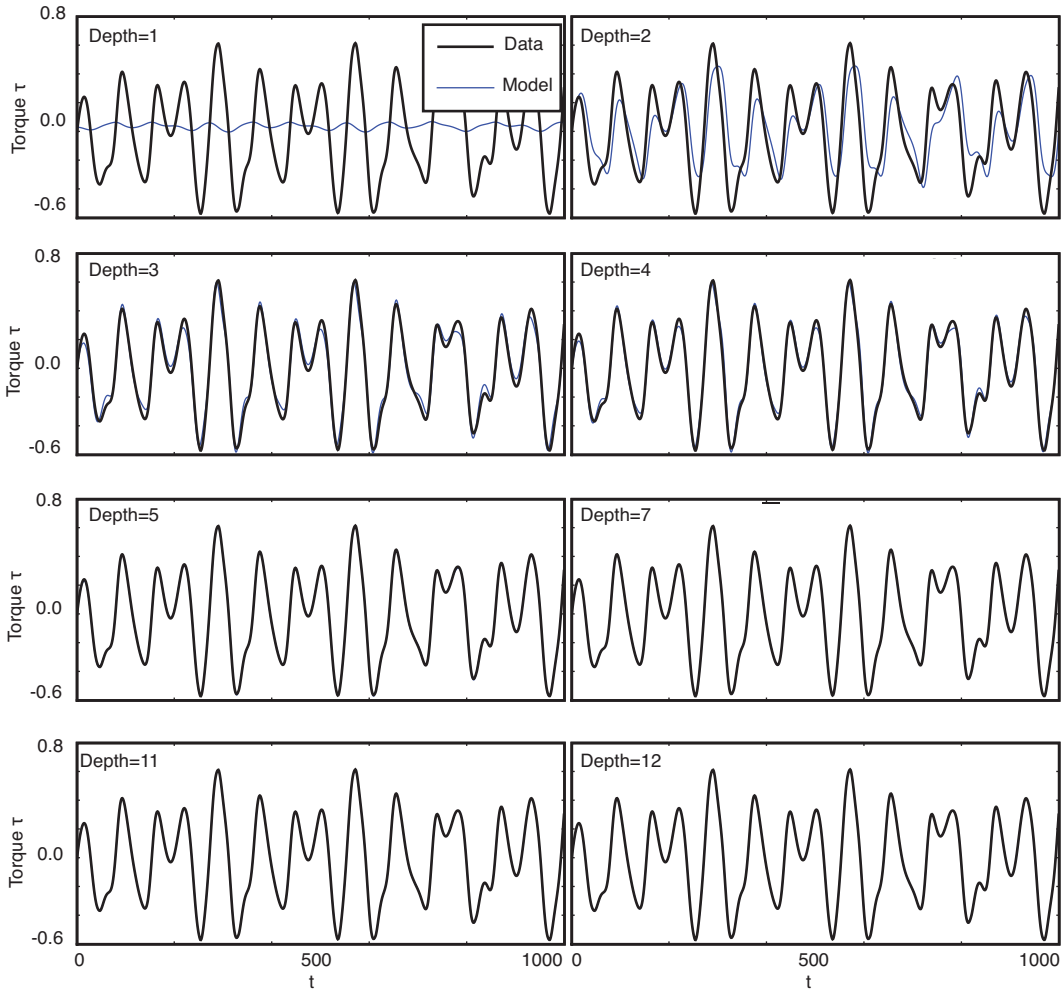

Figure 7.5: Temporal traces of torque as measured using simulated run of falling paper model and as predicted by various results of symbolic regression. Used correlation coefficient as fitness.

takes place over a significantly longer time period, and the expression trees only converge past iteration 600. The diminishing returns that could be seen for the sse cost function of the accuracy of expression with added depth can be seen here as well. In fact, we find that past a depth of 3 very little improvement in the accuracy of function can be seen.

In Fig. 7.3 we show the time trace of torque for the motion. We see that by depth 3 the predicted line follows the trend fairly well and there is little

improvement past this point. The resulting equation,

$$\tau = -0.501349 \cdot (\cos(\cos(0.803327 - \omega)) + \omega + 0.803327 - u \cdot v \cdot -1.98668) + 0.78714, \quad (7.6)$$

shows the correct $u \cdot v$ dependence in the original input model, and includes dependence on ω as well. We note that the ω dependence in this run is not the completely correct one, however in the range of angular velocities encountered in this trajectory $-0.501349 \cdot (\cos(\cos(0.803327 - \omega)) + \omega$ proves to be an extremely close approximation to $-(0.2 + 0.2\,|\omega|)\omega$. On some runs the exact torque was found using the genetic algorithm, however this is a typical run, where correct variable dependence was found to an arbitrarily high approximation at a reasonably tree size.

We find that using a cost function of the Pearson's r^2 coefficient is a significant improvement over sum of square errors. We therefore choose this cost function for the analysis of the real data.

7.3.2 Real Data

To generate an improved quasi-steady model of the torque about a falling wings centroid, we generate a trajectory of a falling plate by direct simulations of the Navier-Stokes equations. We show a typical run that we use in our analysis in Fig. 7.6. The numerical method used to generate this trajectory is shown in §6.2.2. We repeat the analysis found in §7.3.1 on this dataset.

We show the Pareto optimal front as a function of iteration for symbolic regression of the full dataset in Fig. 7.7. We show generations 10, 90, 170, 250 and 330. We find that past generate 200 the Pareto front converges and little learning takes place. As opposed to the falling paper data, the full dataset does not

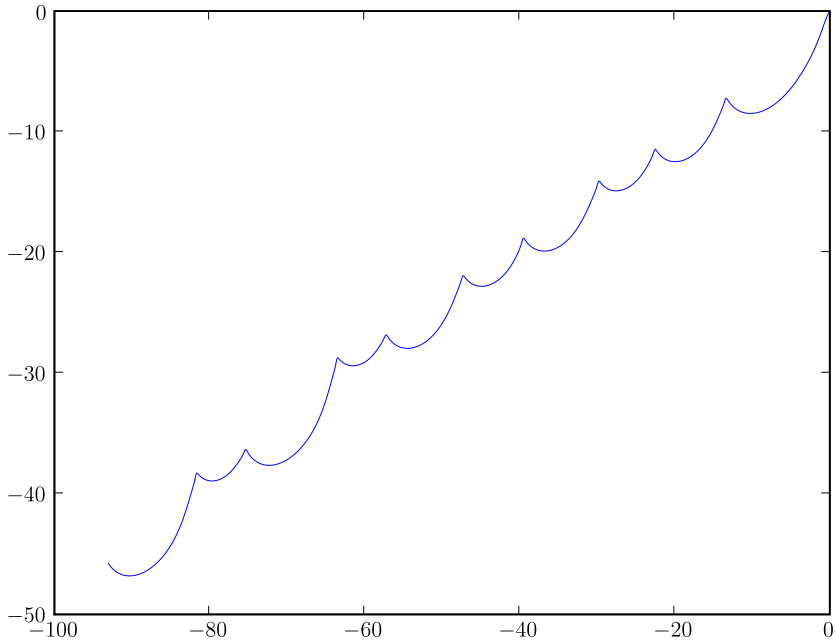

Figure 7.6: Motion trace of data obtained from direct simulation of Navier-Stokes equation.

have a clear diminishing return point when the accuracy of the symbolic trees is considered as a function of tree depth. There is a much smoother improvement curve that improves dramatically between depths 1–4 and then falls off somewhat past this depth, but still continues to rise.

In Fig. 7.3, we show the time trace of torque for the motion. We once again find that by depth 4 the predicted curve follows the full dataset well, although unlike the falling paper data there are deviations from this curve. The torque model that results from this regression is,

$$\tau = -0.00184853 \cdot \frac{\sin(3.95855 - v)}{0.121015 - u + \sin(u)} - 0.00664301. \tag{7.7}$$

We find that this model improves on the accuracy of the falling paper model for the regressed trajectory. Thus, in the absolute sense it represents an improve-

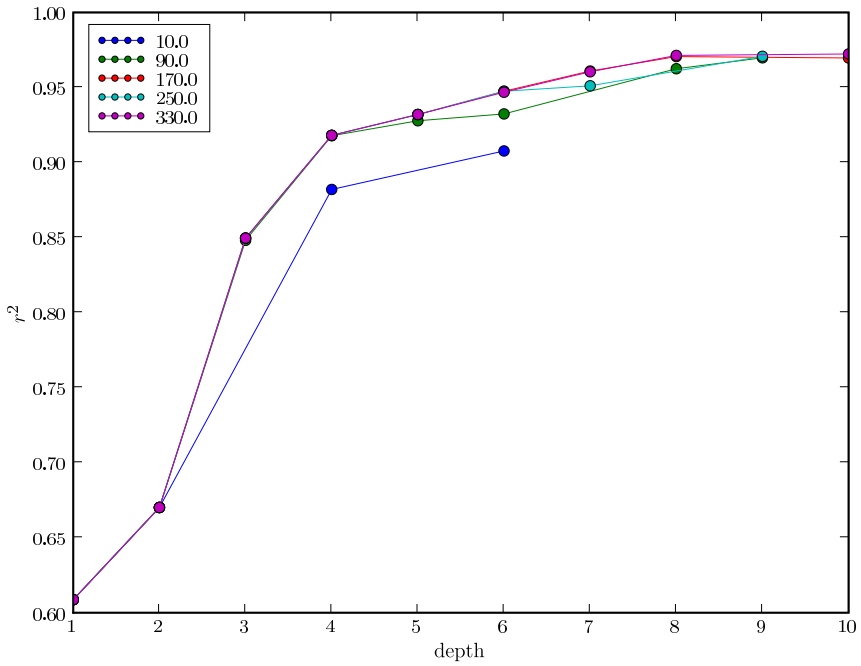

Figure 7.7: Pareto front for the r^2 versus depth of the expression tree. Note that good solutions are maximized under the r^2 axis and minimized under the depth axis.

ment in accuracy. However, the formula gives little insight into the underlying processes. This is, in part, because the dimensions of the equations are incorrect. Therefore, formulas such as Eq. 7.7 either must be rigorously analyzed by hand the genetic algorithm must be modified to take units into account. This indicates that a quasi-steady torque model may exist, and can be approximated by some of the models present.

7.4 Summary and Future Work

Here, we introduce a genetic programming method for discovering the equations of motions that drive a physical system. We find that by incorporating

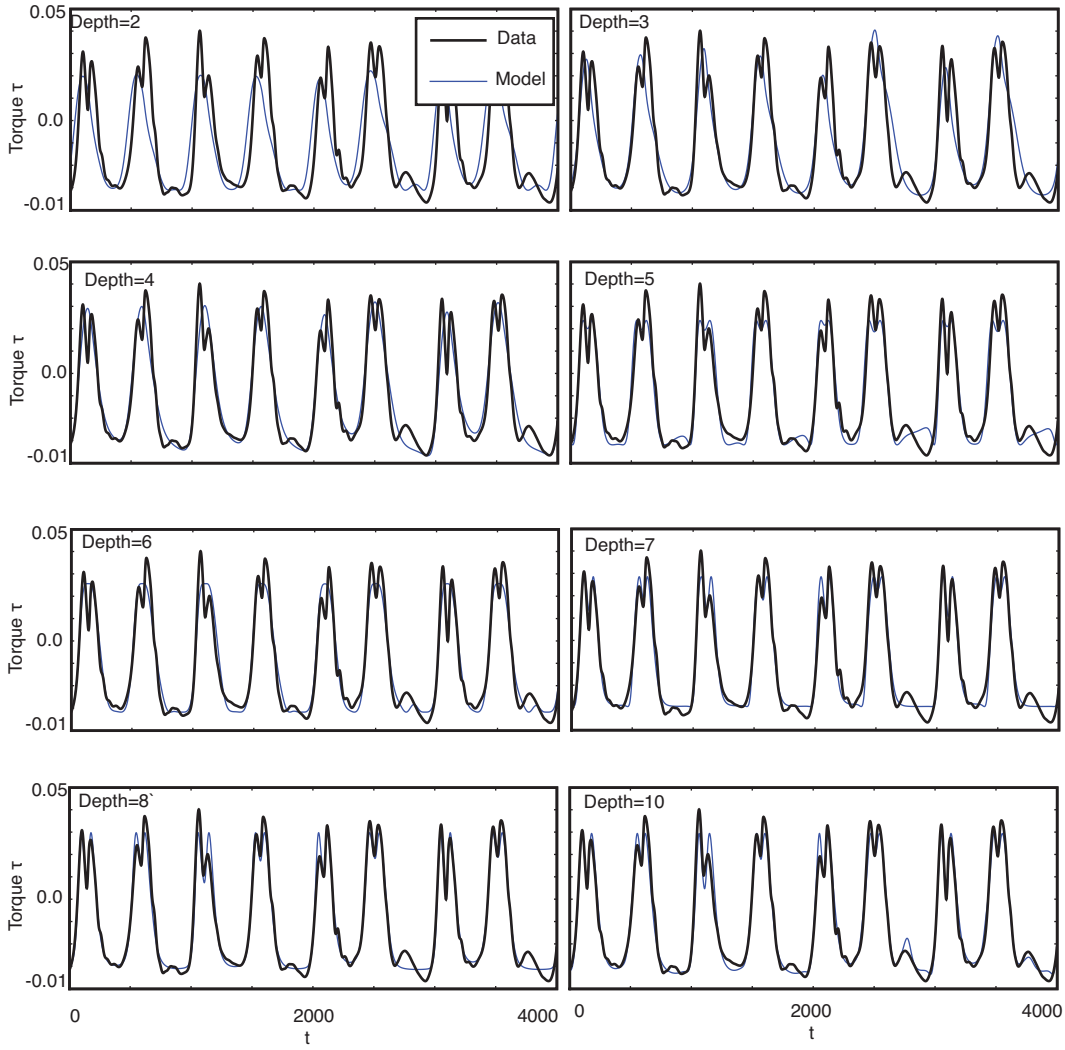

Figure 7.8: We compare models of various complexity for τ that were found using the symbolic regression method to the target value calculated from simulating the Navier-stokes equations. For the above results, we use the correlation coefficient as the cost function for the genetic algorithm.

multi-objective Pareto optimization to reduce bloat, active and passive diversity maintenance, and the correlation-coefficient as the fitness function we are able to recover the torque model that is used to generate a simulated trajectory of a plate falling under the influence of gravity. We also apply this method to recovering an approximate quasi-steady torque model from numerical solutions of the Navier-Stokes equations. We find that this method is able to recover

models that improve upon the torque model in the Falling paper in the sense that they have a lower sum of square error and higher correlation coefficient. They, however, do not provide any insight into the physics underlying the system. Therefore, the formulas that this software currently outputs are of limited benefit. They must either be rigorously analyzed by hand to ensure that they are physically viable or improvements must be made to the algorithm to account for its shortcomings. Nonetheless, the fact that this algorithm produces high quality symbolic approximations of the quasi-steady torque, lends hope that with future improvements to this technology an accurate physically based quasi-steady model may be found.

To improve the above described GA method, we plan to include the ability to generate expressions that have consistent units [134]. We believe that by doing so the models that the GA finds will be much improved. Additionally, the use of numerical solutions of Eq. 6.1 to generate the target torques may be transcended by the use of direct experiments measuring the trajectories of falling plates.

BIBLIOGRAPHY

[1] E-. J. Marey. *Movement*. William Heinemann, 1895.

[2] J. B. Pettigrew. *Animal Locomotion or Walking, Swimming and Flying*. Henry S. King, 1873.

[3] Z. J. Wang. Aerodynamic efficiency in flapping filght: analysis of a two-stroke model. *J. Exp. Biol.*, 211:234–238, 2008.

[4] R. B. Srygley and A. L. R. Thomas. Unconventional lift-generating mechanisms in free-flying butterflies. *Nature*, 420:660–664, 2002.

[5] S. Fry, R. Sayaman, and M. H. Dickinson. The aerodynamics of free-flight maneuvers in *Drosophila*. *Science*, 300:495–498, 2003.

[6] Z. J. Wang and D. B. Russell. Effect of forewing and hindwing interactions on aerodynamic forces and power in hovering dragonfly flight. *PRL*, 99(148101):148101–1 – 148101–4, 2007.

[7] M. Sun and S. Lan. A computational study of the aerodynamic forces and power requirements of dragonfly (*Aeschna juncea*). *J. Exp. Biol.*, 2004.

[8] W. B. Dickson, A. D. Straw, and M. H. Dickinson. Integrative model of *Drosophila* flight. *AIAA*, 46(9):2150–2164, 2008.

[9] Z. J. Wang. Vortex shedding and frequency selection in flapping flight. *J. Fluid Mech.*, 2000.

[10] D. I. Pullin and Z. J. Wang. Unsteady forces on an accelerating plate and application to hovering insect flight. *Journal of Fluid Mechanics*, 509:1–21, 2004.

[11] Z. J. Wang. The role of drag in insect hovering. *J. Exp. Biol.*, 207:4147–4155, 2004.

[12] T. Weis-Fogh. Quick estimates of flight fitness in hovering animals, including novel mechanisms for lift production. *J. Exp. Biol.*, 59:169–230, 1973.

[13] G. K. Taylor. Mechanics and aerodynamics of insect flight control. *Biol. Rev.*, 76:449–471, 2001.

[14] C. P. Ellington. The aerodynamics of hovering insect flight. I. the quasi-steady analysis. *Phil. Trans. R. Soc. B*, 305(1122):1–15, 1984.

[15] S. P. Sane and M. H. Dickinson. The aerodynamic effects of wing rotation and revised quasi-steady model of flapping flight. *J. Exp. Biol.*, 205:1087–1096, 2002.

[16] A. Wisser. Mechanisms of wing rotating regulation in *Calliphora erythrocephala* (Insecta, Diptera). *Zoomorphology*, 106:261–268, 1987.

[17] J. A. Miyan and A. W. Ewing. How Diptera move their wings: A re-examination of the wing base articulation and muscle systems concerned with flight. *Philos. T. R. Soc. B*, 311:271–302, 1985.

[18] J. A. Miyan and A. W. Ewing. Further observations on Dipteran flight: Details of the mechanism. *J. Exp. Biol.*, 136:229–241, 1988.

[19] R. J. Wootton. Functional-morphology of insect wings. *Annu. Rev. Entomol.*, 37:113–140, 1992.

[20] M. H. Dickinson and M. S. Tu. The function of Dipteran flight muscle. *Comp. Biochem. Physiol.*, 116A:223 – 238, 1997.

[21] R. Dudley. *The Biomechanics of Insect Flight: Form, Function, Evolution*. Princeton University, 2000.

[22] M. H. Dickinson. The initiation and control of rapid flight maneuvers in fruit flies. *Integr. Comp. Biol.*, 45:274–281, 2005.

[23] J. O. Vigoreaux, editor. *Nature's Versatile Engine:: Insect Flight Muscle Inside and Out*. Springer, first edition, 2005.

[24] A. L. R. Thomas, G. K. Taylor., R. B. Srygley, and R. L. Nudds. Dragonfly flight: free-flight and tethered flow visualizations reveal a diverse array of unsteady lift-generating mechanisms, controlled primarily *via* angle of attack. *J. Exp. Biol.*, 207:4299–4323, 2004.

[25] L. Ristroph, G. J. Berman, A. J. Bergou, Z. J. Wang, and I. Cohen. An automated hull reconstruction motion tracking (HRMT) to study sideways maneuvers of free-flying insects. *J. Exp. Biol.*, 212, 2009.

[26] D. B. Russell. *Numerical and Experimental Investigations into the Aerodynamics of Dragonfly Flight*. PhD thesis, Cornell University, 2004.

[27] M. H. Dickinson, F.-O. Lehmann, and K. G. Götz. The active control of wing rotation by *Drosophila*. *J. Exp. Biol.*, 182:173–189, 1993.

[28] R. Norberg. The pterostigma of insect wings an inertial regulator of wing pitch. *J. Comp. Physiol.*, 81:9–22, 1972.

[29] A. R. Ennos. The inertial cause of wing rotation in Diptera. *J. Exp. Biol.*, 140:161–169, 1988.

[30] S. N. Fry, R. Sayaman, and M. H. Dickinson. The aerodynamics of hovering flight in *Drosophila*. *J. Exp. Biol.*, 208:2303–2318, 2005.

[31] A. P. Willmott and C. P. Ellington. The mechanics of flight in the hawkmoth *Manduca Sexta* I. Kinematics of hovering and forward flight. *J. Exp. Biol.*, 200:2705–2722, 1997.

[32] Z. J. Wang. Two dimensional mechanism for insect hovering. *Phys. Rev. Lett.*, 85:2216–2219, 2000.

[33] D. Song, H. Wang, L. Zeng, and C. Yin. Measuring the camber deformation of a dragonfly wing using projected comb fringe. *Rev. Sci. Instrum.*, 72(5):2450–2454, 2000.

[34] S. A. Combes and T. L. Daniel. Flexural stiffness in insect wings II. Spatial distribution and dynamic wing bending. *J. Exp. Biol.*, 206:2989–2997, 2003.

[35] A. P. Willmott and C. P. Ellington. The mechanics of flight in the hawkmoth *Manduca Sexta* II. Aerodynamic consequences of kinematic and morphological variation. *J. Exp. Biol.*, 200:2273–2745, 1997.

[36] A. P. Andersen, U. Pesavento, and Z. J. Wang. Unsteady aerodynamics of fluttering and tumbling plates. *J. Fluid Mech.*, 541:65–90, 2005.

[37] G. J. Berman. *Optimiation, control, and flies: quantitative studies of insect flight*. PhD thesis, Cornell University, 2009.

[38] A. D. Briscoe and L. Chittka. The evolution of color vision in insects. *Ann. Rev. Entomol.*, pages 471–511, 2001.

[39] E. I. Fontaine, M. H. Dickinson, and J. W. Burdick. Wing and body motion during flight initiation in *Drosophila* revealed by automated visual tracking. *J. Exp. Biol.*, 212:1307–1323, 2009.

[40] S. M. Walker, A. L. R. Thomas, and G. K. Taylor. Photogrammetric reconstruction of high-resolution surface topographies and deformable wing kinematics of tethered locusts and free-flying hoverflies. *Journ. Roy. Soc. Int.*, 2008.

[41] D. Hoiem. *Seeing the World Behind the Image: Spatial Layout for 3D Scene Understanding*. PhD thesis, Carnegie Mellon University, 2007.

[42] G. J. Berman and Z. J. Wang. Energy-minimizing kinematics in hovering insect flight. *J. Fluid Mech.*, 582:153–168, 2007.

[43] W. Schroeder, K. Martin, and B. Lorensen. *The Visualization Toolkit, 3rd Edition.* Kitware Inc., 2003.

[44] J. B. MacQueen. Some methods for the classification and analysis of multivariate observations. In *Proceedings of 5th Berkeley Symposium on Mathematical Statistics and Probability*, pages 281–297. University of California Press, 1967.

[45] H. Goldstein, C. Poole, and J. Safko. *Classical Mechanics*. Pearson Educations, 2002.

[46] A. A. Shabana. *Dynamics of Multibody Systems*. Cambridge, third edition, 2005.

[47] K. G. Götz and U. Wandel. Optomotor control of the force of flight in *Drosophila* and *Musca* II. Covariance of lift and thrust in still air. *Biol. Cybern.*, 51:135–139, 1984.

[48] C. T. David. The relationship between body angle and flight speed in free-flying *Drosophila*. *Physiol. Entomol.*, 3:191 – 195, 1978.

[49] Persistence of Vision Pty. Ltd. Persistence of vision raytracer (version 3.6). `http://www.povray.org/`, 2004.

[50] W. Härdle. *Applied nonparametric regression*. Cambridge University, 1992.

[51] J. M. Wakeling and C. P. Ellington. Dragonfly flight II. Velocities, accelerations and kinematics of flapping flight. *J. Exp. Biol.*, 200:557–582, 1997.

[52] J. M. Wakeling and C. P. Ellington. Dragonfly flight III. Lift and power requirements. *J. Exp. Biol.*, 200:583–600, 1997.

[53] A. J. Bergou, S. Xu, and Z. J. Wang. Passive wing pitch reversal in insect flight. *J. Fluid Mech.*, 591:321–337, 2007.

[54] A. Azuma, S. Azuma, I. Watanabe, and T. Furuta. Flight mechanics of a dragonfly. *J. Exp. Biol.*, 116:79–107, 1985.

[55] H. Liu. Integrated modeling of insect flight: From morphology, kinematics to aerodynamics. *J. Comput. Phys.*, 228(2):439–459, 2009.

[56] Y. Liu and M. Sun. Wing kinematics measurement and aerodynamics of hovering droneflies. *J. Exp. Biol.*, 211(13):2014–2025, 2008.

[57] J. P. Boyd. *Chebyshev and Fourier Spectral Methods*. Dover Publications, Inc., second edition, 2001.

[58] R. Anderssen and P. Bloomfield. Numerical differentiation procedures for non-exact data. *Numer. Math.*, 22:157–182, 1974.

[59] H.-G. Müller, U. Stadtmüller, and T. Schmitt. Bandwidth choice and confidence intervals for derivatives of noisy data. *Biometrika*, 74(4):743–749, 1987.

[60] R. Anderssen, F. de Hoog, and M. Hegland. A stable finite difference ansatz for higher order differentiation of non-exact data. *Bull. Austral. Math. Soc.*, 58:223–232, 1996.

[61] B. Carlsson, M. Sternad, and A. Ahlen. Digital differentiation of noisy data measured through a dynamicsystem. *IEEE Trans. Sig. Proc.*, 40(1):218–222, 1992.

[62] R. Anderssen and M. Hegland. For numerical differentiation, dimensionality can be a blessing! *Math. Comput.*, 68(227):1121–1141, 1999.

[63] R. Chartrand. Numerical differentiation of noisy data. `http://math.lanl.gov/Research/Publications/Docs/chartrand-2007-numerical.pdf`, 2007.

[64] S. Revzen and J. M. Guckenheimer. Estimating the phase of synchronized oscillators. *Phys. Rev. E*, 78:051907–1–12, 2008.

[65] G. G. Magaril-Il'yaev and K. Y. Osipenko. Optimal recovery of periodic functions and their derivatives from fourier coefficients prescribed with error. *Sb. Math.*, 193:387–407, 2002.

[66] M. Zhang, K. Montooth, M. Wells, A. Clark, and D. Zhang. Mapping multiple quantitative trait loci by bayesian classification. *Genetics*, 169:2305–2318, 2005.

[67] P. Bobrov and E. Ostrovskii. Confidence intervals in adaptive estimation. *J. Math. Sci.*, 99(2):1031–1043, 2000.

[68] L. N. Thibos. *Fourier Analysis for Beginners*. Visual Sciences Group, third edition, 2003.

[69] M. B. Tischler. *Advances in aircraft flight control*. Taylor & Francis, 1996.

[70] S. P. Sane and M. H. Dickinson. The control of flight force by a flapping wing: lift and drag production. *J. Exp. Biol.*, 204:2607–2626, 2001.

[71] D. Ishihara, T. Horie, and M. Denda. A two-dimensional computational study on the fluid-structure interaction cause of wing pitch changes in Dipteran flapping flight. *J. Exp. Biol.*, 212:1–10, 2009.

[72] L. B. Tuckerman. Inertia factors of ellipsoids for use in airship design. *Report National Advisory Committee for Aeronautics*, 210:62–67, 1926.

[73] A. R. Ennos. The importance of torsion in the design of insect wings. *J. Exp. Biol.*, 140:137–160, 1988.

[74] Y. C. Fung. *Biomechanics: Mechanical Properties of Living Tissues*. Springer, second edition, 1993.

[75] K. Levenberg. A method for the solution of certain non-linear problems in least squares. *Q. Appl. Math.*, 2:164–168, 1944.

[76] T. Hesselberg and F.-O. Lehmann. Turning behaviour depends on frictional damping in the fruit fly *Drosophila*. *J. Exp. Biol.*, 210(24):4319–4334, 2007.

[77] T. L. Hedrick, B. Cheng, and X. Deng. Wingbeat time and the scaling of passive rotational damping in flapping flight. *Science*, 324:252–255, 2009.

[78] M. Frye and M. H. Dickinson. Closing the loop between neurobiology and flight behavior in *Drosophila*. *Curr. Opin. Neurobiol.*, 14:729–736, 2004.

[79] A. M. Reynolds and M. A. Frye. Free-flight odor tracking in *Drosophila* is consistent with an optimal intermittent scale-free search. *PLoS ONE*, 2(4), 2007.

[80] A. R. Ennos. The kinematics and aerodynamics of the free flight of some Diptera. *J. Exp. Biol.*, 142:49–85, 1989.

[81] A. M. Mountcastle and T. L. Daniel. Aerodynamic and functional consequences of wing compliance. *Exp. Fluids*, 2009.

[82] S. A. Combes and T. L. Daniel. Into thin air: contributions of aerodynamic and inertial-elastic forces to wing bending in the hawkmoth *Manduca sexta*. *J. Exp. Biol.*, 206:2999–3006, 2003.

[83] S. Collins, A. Ruina, R. Tedrake, and M. Wisse. Efficient bipedal robots based on passive-dynamic walkers. *Science*, 307(5712):1082–1085, 2005.

[84] J. C. Liao, D. N. Beal, G. V. Lauder, and M. S. Triantafyllou. Fish exploiting vorticies decrease muscle activity. *Science*, 302:1566–1569, 2003.

[85] R. J. Wood. The rst takeoff of a biologically inspired at-scale robotic insect. *IEEE Trans. Robotics*, 24:341–347, 2008.

[86] G. K. Taylor and A. L. R. Thomas. Animal flight dynamics II. Longitudinal stability in flapping flight. *J. Theor. Biol.*, 214:351–370, 2002.

[87] U. Pesavento and Z. J. Wang. Falling paper: Navier-stokes solutions, model of fluid forces, and center of mass elevation. *Phys. Rev. Lett.*, 93(14):144501, 2004.

[88] S. P. Sane. Induced airflow in flying insects I. A theoretical model of the induced flow. *J. Exp. Biol.*, 209:32–42, 2006.

[89] S. P. Sane and N. P. Jacobson. Induced airflow in flying insects II. Measurement of induced flow. *J. Exp. Biol.*, 209:43–56, 2006.

[90] D. E. Alexander. *Nature's Flyers*. The Johns Hopkins University Press, 2002.

[91] C. P. Ellington, C. Berg, A. P. Willmott, and A. L. R. Thomas. Leading-edge vortices in insect flight. *Nature*, 384:626–630, 1996.

[92] M. Kliss, C. Somps, and M. Luttges. Stable vortex structures: A flat plate model of dragonfly hovering. *J. Theor. Biol.*, 89:209–228, 1989.

[93] Z. J. Wang, J. M. Birch, and M. H. Dickinson. Unsteady forces and flows in low reynolds number hovering flight: two-dimensional computations vs. robotic wing experiments. *J. Exp. Biol.*, 207:449–460, 2004.

[94] F. Minotti. Unsteady two-dimensional theory of a flapping wing. *Phys. Rev. E*, 2002.

[95] S. Xu and Z. J. Wang. An immersed interface method for simulating the interaction of fluid with moving boundaries. *J. Comput. Phys.*, 216:454–493, 2006.

[96] L. Miller and C. Peskin. When vortices stick: an aerodynamic transition in tiny insect flight. *J. Exp. Biol.*, 2004.

[97] J. Wu and M. Sun. Unsteady aerodynamic forces of a flapping wing. *J. Exp. Biol.*, 207:1137–1150, 2004.

[98] S. Xu and Z. J. Wang. Systematic derivation of jump conditions for the immersed interface method in three-dimensional flow simulation. *SIAM J. Sci. Comp.*, 27(6):1948–1980, 2006.

[99] D. Le, B. Khoo, and J. Peraire. An immersed interface method for viscous incompressible flows involving rigid and flexible boundaries. *J. Comput. Phys.*, 220(1):109–138, 2006.

[100] J. R. Usherwood and C. P. Ellington. The aerodynamics of revolving wings I. Model hawkmoth wings. *J. Exp. Biol.*, 205:1547–1564, 2002.

[101] J. R. Usherwood and C. P. Ellington. The aerodynamics of revolving wings II. Propeller force coefficients from mayfly to quail. *J. Exp. Biol.*, 205:1565–1576, 2002.

[102] Y. Kim and C. Peskin. Penalty immersed boundary method for an elastic boundary with mass. *Phys. Fluids*, 19(5):053103, 2007.

[103] A. P. Andersen, U. Pesavento, and Z. J. Wang. Unsteady aerodynamics of fluttering and tumbling plates. *Journal of Fluid Mechanics*, 2005.

[104] S. D. Alben and M. Shelley. Coherent locomotion as an attracting state for a free flapping body. *PNAS*, 102(32):11163–11166, 2005.

[105] A. P. Andersen, U. Pesavento, and Z. J. Wang. Analysis of transitions between fluttering, tumbling and steady descent of falling cards. *J. Fluid Mech.*, 2005.

[106] N. Vandenberghe, J. Zhang, and S. Childress. Symmetry breaking leads to forward flapping flight. *J. Fluid Mech.*, 506:147–155, 2004.

[107] W. E and J.-G. Liu. Essentially compact schemes for unsteady viscous incompressible flows. *J. Comput. Phys.*, 126:122–138, 1996.

[108] M. Jensen. Biology and physics of locust flight. iii. the aerodynamics of locust flight. *Philos. Trans. Roy. Soc. B*, 239(667):511–552, 1956.

[109] M. Jensen and T. Weis-Fogh. Biology and physics of locust flight. v. strength and elasticity of locust cuticle. *Philos. Trans. Roy. Soc. B*, 245(721):137–169, 1961.

[110] T. Weis-Fogh and M. Jensen. Biology and physics of locust flight. i. basic principles in insect flight. a critical review. *Philos. Trans. Roy. Soc. B*, 239(667):415–458, 1956.

[111] J. Walker. Rotational lift: Something different or more of the same? *J. Exp. Biol.*, 205:3783–3792, 2002.

[112] R. Zbikowski. On aerodynamic modelling of an insect-like flapping wing in hover for micro air vehicles. *Phil. Trans. R. Soc. Lond. A*, 360:273–290, 2002.

[113] S. Fry, R. Sayaman, and M. H. Dickinson. The aerodynamics of hovering flight in *Drosophila*. *J. Exp. Biol.*, 208:2303–2318, 2005.

[114] G. Spedding, A. Hedenstrom, J. McArthur, and M. Rosen. The implica-

tions of low-speed fixed-wing aerofoil measurements on the analysis and performance of flapping bird wings. *J. Exp. Biol.*, 211:215–223, 2008.

[115] A. P. Andersen, U. Pesavento, and Z. J. Wang. Analysis of transitions between fluttering, tumbling and steady descent of falling cards. *J. Fluid Mech.*, 541:91–104, 2005.

[116] L. I. Sedov. *Two-Dimensional Problems in Hydrodynamics and Aerodynamics*. Interscience, 1965.

[117] J. N. Newman. *Marine Hydrodynamics*. MIT Press, 1977.

[118] C. E. Brennen. A review of added mass and fluid inertial forces. Technical Report CR82.010, Naval Civil Engineering Laboratory, Port Hueneme, CA, USA, 1982.

[119] M. H. Dickinson, F.-O. Lehmann, and S. P. Sane. Wing rotation and the aerodynamic basis of insect flight. *Science*, 284:1954–1960, 1999.

[120] R. H. Dieck. *Measurement Uncertainty*. ISA, fourth edition, 2006.

[121] H. P. Langtangen and A. Tveito. *Advanced Topics in Computational Partial Differential Equations: Numerical Methods and Diffpack Programming*. Springer, 2004.

[122] M. Mitchell. *An Introduction to Genetic Algorithms*. MIT Press, 1998.

[123] C. L. M. H. Navier. Memoire sur les lois du mouvement des fluides. *Mem. Acad. Sci. Inst. France*, 6:389–440, 1822.

[124] S. Xu and Z. J. Wang. An immersed interface method for simulating the interaction of a fluid with moving boundaries. *J. Comput. Phys.*, 216:454–493, 2006.

[125] J. R. Koza. A genetic approach to econometric modeling. In *Sixth World Congress of the Econometric Society*, 1990.

[126] S. Luke and L. Panait. A comparison of bloat control methods for genetic programming. *Evolutionary Computation*, 14(3):309–344, 2006.

[127] S. Luke and L. Spector. A comparison of crossover and mutation in genetic programming. In *Genetic Programming 1997: Proceedings of the Second Annual Conference*, pages 240–248. MIT Press, 1997.

[128] S. Bleuler, M. Brack, L. Thiele, and E. Zitzler. Multiobjective genetic programming: Reducing bloat using SPEA2. In *Proceedings of the 2001 Congress on Evolutionary Computation CEC2001*, pages 536–543, COEX, World Trade Center, 159 Samseong-dong, Gangnam-gu, Seoul, Korea, 2001. IEEE Press.

[129] Y. Bernstein, X. Li, V. Ciesielski, and A. Song. Multiobjective parsimony enforcement for superior generalisation performance. In *Proceedings of the 2004 IEEE Congress on Evolutionary Computation*, pages 83–89. IEEE Press, 2004.

[130] K. Deb, S. Agrawal, A. Pratap, and T. Meyarivan. A fast elitist non-dominated sorting genetic algorithm for multi-objective optimisation: NSGA-II. In M. Schoenauer, K. Deb, G. Rudolph, X. Yao, E. Lutton, J. J. Merelo, and H.-P. Schwefel, editors, *Proceedings of the 6th International Conference on Parallel Problem Solving from Nature - PPSN VI*, volume 1917, pages 849–858, Paris, France, 2000. Springer-Verlag.

[131] E. D. de Jong and J. B. Pollack. Multi-objective methods for tree size control. *Genetic Programming and Evolvable Machines*, 4(3):211–233, 2003.

[132] S. M. Gustafson. *An Analysis of Diversity in Genetic Programming*. PhD thesis, University of Nottingham, 2004.

[133] W. D. Hillis. Co-evolving parasites improve simulated evolution as an optimization procedure. In *Artificial Life II*, volume X, pages 313–324. Addison-Wesley, 1992.

[134] M. Keijzer. *Scientific Discovery using Genetic Programming*. PhD thesis, Danish Technical University, 2002.